UNIVERSITY OF CALIFORNIA
SANTA CRUZ

GALACTIC EVOLUTION THROUGH THE FAR-ULTRAVIOLET LENS

A dissertation submitted in partial satisfaction of the
requirements for the degree of

Doctor of Philosophy

in

ASTRONOMY AND ASTROPHYSICS

by

Sara R. Crandall

June 2021

The Dissertation of Sara R. Crandall is approved:

Graeme H. Smith, Chair

Constance M Rockosi

Ruth Murray-Clay

Quentin Williams
Interim Vice Provost and Dean of Graduate Studies

Table of Contents

List of Figures

List of Tables

Abstract

Galactic Evolution Through the Far-Ultraviolet Lens

by

Sara R. Crandall

This thesis adds to the toolbox of techniques in estimating late-F, G and K type dwarf star fundamental parameters; specifically age. Stellar age cannot be directly measured, yet age determinations are fundamental to understanding the evolution of our universe's constituents. Stellar modeling techniques such as isochrone fitting are used to estimate ages and interpret the evolution of the Milky Way galaxy. However, the models have varying accuracy. Through model-independent estimates of age and metallicity determined through purely empirical methods, one gains an understanding of the stellar evolution and the greater context of the Milky Way's formation and evolution.

This thesis first calibrates a relationship between stellar age and far-ultraviolet observations. I utilized far-ultraviolet photometry acquired by the Galaxy Evolution Explorer (*GALEX*) space telescope as an indicator of chromospheric activity to infer ages of late-F, G, and K type dwarf stars. I derived a purely empirical correlation between FUV magnitudes and stellar age in conjunction with $(B-V)$ color. My attention is restricted to sun-like stars with color range $0.55 \leq (B-V) \leq 0.71$ and absolute magnitude range $4.3 \leq M_{\rm V} \leq 5.3$. The correlation is defined in terms of a FUV-excess parameter $Q(FUV-B, B-V)$. I related stellar age, τ, to Q through the relation $\log_e(\tau) = \log_e(a) + bQ$, where a and b are fit parameters and functions of $(B-V)$. This correlation is functional up to 6 Gyr for FGK dwarfs. With such a

correlation, one only need Johnson $(B-V)$ and FUV measurements to estimate stellar age for Population I dwarf stars of solar-like temperature and metallicity.

The nature of the activity-age relationship is more elusive for giants. The difficulties in analyzing the age-activity relationship of giants stem from the challenges in determining low activity levels from observed activity indicators. In this thesis I have examined correlations between four chromospheric and coronal activity indicators. I found an evident correlation between $\log(L_{\rm X}/L_{\rm bol}) > -6.0$ and $\log(F_{\rm MgII}/F_{\rm bol}) < -4.8$, where $L_{\rm X}$ is the X-ray luminosity from ROSAT observations (a coronal activity indicator), and $F_{\rm MgII}$ is the flux from Mg II h and k emission lines (a chromospheric activity indicator). Using *GALEX* far-ultraviolet (FUV) magnitudes I also constrained a relationship between FUV magnitudes as a chromospheric activity indicator and X-ray luminosities. I found a varied range of FUV emission for core-helium burning stars (CHeB) indicating that giants in this phase may be receiving a magnetic field strength "boost." Lastly I endeavored to constrain a relationship between ultraviolet emission and rotational velocities of giants, but did not find a clear relationship. Obscurities in this relationship may be resulting from a lack of $\sin i$ measurements and/or too few stars with $v\sin i > 7$ km/s.

Such a calibration between *GALEX* FUV magnitudes and stellar age has utility in population studies of FGK dwarfs for further understanding of the chemical evolution of the Milky Way. As an illustration of one such application I have investigated a population of solar neighborhood stars for their metallicities and velocity dispersions. I have cross-matched a sample of FGK type dwarf stars from Casagrande et al. (2011)

with the *Gaia* and *GALEX* catalogs. Using calibrated relationships between *FUV* magnitudes and age, I determined a chromospheric activity indicator, Q, and stellar age, τ, for each dwarf. I further investigate the activity-velocity and activity-metallicity relations with [Fe/H] and velocities from Casagrande et al. (2011) and empirically-determined *FUV* ages. I show that perigalactic and eccentricity versus *FUV*-age plots are consistent to an "inside out" formation history model.

Acknowledgments

First and foremost I give thanks to my advisor, Graeme Smith. Graeme was the exact advisor I needed to pursue a Ph.D. Without him I would not have had the will to complete my studies. He is the most empathetic, encouraging, and supportive advisor. Thank you for allowing me the space to pursue my career goals. I won't let you down.

To Connie, Raja, and Brad. You showed faith in me when I had very little in myself. I can't thank you enough for your support and guidance. Without you I wouldn't have found a fruitful thesis.

I would like to thank Sandy Faber, Bob Williams, and the Osterbrock Leadership Program. This program showed me the path to a science policy career which I will continue to pursue after my Ph.D. The OLP has provided me with opportunities that I would not have experienced in a traditional graduate program. What a fantastic time it was to visit Baltimore, Sacramento, D.C., and Space Telescope. Through the OLP I learned how to perform informational interviews, network, and promote my transferable skills.

My gratitude also goes out to my fabulous mentor, Genevieve Graves. You are one of the most inspiring women I know. I am so very grateful for all of the professional and personal advice you've given me during my grad school tenure. I hope that I may be able to pay it forward in the future.

I give thanks to all of my grad school friends who brought joy to my life in Santa Cruz. You all showed such kindness towards me and Tessa. Thank you for all the

memorable pool parties, camping trips, thanksgiving dinners, porch hang outs, pumpkin patch outings, and aquarium visits. I learned a lot from you, including how to properly roast Brussels sprouts.

To my family - I am beyond lucky to have you. Mom, you are my best friend and I can't thank you enough for helping me to grow, see kindness in people, and to be patient. Casey, thank you for editing my work. I am very lucky to have you as a supportive sister. Tessa, I sometimes wonder if I made the wrong decision in attending grad school while trying to focus on motherhood. The patience and support you've shown me is inspiring. You have such joy and love for being a young human, and you help me to feel that my education is worthwhile. To Shaya and Rakia, thank you for allowing me to be a part of your world. You make it exponentially more exciting, joyful, and full of love. I cannot express enough how much grateful I am for my dads, my siblings, and my new Buki family. How lucky am I to have you all!

Shovavi - You have not known me as anyone except a grad student. I'm excited for us to explore the world outside of that space. Thank you for being a Positive Polly and Negative Nancy when appropriately needed. I feel grateful to have spent the last four years with you; including one in which there was a global pandemic. Now, let's move on and "we'll see."

Published Material

The text of this dissertation includes a reprint of the following published material led by Sara Crandall, with the permission of the listed coauthors:

Chapter 2 was published in the literature as Crandall et al. (2020). I was

responsible for data collection, performing analysis, generating figures, and writing the text. I thank Graeme Smith for his support and generous feedback on this written work.

Chapters 3 and 4 are in development for publication. I was responsible for data collection, analyses, generating figures, and writing text. Graeme Smith was responsible for the analysis of the relationship between X-ray luminosity as a coronal activity indicator and Mg II emission as a chromospheric activity in Chapter 3 indicator. I give many thanks to Sufia Birmingham and Vy Vo for their support in data collection and analysis as SIP mentees. Lastly, I thank Graeme Smith, Connie Rockosi, Ruth Murray-Clay for their feedback and guidance on these works.

Scientific Acknowledgments

I gratefully acknowledge the support of the National Science Foundation through award AST-1517791. This research has made use of the NASA Astrophysics Data System. The *GALEX FUV* data presented in this paper were obtained from the Mikulski Archive for Space Telescopes (MAST). STScI is operated by the Association of Universities for Research in Astronomy, Inc., under NASA contract NAS5-26555.

Further, I thank Connie Rockosi, Natalie Batalha, and David Soderblom for their enlightening perspectives and conversations which improved this thesis. Many thanks are given to Ruth Murray-Clay and Connie Rockosi for their guidance and mentorship in exploring Milky Way dynamics. This work would not have been completed without Sufia Birmingham and Vy Vo who enthusiastically explored the age-velocity and age-metallicity relations in their Science Internship Program (SIP) research.

For Pina, Fly High

Chapter 1

Introduction

The convoluted interactions between the Milky Way's constituents complicates our understanding of its evolution and formation history. While there is a long line of studies investigating our galaxy's evolution, major questions still remain unanswered. Is there a relationship between metallicity and star formation? How have stellar velocity dispersions been impacted over the course of the galaxy's evolution? By focusing our attention on the life span of stars as galactic constituents, we become "archaeologists" looking into the Galaxy's past. Then we may interpret the Milky Way's evolution in a broader context.

This thesis adds to the toolbox of techniques used to age-date sun-like stars. Stellar ages are often based on theoretical models, called isochrones, which have varying accuracy. This work demonstrates that one may, instead, utilize direct observations of ultraviolet light to estimate age of main sequence stars similar to our own. The basis of this research lies in observing stellar-atmospheric activity through far-ultraviolet (FUV)

light and correlating observations with age. With a calibrated FUV-activity correlation in hand, we test how stellar systems have evolved within our galaxy. This thesis explores the age-metallicity and age-velocity relations with empirically determined FUV ages to interpret the Milky Way's history.

1.1 Inferring Stellar Ages

Many stellar parameters are directly measured from observed emissions using either spectroscopy or photometry. Stellar age is one of the most significant of these parameters, as it plays a vital part in understanding stellar and galactic evolution. Yet, we cannot directly measure it. Instead, it must be inferred from another measurable parameter referred to as an age indicator. Ages are unique, even among other inferred parameters, because of the wide variance in errors associated with estimating ages. For example, the mass of a main sequence star can be inferred to $\sim$ 10% just from its spectra (Soderblom 2010). However, estimates of stellar ages can easily vary by $\sim$ 60% (Mamajek & Hillenbrand 2008).

In the long developing history in techniques to infer stellar ages, Skumanich (1972) motivated a search for correlating ages to stellar activity indicators. Their work sought to quantify the correlation between stellar age and Ca II H and K emission for stars of similar spectral type. Discovery of further correlations of these types, such as those presented in this thesis, adds to our understanding of the galaxy's evolution on varying scales. As in the Soderblom (2010) extensive review of previous techniques, we here describe our methods, their appropriate arena for application, along with strengths

and weaknesses as we find them.

Yet, not all stellar age-dating techniques are equal nor appropriate in every situation. In an effort to find an ideal technique, Barnes (2007) outlined a list of stellar age indicator characteristics pointing towards an ideal technique. These characteristics include the measurability of a single star's age, without sensitivity to other stellar parameters. Stellar ages would be calibrated against objects with well-measured ages. The indicator would also produce an age as a function of variables, have calculable errors, and is sensitive to age. This thesis work demonstrates an age-dating technique in which chromospheric activity possesses many of the ideal age indicator characteristics: measurability for single stars, sensitivity to age, calibration, and invertibility.

Possibly the most widely-used stellar-age dating technique is isochrone fitting, especially (as will be demonstrated in this thesis) when interpreting the Milky Way's evolution. This technique makes use of color-magnitude diagrams among varied-age stellar populations. A plethora of models and statistical techniques are used to determine isochrone ages. However, significant scatter is often found between ages determined from different isochrone models, especially for older stars. Figure 1.1 demonstrates how ages of stars can differ between independent isochrone fitting models. The figure shows a comparison between the ages of FGK stars as determined by Brewer et al. (2016) and Casagrande et al. (2011). Brewer et al. (2016) utilized interpolated Yonsei-Yale isochrones (Yi et al. 2001) to derive ages of stars observed with Keck Observatory's High Resolution Echelle Spectrometer (HIRES) spectrograph. Casagrande et al. (2011) re-analyzed stellar parameters from the Geneva-Copenhagen Survey and estimated ages

using two isochrone fitting models: BASTI (Pietrinferni et al. 2004, 2006, 2009) and Padova (Bertelli et al. 2008, 2009). Ages can widely differ given varying input parameters and isochrone modeling techniques. As another example, Tayar et al. (2021) shows an associated error in age $\sim 20\%$ given stellar modeling input parameter offsets.

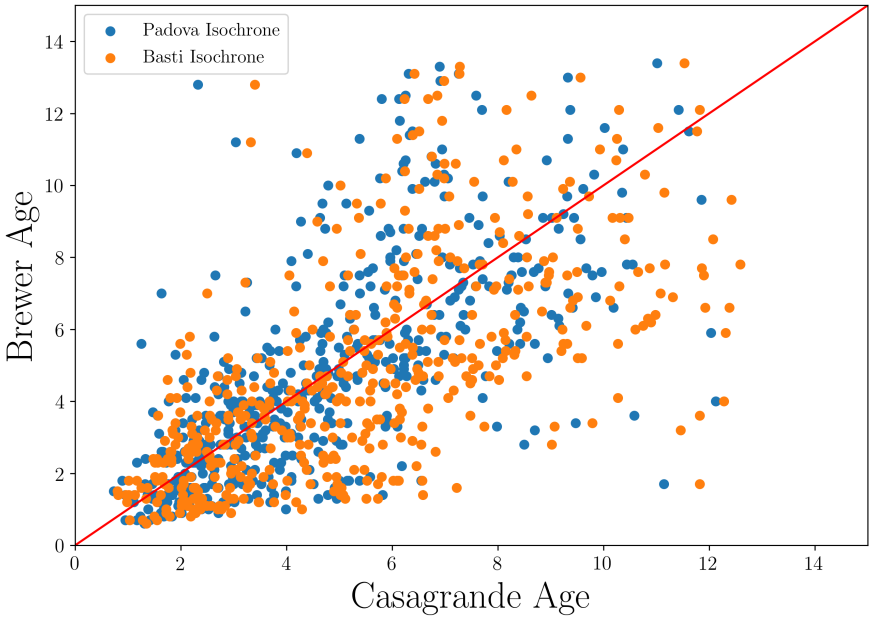

Figure 1.1 An example of how various isochrone fitting models yield differences in ages for single stars. Brewer et al. (2016) ages were determined by interpolating Y^2 isochrones, while Casagrande et al. (2011) utilized two separate isochrones: BASTI (Pietrinferni et al. 2004, 2006, 2009) in orange and Padova (Bertelli et al. 2008, 2009) in blue.

In more recent years the Bayesian method used to determine ages has proven to reduce scatter as compared to traditional isochrone fitting methods (see, e.g. Pont & Eyer 2004; Jørgensen & Lindegren 2004). Utilizing the Bayesian method and *Gaia* DR1 parallax measurements, Lin et al. (2018) have shown that their isochrone-determined ages are similar to those found in the literature with reduced uncertainties for younger stars. However, for stars greater than $\sim$ 2 Gyr their sample has larger scatter as

compared to other well-studied ages. In another chromospheric activity-age relationship work by Mamajek & Hillenbrand (2008), they find a calibration with an age precision of $\pm$ 0.25 dex or $\sim 60\%(1\sigma)$. Such scatter illustrates a need for additional types of age-dating techniques which may be applied to dwarf stars; such as activity ages, lithium ages, or gyrochronology ages. Then one may compare age estimates of stars determined by a variety of methodologies.

This thesis focuses on a purely empirical age-dating technique which has not been extensively calibrated to date, in which far-ultraviolet (FUV) photometry is mapped directly to stellar age. This work demonstrates the use of such an indicator with desired characteristics outlined by Barnes (2007). These characteristics include *measurability for single stars*. That is, FUV emission is measured easily by itself and does not require other quantities to be measured. In addition, FUV emission is demonstrated to be *sensitive to age*; the basis of such correlation shown in the FUV-chromospheric activity relation in Smith & Redenbaugh (2010); Smith et al. (2017). The calibration is also invertable such that one may invert stellar age with FUV magnitudes in a well-defined formula.

1.1.1 The Stellar Age and Atmospheric Activity Relationship

A plethora of creative techniques have been developed to indirectly infer stellar age, such as asteroseismology, lithium depletion, isochrone fitting, and stellar spin-down (Soderblom 2010). Many such works rely on the stellar atmospheric activity-age relationship.

FGK spectral type stars undergo mass loss during the main sequence stage of

evolution via a coronal hot wind along with rotational spin down. This mass loss, in turn, is associated with a decrease in magnetic field strength. Activity levels in the chromosphere, transition region, and corona, are tied to the internal magnetic field strength and thus also decrease with age during the main sequence phase (Skumanich 1972). It has been shown that chromospheric and coronal activity are directly related to magnetic field strength. In addition, there exists a relationship between coronal activity and the ages of main sequence dwarf stars due to stellar spin-down and decreasing magnetic dynamo strength (see e.g. Soderblom et al. 1991; Pace & Pasquini 2004; Mamajek & Hillenbrand 2008; Jackson et al. 2012; Booth et al. 2017). Hence, atmospheric activity is an indicator of stellar age.

Spectral line strengths originating in the chromosphere or transition region are often used as stellar activity indicators (Skumanich 1972; Simon et al. 1985), and hence age. Common examples which show a direct relationship between stellar age and activity of main-sequence stars are the Ca II H and K (see e.g., Barry 1988; Soderblom et al. 1991; Pace & Pasquini 2004; Mamajek & Hillenbrand 2008; Smith & Redenbaugh 2010; Findeisen et al. 2011; Smith et al. 2017; Lorenzo-Oliveira et al. 2018), the Mg II h and k (see e.g., Rutten & Pylyser 1988; Pasquini et al. 1990; Dupree et al. 1999; Pérez Martínez et al. 2011; Smith & Shetrone 2000), and more recently the Ca II infrared triplet (Lorenzo-Oliveira et al. 2016) emission lines. Similarly, soft X-ray emission from the corona is regularly used to relate atmospheric activity and age (Jackson et al. 2012; Booth et al. 2017).

Such correlations suggest that FGK stars should be relatively inactive once

they commence evolution to the red giant branch on the Hertzsprung-Russell diagram. Indeed, an observing program by Linsky & Haisch (1979) early in the *IUE* satellite mission showed an absence of coronal emission among a small sample of highly evolved late-type giants. However, such stars were known to possess chromospheres through earlier studies such as Wilson (1967, 1976); Deutsch (1970); Bappu & Sivaraman (1977); Stencel (1978).

The contradictions from such studies have excited active research into the surface activity levels of giant stars. Surveys of soft X-ray coronal emission among giants in different regions of the H-R diagram have been made (see e.g., Maggio et al. 1990; Haisch et al. 1991; Hünsch et al. 1996; Ayres et al. 1998; Gondoin 1999). Clarifying the absence of coronal emission among the coolest giants, Ayres et al. (1997) suggested that coronal loops are partially embedded in the chromosphere. This implies that coronae as still active into the subgiant and giant phases (see also Hünsch & Schröder 1996; Ayres et al. 2007). Far-ultraviolet emission lines arising in a transition region were studied by Linsky & Haisch (1979); Ayres et al. (1981); Simon (1984); Hartmann et al. (1985); Simon & Drake (1989); Dupree et al. (2005), for example, among samples of red giants in different stages of evolution observed with the *IUE* and *FUSE* satellites. Additionally, Ayres et al. (1982) demonstrated that observed broad C IV profiles are typical of active giant stars. Chromospheric activity in giants is less elusive to optical observation, and thus has a long history of study going back to the discovery of the Wilson-Bappu effect (Wilson & Vainu Bappu 1957).

1.2 Chromospheric Activity Through the Far-Ultraviolet Lens

High-resolution spectroscopy is often used to trace activity levels in the chromosphere and transition region. For example, Ca II emission, which originates in the chromosphere, has been a prime tool among both giant and main sequence stars. This is because the H and K Fraunhofer lines are dark in the photosphere. For wavelengths < 2000 Å, spectra of cool dwarfs contain emission lines from several sources. Sources include the chromosphere or transition region, such as $\lambda\lambda 1548, 1550$ C IV, $\lambda 1393$ Si IV, and $\lambda 1334$ C II, as well as photospheric flux (Ayres 2015). However, in the mid- to far-ultraviolet, photospheric flux is reduced for late-F, G, and K type stars, allowing chromospheric emission lines to be illuminated with greater contrast.

Table 1.1 lists emission lines which trace atmospheric activity levels of G and K-type dwarf and giant stars within an *FUV* broadband range. These emission lines were observed by Ayres et al. (1981) who conducted an *IUE* survey of cool stars. They observed the Mg II 2800 doublet to be quite prominent for both dwarfs and giants. While all emission lines listed in Table 1.1 were observed in all G-type giants, the Mg II 2800 doublet and C IV 1548,1550 lines were the most prominent for K-type giants. Some K giants were observed to emit the other lines listed in Table 1.1, but they were quite weak. Ayres et al. (1981) demonstrates that, despite the fact that the K stars have less photospheric contamination in the *FUV* band, the contrast between the chromospheric and photospheric contributions is less defined than for G stars.

The Ca II H and K emission lines of FGK type dwarf stars have been shown to

Table 1.1 Emission Lines Observed in the Atmospheres of G & K-Type Dwarf and Giant Stars (Ayres et al. 1981)

Emission	Wavelength
N V	1240
O I	1305
C II	1334
Si IV	1393
C IV	1548,1550
He II	1640
Mg II	2800

trace far-ultraviolet luminosity (Smith & Redenbaugh 2010; Findeisen et al. 2011; Smith et al. 2017). Whereas Smith & Redenbaugh (2010); Smith et al. (2017) demonstrated correlations between *GALEX* satellite *FUV* photometry and chromospheric and coronal activity, Findeisen et al. (2011) constrained relationships between the ages of FGK dwarfs and *GALEX NUV* flux, and attempted to do so with *FUV* flux. While many works have utilized coronal and chromospheric emission lines with spectroscopy as age indicators, this thesis provides a context within which *GALEX FUV* photometry can be added to the panoply of tools based on stellar activity that have been developed for the age-dating of solar-type dwarf stars.

1.2.1 The Galaxy Evolution Explorer Satellite (*GALEX*)

This thesis utilized *FUV* magnitude observations from the Galaxy Evolution Explorer satellite or *GALEX*. The primary mission within the *GALEX* All-Sky Imaging Survey (AIS) was to image a plethora of galaxies within redshift $z = 0 - 2$. The AIS covered 26,000 square degrees of the sky with a limit of mAB $\sim 20 - 21$ (Martin et al.

2003) in both a far-ultraviolet and near-ultraviolet band. The *FUV* passband relevant to this thesis covered a broad wavelength range of $1150 - 1800$ Å. The AIS also imaged thousands of dwarf stars during its cycles, observations of which are vital to this thesis. Specifically, we have utilized the *GALEX* Data Release GR6/7 catalog (Bianchi et al. 2014).

1.3 Interpreting the Milky Way's Evolution

This thesis seeks to explore the structure and evolution of stars as constituents within our galaxy. Two important relationships have guided local Milky Way evolution studies through hypothesized correlations between stellar ages, velocities, and metallicities. The first stems from the work of Twarog (1980a,b) showing an age-metallicity relationship (AMR) for main sequence stars within the Milky Way. This relation has since been used to test chemical evolution hypotheses (Casagrande et al. 2011; Holmberg et al. 2007; Holmberg 2009). The second, the age-velocity relation (AVR), suggests that older stars tend to have a larger velocity dispersion (Strömberg 1946; Spitzer & Schwarzchild 1951; Wielen 1977; Seabroke & Gilmore 2007; Soubiran et al. 2008).

The central parameter to such investigations is stellar age. However, the age-dating of stars proves to be difficult due to techniques that often rely on stellar models with varying accuracies and parameters, such as the method of interpreting isochrones (see e.g., Carlberg et al. 1985; Hänninen & Flynn 2002). Often galactic evolution studies utilize isochrone-determined ages. This thesis utilizes *FUV*-determines ages, which are derived through a purely empirical relationship, to establish a basis of understanding

chemical evolution of the Milky Way galaxy. Additionally, interpreting the AMR and AVR relationships with recent, extremely precise, astrometric observations by *Gaia*, can reveal a great deal of Galactic evolutionary information; including the evolution of the Galactic thin and thick disk populations (see e.g. Minchev 2013; Rocha-Pinto 2004).

1.3.1 The Age-Velocity Relation

The velocity dispersion of stars in our solar neighborhood increases with age. This is the so-called age-velocity dispersion relation (AVR). Constraints on this relation lend to a better understanding of the mechanisms which define the formation and evolution of the Milky Way galaxy. The velocity dispersion increasing with stellar age may be the result of several factors, including how the Milky Way initially formed. Rix & Bovy (2013) reviews the study of Galactic evolution and mechanisms that may have played a role to form its current state. One explanation being that orbits of stars were determined at birth. Vertical gradients of age and metallicity are fixed as a consequence of the initial gas settlement of the disc, and radial gradients are formed "inside out" (see e.g. Veltz et al. 2008; Robin et al. 2014; Navarro et al. 2018). The initial determination of orbits may have been the result of several mechanisms; early mergers (Brook et al. 2004, 2012), accretion from satellite galaxies (Abadi et al. 2003), or continuous star formation trends (Bird et al. 2013).

Alternately, the observed AVR is often argued to be the result of orbital scattering or dynamical heating after gas settled into a disc. As such, older stars subsequently had more time to gravitationally interact with other massive objects and to scatter. Simulations demonstrate how gravitational interactions cause heating through a variety

of mechanisms. In earlier studies, Giant Molecular Clouds (GMCs) were believed to be the main driver of Galactic heating, yet in recent years simulations have shown that multiple mechanisms contribute to the observed AVR (see, for example, Hänninen & Flynn 2002; Aumer et al. 2016). The spiral arm structure and a possible bar (Barbanis & Woltjer 1967; Aumer et al. 2016), black holes (Lacey & Ostriker 1985; Hänninen & Flynn 2002), and satellite mergers (Walker et al. 1996; Moetazedian & Just 2016; Ting & Rix 2019) may all play a role in Galactic heating.

While many works demonstrate the general upward trend of a age-velocity relation, there is no consensus on the shape of said trend. An age-velocity plot is generally fit by a power law function of the form

$$\sigma \propto \tau^{\beta}, \tag{1.1}$$

where σ is the velocity dispersion, τ is stellar age, and β is the fit parameter. The shape and fit of the trend lends to different interpretations of heating mechanisms playing a role in the formation of the Milky Way. For example, a mean velocity dispersion fit with said function resulting in a $\beta \sim 0.33$ which indicate GMCs playing a significant role in the Milky Way's heating history (Spitzer & Schwarzchild 1951). A radial velocity dispersion fit with $0.2 \leq \beta \leq 0.6$ may indicate that spiral arms are the primary heating mechanism (De Simone et al. 2004)[1].

[1]For a thorough discussion on a variety of heating mechanisms see Kumamoto et al. (2017).

1.3.2 The *Gaia* Space Telescope

Stellar ages prove difficult to pinpoint and must be inferred from other parameters. Velocities, the other vital parameter for assessing the AVR, are readily available. Fortuitously, the most precise velocity measurements to date, the Gaia Space Telescope Data Release (DR2) and early Data Release 3 (eDR3) (Gaia Collaboration et al. 2018a), were released in the genesis of this thesis work.

The *Gaia* satellite (Gaia Collaboration et al. 2016) was launched in 2013 and has since provided a wealth of information for stellar kinematic studies. The data include positional, proper motion, radial velocity, and parallax measurements. Over one billion objects were observed by the telescope, most of which were stars. DR2 also released *Gaia* photometry colors G, $G_{\rm BP}$, and $G_{\rm RP}$ (Weiler 2018) which allows for a selection of many sun-like FGK-type stars from subsequent color-magnitude diagrams (Gaia Collaboration et al. 2018a). The plethora of data from *Gaia* has significant overlap with *GALEX* observations used in these analyses.

After issuance of DR2 many stellar population studies have been and continue to be published (Mints & Hekker 2018). For example, Sanders & Das (2018) included isochrone-determined ages for around three million *Gaia* observed stars. There are also works which interpret star formation histories and kinematics of the solar neighborhood (see e.g., Bovy 2017; Gaia Collaboration et al. 2018b). This thesis utilizes empirically-derived stellar ages to interpret the solar neighborhood's evolution. Then one may compare such interpretations with those extracted using isochrone-determined ages.

1.3.3 The Age-Metallicity Relation

Like the AVR, a constructed age-metallicity relation (AMR) provides information to interpret the Milky Way's evolution in the solar neighborhood. Historically significant for it's early proposal of the age metallicity relation, Figure 4.12 shows the AMR constructed by Twarog (1980b). Metallicity estimates shown in this plot, [Fe/H], were derived using four-color and Hβ photometry. The same photometric measurements were also used to constrain physical parameters, and in turn, derive isochrone ages shown in the same figure. Here, a mixing length parameter of $Y = 1.6$ and a variable helium abundance was used. The analysis of F dwarfs stars from Twarog (1980b) showed that older stars are metal-poor and younger stars are metal-rich, with a slower increase in [Fe/H] for stars forming now.

Since being initiated by Twarog (1980b), many works have sought to construct similar AMR plots using ages and metallicities derived from a variety of observations. Such works are used to interpret the chemical evolution of the Milky Way, especially in our solar neighborhood (Rana & Basu 1992; Pilyugin & Edmunds 1996; Bensby et al. 2004; Haywood 2006; Holmberg et al. 2007; Holmberg 2009; Casagrande et al. 2011). However, there is no consensus on whether this relationship truly holds up. For example, Casagrande et al. (2011) constructed an AMR plot using thousands of stars from the Geneva-Copenhagen Survey (Nordström et al. 2004b) by re-calibrating metallicity measurements of the Survey and determining ages with isochrones. However, they saw no relationship between [Fe/H] and ages of FGK type stars in the solar neighborhood. That is, they demonstrated a consistent scatter in [Fe/H] of ~ 0.8 dex in an age range up

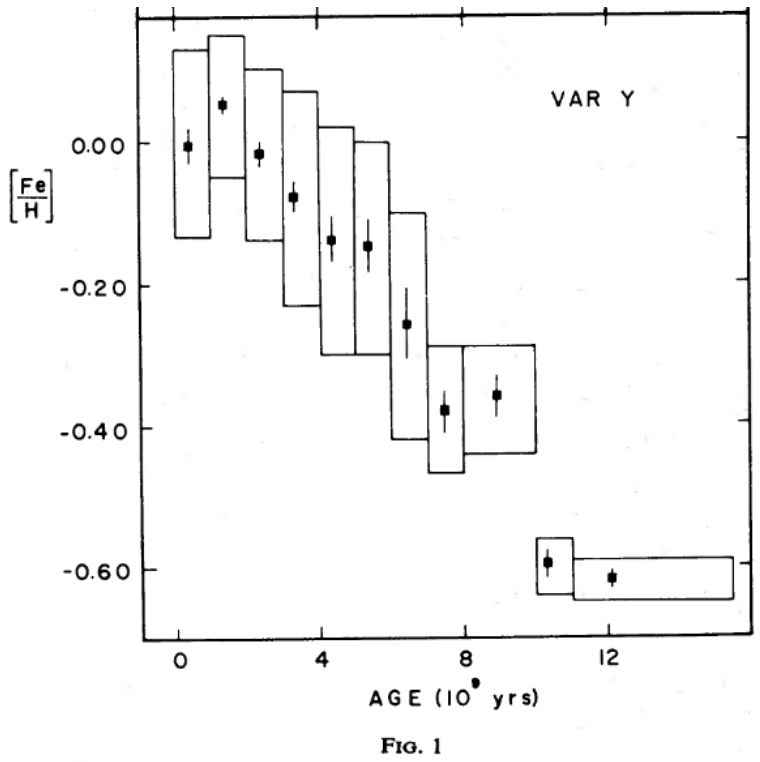

Figure 1.2 A constructed age-metallicity relation plot from Twarog (1980b) using four-color and Hβ photometry to derive [Fe/H] and isochrone age estimates.

to $\sim$ 12 Gyr. Similar to constructed AVR plots, AMR plots use isochrone-determined ages more often than not. As mentioned above, these ages can vary widely for a single star due to the assumptions made in modeling stellar evolution models.

1.3.4 The Thin and Thick Disks

The AVR and AMR help to interpret the chemical and kinematic evolution of the Milky Way. One common interpretation of the structure of the galaxy shows a model with a thin and a thick disk. Historically, the existence of such structure stems from observations of external, lenticular-type galaxies (Burnstein 1979; Tsikoudi 1979), which where then identified within the Milky Way (Gilmore & Reid 1983). There are

two broad possibilities for the thick disc formation: the disc formed in situ or it is a "puffed up" version of the thin disc.

In the former scenario early star formation produced metal poor stars which maintained their scale heights after the surrounding gas collapsed into the Galactic plane (Veltz et al. 2008; Robin et al. 2014; Navarro et al. 2018). These stars are identified as intermediate Population II, thick disc stars. Younger Population I, thin disc, stars formed later in the collapsed disc. A similar scenario describes a major merger (Veltz et al. 2008), or several mergers (Brook et al. 2004) early on in the Milky Way's formation history in which accretion formed the thick disc stars in situ. In this case, the merger(s) must have occurred before the gas forming the thin disc fully settled. Otherwise, major disruptions of the thin disc would have manifested.

Alternatively, thick disc stars may have larger scale heights than thin disc stars due to dynamical heating. Early in the Milky Way's formation a rapidly spinning gas cloud collapsed and settled (as described, for example, in Eggen et al. 1962). The thick disc stars then formed and their orbits have been heated or "puffed" up to greater distances above the Galactic mid-plane. Thin disc stars were formed later and have not experienced the same amount of scatter. Several mechanisms may have contributed to the observed heating (Hänninen & Flynn 2002; Aumer et al. 2016) which likely include scatter from Giant Molecular Clouds and/or black holes (Lacey & Ostriker 1985; Hänninen & Flynn 2002). Heating may have been a consequence of the Milky Way's spiral structure or a possible bar (Barbanis & Woltjer 1967; Aumer et al. 2016). Additionally, minor mergers from satellite galaxies may have played a role (Walker et al.

1996; Moetazedian & Just 2016; Ting & Rix 2019).

There is a long history of exploring the definitions of the thin and thick disk populations and their formation histories. However, investigations also include the possible nonexistence of the two populations. For example, Bovy et al. (2012) find no distinct populations, and that the thick disc is a tail of a continuous scale-height distribution.

Investigations of these stellar populations usually use isochrone-determined ages which have varying accuracies. However, several investigations make use of chromospheric activity indicators, like Ca II H and K emission line strengths, to infer formation histories and to document the AMR and AVR (see e.g., Rocha-Pinto 2004; Reid et al. 2007; Jenkins et al. 2011). This thesis expands on such explorations by employing an empirical relationship between FUV emission and stellar age to interpret the Milky Way's evolution and its stellar populations.

1.4 Outline of This Work

This thesis is composed of two main investigations. In the first, I have constrained a relationship between FUV emission as a chromospheric activity indicator, and age of FGK dwarf stars. Furthermore, I have explored the FUV-activity relationship for evolved giants. The second investigation explores the use of empirically derived, FUV-determined ages to construct AMR and AVR plots in order to interpret the Milky Way's evolution within our Solar neighborhood. The outline of this work is as follows:

Chapter 2 calibrates the FUV-age relationship for a sample of stars with John-

son $(B-V)$ colors, literature-reported ages, and *GALEX* far-ultraviolet observations. As an illustration of population studies of FGK dwarfs for further understanding of the chemical evolution of the Milky Way, I constructed activity and FUV-age distributions for a sample of thin and thick disc stars. Chapter 3 investigates the more elusive FUV-activity relationship in red giant stars. Therein I examine correlations between four chromospheric and coronal activity indicators. In Chapter 4, I re-calibrate the FUV-age relationship in *Gaia* color space, as *Gaia* photometry is available to anyone and one need not obtain $(B-V)$ photometry. I then utilize the updated FUV-age calibration to determine model-independent ages of hundreds of stars in the Geneva-Copenhagen Survey. An AVR and AMR is constructed using FUV-determined ages and unprecedentedly precise *Gaia* kinematics. I fit the AVRs with a power law function and compare to AVRs within the literature. In addition, I show that perigalactic and eccentricity versus FUV-age plots are consistent to an "inside out" model. Finally, Chapter 5 summarizes this thesis and discusses future work.

Chapter 2

Estimating the Ages of FGK Dwarf Stars with GALEX FUV Magnitudes

2.1 Introduction

An understanding of stellar evolutionary processes requires a knowledge of stellar age. There exists a long history of creative techniques used to determine ages. For an extensive review of stellar-age dating techniques see Soderblom (2010). Accurate stellar ages remain an important input for modeling stellar structure and evolution. Additionally, age inputs are needed to employ stars as chemical evolution tracers of the Milky Way and nearby galaxies (see, e.g. Layden & Sarajedini 2000; Holmberg et al. 2007; Koch et al. 2007; Schuster et al. 2012; Haywood et al. 2013; Piatti & Geisler 2013;

Soderblom 2015)

Possibly the most widely-used stellar-age dating technique is isochrone fitting. This technique makes use of color-magnitude diagrams among varied-age stellar populations. There exists a plethora of models and statistical analyses used to determine isochrone ages. However, there is often significant scatter between ages determined from different isochrone models, especially for older stars.

In more recent years the Bayesian method used to determine ages has proven to reduce scatter as compared to traditional isochrone fitting methods (see, e.g. Pont & Eyer 2004; Jørgensen & Lindegren 2004). Utilizing the Bayesian method and Gaia DR1 parallax measurements, Lin et al. (2018) have shown that their isochrone-determined ages are similar to those found in the literature with reduced uncertainties for younger stars. However, for stars greater than $\sim$ 2 Gyr their sample has larger scatter as compared to other well-studied ages found in the literature. In another chromospheric activity-age relationship work by Mamajek & Hillenbrand (2008), they find a calibration with an age precision of $\pm$ 0.25 dex or 60% (1 σ). Such scatter illustrates a need for additional types of age-dating techniques which may be applied to dwarf stars, such as activity ages, lithium ages, or gyrochronology ages. Then one may compare age estimates of stars determined by a variety of methodologies. This paper focuses on a purely empirical age-dating technique which has not been extensively calibrated to date, in which far-ultraviolet (FUV) photometry is mapped directly to stellar age.

Magnetic field strengths of main-sequence stars decrease as they age and rotation speeds slow. It has been shown for FGK dwarfs that stellar chromospheric activity

is directly related to magnetic field strength (Skumanich 1972). Hence, such stars may be dated by measuring their level of chromospheric activity and correlating this against age (see, e.g. Soderblom et al. 1991; Pace & Pasquini 2004; Mamajek & Hillenbrand 2008; Jackson et al. 2012; Booth et al. 2017).

Chromospheric and coronal radiation, such as Ca II H and K and soft X-ray emission, are often used as stellar activity indicators, and hence age. The Ca II H and K emission lines from late-F, G, and K type dwarf stars have been shown to trace *FUV* luminosity (Smith & Redenbaugh 2010; Findeisen et al. 2011; Smith et al. 2017). Whereas Smith & Redenbaugh (2010) and Smith et al. (2017) demonstrated correlations between the Galaxy Evolution Explorer (*GALEX*) satellite *FUV* photometry and chromospheric and coronal activity, Findeisen et al. (2011) constrained relationships between the ages of FGK dwarfs and *GALEX* near-ultraviolet (NUV) flux. They also attempted to do so with *FUV* flux. While many works have utilized coronal and chromospheric emission lines as age indicators, such as relationships between $\log R'_{\rm HK}$ and age,[2] the study presented in this paper provides a context within which *GALEX FUV* photometry can be added to the panoply of tools based on stellar activity that have been developed for the age dating of solar-type dwarf stars.

This chapter of the thesis has utilized solar-analog field dwarf stars plus representative moving group and open cluster stars to calibrate an *FUV*-age relationship. Such a technique that does not rely on models, but rather a purely empirical relationship, adds to the toolbox of age-dating techniques. The sample of stars used in the *FUV*-age calibrations is discussed in Section 2.2. Section 2.3 outlines the analysis per-

[2] An example of this relationship is demonstrated in Section A.1 of Appendix A

formed to achieve said calibrations. Section 2.4 explores a consistency check using the NGC 752 open cluster. In Section 2.5 we investigate FUV-determined ages and activity levels of thin and thick disk stars designated by their chemical abundances. Finally, Section 2.6 discusses some potential uses of the calibration.

2.2 The Age-Calibration Star Sample

This chapter demonstrates a method for estimating ages of solar-like dwarf stars from FUV magnitudes. We considered stars in the color range $0.55 \leq (B-V) \leq 0.70$, which covers a solar-analog range while also including both hotter and cooler stars. In order to develop an age-FUV calibration we have utilized a sample of late-F, G, and K type dwarf stars with solar-like luminosities, metallicities, and spectral types. By restricting our attention to late-F, G, and early-K dwarfs we have calibrated the age-FUV relationship with stars whose stellar activity is governed by a set of physical mechanisms that are analogous to those producing the activity of the Sun.

We have compiled a calibration sample of such stars having *GALEX* FUV magnitude data and for which age determinations are found in published literature. Data for this calibration sample were used to derive a relation between an FUV-based stellar color and stellar age. Since the FUV spectra of G-type dwarfs are expected to be age-sensitive due to the influence of chromosphere and transition region emission lines, we have sought a sample of calibration stars with ages in the literature that have predominantly been derived from stellar activity indicators such as the Ca II H and K lines (see, e.g. Lorenzo-Oliveira et al. 2018). *GALEX* FUV magnitude measurements

used in this work were collected from the GR6/7 data release, mostly from the All-Sky Imaging Survey, through the Mikulski Archive for Space Telescopes (MAST) (Conti et al. 2011).

For age-calibration purposes a sample of solar-analog stars with a range of ages was needed. Cluster stars with ages greater than the Sun are too faint for *GALEX* observations, so field stars compose the sample used herein. Field star catalogs which accommodate all of the previously noted requirements were narrowed down to Ballering et al. (2013), Isaacson & Fischer (2010), Sierchio et al. (2014) and Lorenzo-Oliveira et al. (2018). The oldest star in the sample is 9.0 Gyr. Ages reported in Ballering et al. (2013) and Sierchio et al. (2014) were primarily determined using chromospheric activity and X-ray luminosity indicators. These ages were supplemented with surface gravity measurements and gyrochronology if available, and were checked to be consistent with isochrone estimates. Ages from Isaacson & Fischer (2010) were determined by chromospheric activity indicator $\log R'_{HK}$ and calibrations from Mamajek & Hillenbrand (2008). Quoted ages from Lorenzo-Oliveira et al. (2018) were determined via Yonsei-Yale isochrones (Yi et al. 2001; Kim et al. 2002). Stars which fell in more than one catalog were treated separately. Their ages were not averaged as the methods used to determine ages are not always comparable. Stars with significant diskrepancies in age were accounted for in a two-step calibration process (see Section 2.3). An initial calibration of the FUV-age relation was performed for each individual catalog (Ballering et al. 2013, Isaacson & Fischer 2010, Sierchio et al. 2014 and Lorenzo-Oliveira et al. 2018). Stars from any individual catalog were removed if determined to be outliers.

Then a collection of the remaining stars were combined for a final calibration.

All field stars in the compiled calibration sample are solar analogs, that is, they have similar spectral types and luminosities to that of the Sun. Selected stars have absolute magnitudes within ±0.5 mag of the Sun (i.e. they fall within $4.3 \leq M_{\rm V} \leq 5.3$). Stars more luminous than this threshold have weakened Ca II H and K and are less likely to give reliable information on chromospheric ages. In addition, selected stars fall into a solar-analog color range of $0.55 \leq (B-V) \leq 0.71$. Parallaxes used to determine $M_{\rm V}$ were collected from SIMBAD (Wenger et al. 2000) with the majority belonging to the Gaia catalog, while $(B-V)$ colors and V magnitudes were collected from the *Hipparcos* catalog.

As for metallicity, 76% of collected stars with [Fe/H] measurements fall within a solar-like range of $-0.2 \leq$ [Fe/H] ≤ 0.2. Most metallicity measurements were gathered from Casagrande et al. (2011) and Valenti & Fischer (2005). Stars which had measurements from both catalogs were compared and were found to have consistent [Fe/H] values (See Section A.2 of Appendix A). However, 30 stars did not have metallicity measurements in either Casagrande et al. (2011) or Valenti & Fischer (2005). Figure 2.1 shows the distribution of metallicities for stars which have measurements. The metallicities of the calibration stars peak near the solar abundance and have a dispersion about the solar [Fe/H] of around 0.3 dex, although there is a small tail to lower abundances.

The reader may be concerned with metallicity effects contributing to errors in an FUV-age relationship. As discussed below, in our age calibration methodol-

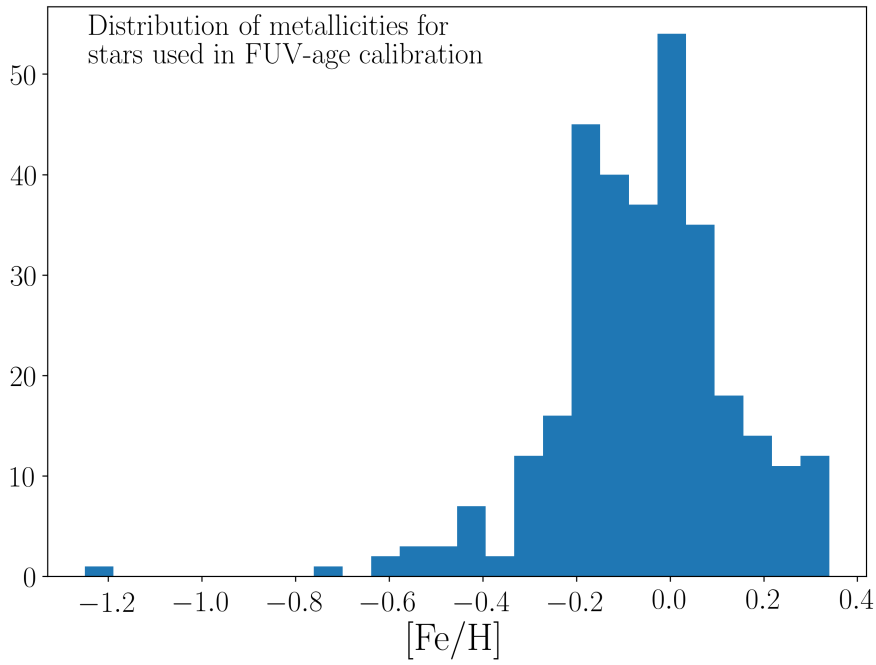

Figure 2.1 A distribution of metallicities, [Fe/H], for stars considered in the FUV-age calibration. Of the collected stars, 76% with [Fe/H] measured fall within a solar-like range of $-0.2 \leq$ [Fe/H] ≤ 0.2. However, 17 stars used in this work do not have a metallicity estimate.

ogy we divided the stellar sample into metallicity ranges $-0.8 \leq$ [Fe/H] < -0.2, $-0.2 \leq$ [Fe/H] < 0.1, $0.1 \leq$ [Fe/H] < 0.5, or those which have no metallicity estimate quoted in Casagrande et al. (2011) (see Figure 2.5 as an example). We found no correlations between metallicity and our derived FUV-age relationships. Our age calibrations nonetheless can be seen from Figure 2.1 to be most applicable to FGK dwarfs with near-solar abundances.

The *GALEX* FUV magnitude was combined with the Johnson B magnitude to give a color that is denoted here as $(FUV - B)$. Stellar parameters including HD identifier, V and B magnitudes, $(FUV - B)$ color, and literature-reported ages for the field stars used in this analysis are found in Section B.1 of Appendix B to this thesis

(Table B.1). Not all stars from the four catalogs are listed in this table, but instead those with the magnitude restrictions listed in this section.

In addition to the field stars, representative dwarf stars within the Hyades and Coma Berenices open clusters were utilized from Smith (2018) in which two-color diagrams were constructed using *GALEX* FUV and Johnson B and V magnitudes. Lastly, representative moving group main sequences from Cochrane & Smith (2019), in which FUV-age correlations were demonstrated, were incorporated into the sample. Stars from both the cluster and moving group compilations were only included if they fell within the restricted color range: $0.55 \leq (B-V) \leq 0.75$.

2.3 Age Calibration

Figure 2.2 shows the two-color diagram, $(FUV-B)$ versus $(B-V)$, for field stars from Sierchio et al. (2014), Ballering et al. (2013), Isaacson & Fischer (2010), and Lorenzo-Oliveira et al. (2018)[3]. As described in Smith & Redenbaugh (2010) and Smith et al. (2017), varied chromospheric emission levels cause significant differences in $(FUV-B)$ at any given $(B-V)$. Figure 2.2 demonstrates such scatter in $(FUV-B)$, particularly in the color range $0.55 \leq (B-V) \leq 0.80$.

The analysis reported here has utilized an upper envelope (denoted in red in Figure 2.2) which describes an empirical minimum chromospheric FUV emission among FGK dwarf stars (Smith et al. 2017). This envelope was chosen to pass through the

[3]Note that not all field stars in this diagram are used to calibrate the FUV-age relation, as the calibration only uses stars that fall within $0.55 \leq (B-V) \leq 0.70$. Stars hotter than this limit tend to have substantial photospheric flux at FUV wavelengths, and there are too few stars to consider proper correlations redward of this limit. In addition, not all stars in Figure 2.2 fall within the solar-analog absolute magnitude range.

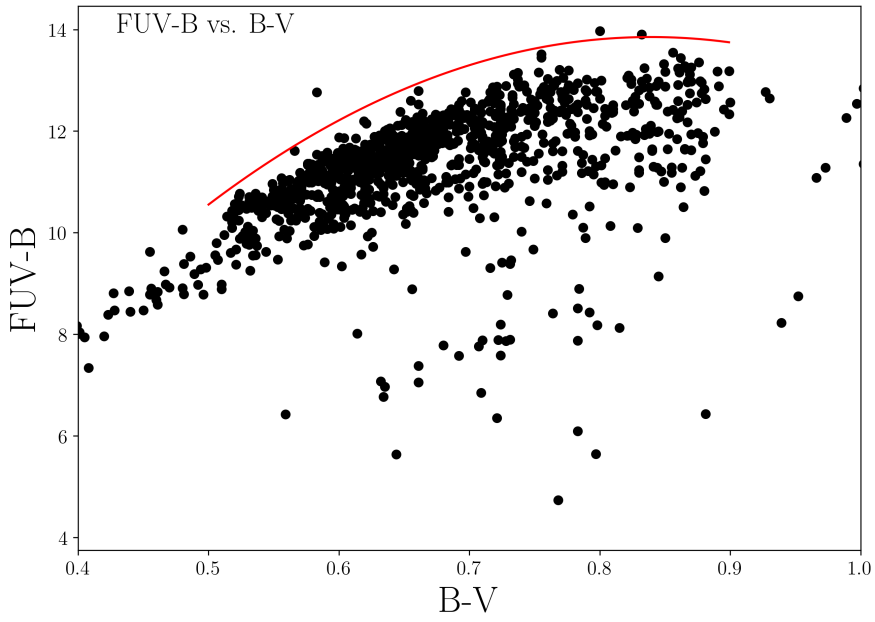

Figure 2.2 A two-color diagram of $(FUV-B)$ versus $(B-V)$ for field stars from Sierchio et al. (2014), Ballering et al. (2013), Isaacson & Fischer (2010), and Lorenzo-Oliveira et al. (2018). Duplicate stars are not shown. Significant differences in $(FUV-B)$ at any given $(B-V)$ indicate differences in chromospheric FUV emission levels. The red line denotes an upper envelope constraint used to demonstrate a minimum level of chromospheric activity.

upper-most points in Figure 2.2. A least-squares polynomial fit was used to determine the envelope as described by

$$u_{\mathrm{FUV}} = -28.70(B-V)^2 + 48.16(B-V) - 6.35. \tag{2.1}$$

Consistent with Smith & Redenbaugh (2010), the upper envelope flattens out and becomes less defined with increasing $(B-V)$ (corresponding to redder dwarfs). All further analyses in this work incorporated the upper envelope for all dwarfs within the FUV-

excess parameter, $Q(FUV - B, B - V)$, defined for each star by

$$Q = (FUV - B) - u_{\rm FUV}. \tag{2.2}$$

The color difference index, Q, indicates a comparative level of chromospheric activity (relative to the upper envelope of Equation 4.3) as a function of *GALEX* far-ultraviolet and Johnson B and V magnitudes. As such we would anticipate that Q varies with the age of FGK dwarfs.

Figure 2.3 provides an illustration of the Q parameter as an indicator of chromospheric activity levels. Here, two stars used in the FUV-age calibration with solar-like colors, yet with different ages, were compared using International Ultraviolet Explorer (IUE) spectra collected from MAST (Conti et al. 2011). HD 76151 (top) with an age of $\tau = 1.8$ Gyr, $(B - V) = 0.67$ and [Fe/H]=0.11 has a more positive Q value ($Q = -1.39$) as compared to HD 1835 (bottom) with $\tau = 0.6$ Gyr, $(B - V) = 0.66$, [Fe/H] $= 0.25$ and $Q = -1.96$. A more positive Q indicates lower chromospheric activity levels as seen in the far-ultraviolet. Figure 2.3 shows the Mg II doublet emission lines around 2800 Å. This doublet has been shown to correlate with Ca II H and K lines (e.g Doherty 1985) and hence chromospheric activity levels. HD 1835 has stronger Mg II lines than HD 76151, indicating higher activity levels. This is consistent with a more negative Q for HD 1835.

The physical relationship between age and FUV-excess parameter, Q, that we

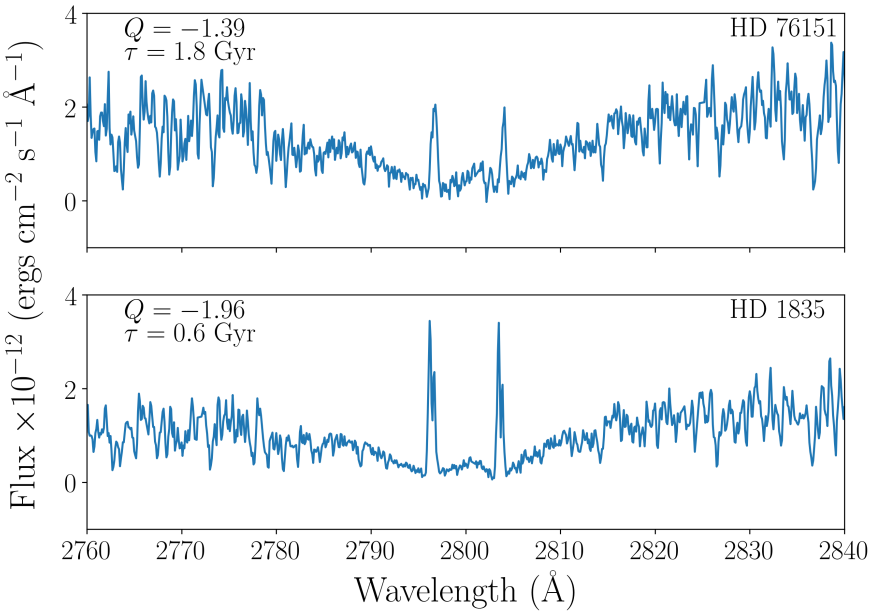

Figure 2.3 International Ultraviolet Explorer (IUE) spectra of two stars with solar-like $(B-V)$ color. HD 1835 (bottom) is younger and has a more negative Q value than HD 76151 (top). The Mg II lines near 2800 Å are stronger for HD 1835 than HD 76151, and as Mg II indicates chromospheric activity, this figure illustrates that FUV photometry, and hence Q, also traces activity levels.

adopted is described by the exponential function

$$\tau = ae^{bQ}, \tag{2.3}$$

and where τ is age in gigayears, and a and b are exponential coefficients. This relationship is purely empirical. To obtain values of the coefficients a and b, simple linear fits were made between Q and the natural logarithm of age within a set of various $(B-V)$ ranges. These fits take the form

$$\log_e(\tau) = \log_e(a) + bQ. \tag{2.4}$$

2.3.1 Initial Age-Calibration Fits

Plots of literature-reported age[4] versus Q were initially constructed for each of the individual field catalogs separately (Sierchio et al. 2014; Ballering et al. 2013; Isaacson & Fischer 2010; Lorenzo-Oliveira et al. 2018). For those stars which fell within our visual absolute magnitude constraints, we found that there exists significant scatter in age versus Q among dwarfs with $(B-V) > 0.70$. As such we limited an initial calibration effort to stars within the three $(B-V)$ color ranges: $0.55 \leq (B-V) < 0.60$, $0.60 \leq (B-V) < 0.65$, and $0.65 \leq (B-V) \leq 0.70$.

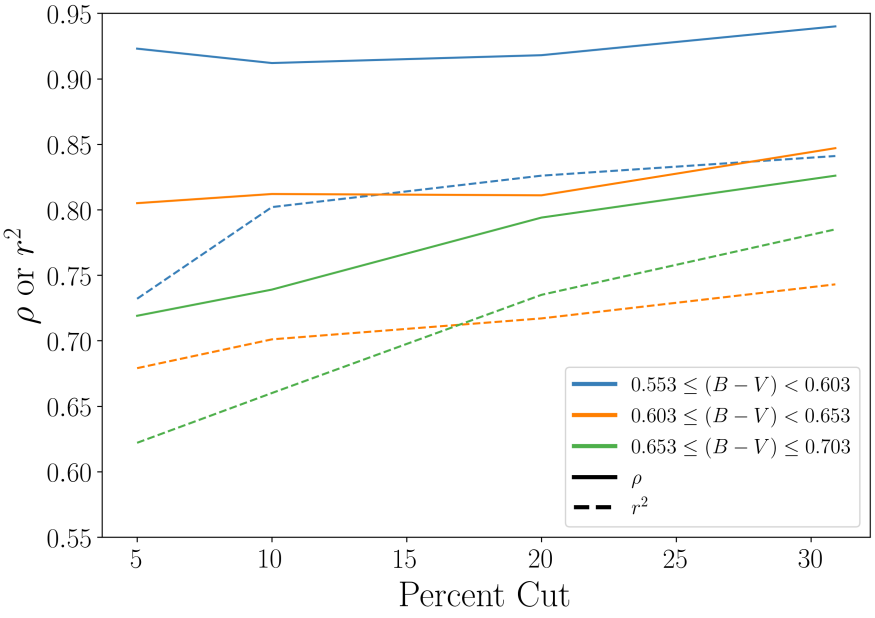

Figure 2.4 Spearman's correlation coefficient (solid line) and coefficient of determination (dashed line) of field stars from the combined (Sierchio et al. 2014; Ballering et al. 2013; Isaacson & Fischer 2010; Lorenzo-Oliveira et al. 2018) catalog after percentage cuts were performed on individual catalogs. Varied colors represent $(B-V)$ bins. Field stars were considered outliers and were cut if they fell within the furthest 5%, 10%, 20%, and 30% residuals about the Q versus τ fits made for each individual catalog.

[4]The literature-reported ages adopted in these plots were estimated using several methods as described above.

Outliers were determined for each catalog [5] based on distance from the linear fit (Equation 2.4) for each color range. Sigma clippings were difficult to achieve, as the majority of the literature-reported ages for the calibration stars are not accompanied with errors. Instead, 5%, 10%, 20%, and 30% clippings were performed on each individual field star catalog within each of the three $(B-V)$ color bins to determine reasonable percentage clippings. That is, linear fits of the form of Equation 2.4 were performed on Q versus $\log_e(\tau)$ for each individual field star catalog, and field stars were considered potential outliers if they fell within the furthest 5%, 10%, 20%, and 30% of said fits. A separate compilation was made of all stars that were not cut at each of the four clipping levels tried and the resulting r^2 and ρ were calculated. Figure 2.4 shows these parameters for each color bin and each trial percentage cut. The points at which the curves in Figure 2.4 flatten out were considered as a basis for choosing a final percentage cut level for each $(B-V)$ color bin. Final cuts were chosen to be 10%, 10%, and 20% of the field stars in color bins $0.55 \leq (B-V) < 0.60$, $0.60 \leq (B-V) < 0.65$, and $0.65 \leq (B-V) \leq 0.70$, respectively. These finalized percentages represent the highest cut below which ρ and r^2 variate significantly. The percentages were applied uniformly to each individual catalog at this stage of the analysis.

Table 2.1 shows fits for each clipped field star catalog (Sierchio et al. 2014; Ballering et al. 2013; Isaacson & Fischer 2010; Lorenzo-Oliveira et al. 2018) in three color bins: $0.55 \leq (B-V) < 0.60$, $0.60 \leq (B-V) < 0.65$, and $0.65 \leq (B-V) \leq 0.70$. These fits are considered the initial fits. Table 2.1 displays the average color for the

[5] Each of the field star catalogs were fit individually at this stage of the analysis, as they contain ages derived by a range of techniques. Ages were not averaged since they may not be comparable in a straightforward manner.

stars within each bin $\langle B-V \rangle$, fit parameters a and b, and indicators of correlation and fit, r^2 and ρ. In almost all cases r^2 and ρ improve when ignoring outliers. The reader may note the variation of a and b parameters between color bins of Table 2.1. As will be demonstrated in more detail below, the fit parameters a and b do indeed appear to be functions of $(B-V)$, i.e., they vary with stellar effective temperature, and so a methodology of choosing a fitting function such as Equation 2.4 does need to take this temperature dependence into account. These variations in a and b are considered explicitly in the derivation of more refined fits, which are discussed below (and summarized in Table 2.2).

2.3.2 Refined Age-Calibration Fits

After outliers were cut from each individual catalog (adopting the finalized percentage cuts noted above), the accepted stars were again complied into one data set, 344 stars in total. Entries for any star that appeared in multiple catalogs were treated separately, as many had different age estimates. In other words, a number of stars have more than one entry in the final merged calibration catalog. Rather than using three $(B-V)$ color bins, we used a total of 12 bins in order to obtain more refined Q-age fits in the case of this combined final catalog. These bins range from $(B-V) = 0.55$ to $(B-V) = 0.71$ and have widths of $(B-V) = 0.05$. Such bins allow for a more continuous fit when calibrating the relationship between τ and Q as a function of $(B-V)$. A flattening of the Q versus τ relation was noticed among the lowest activity stars for a number of $(B-V)$ bins (see Figure 2.5). Slope changes occur at different Q values for each bin anywhere between $Q = -0.7$ to $Q = -0.98$. As such

Table 2.1 Age Calibration Fits for FUV-Excess Parameter Q: Initial Fits[a]

Isaacson & Fischer Field Stars								
B-V Bin	$\langle B-V\rangle$[b]	a	b	N[c]	ρ^{d}	r^{2d}	ρ^{e}	r^{2e}
0.55-0.60	0.59	23.58	2.33	35	0.83	0.71	0.87	0.81
0.60-0.65	0.63	35.51	2.15	74	0.78	0.65	0.77	0.70
0.65-0.70	0.68	29.39	1.72	75	0.74	0.61	0.83	0.76
Ballering et al. Field Stars[f]								
B-V Bin	$\langle B-V\rangle$[b]	a	b	N[c]	ρ^{d}	r^{2d}	ρ^{e}	r^{2e}
0.55-0.60	0.58	29.43	2.64	25	0.94	0.78	0.95	0.82
0.60-0.65	0.63	44.81	2.48	25	0.86	0.70	0.93	0.76
0.65-0.70	0.68	29.42	1.79	16	0.87	0.85	0.81	0.84
Sierchio et al. Field Stars								
B-V Bin	$\langle B-V\rangle$[b]	a	b	N[c]	ρ^{d}	r^{2d}	ρ^{e}	r^{2e}
0.55-0.60	0.58	21.58	2.43	17	0.88	0.64	0.88	0.72
0.60-0.65	0.63	41.74	2.40	20	0.83	0.77	0.90	0.86
0.65-0.70	0.68	44.49	2.16	17	0.84	0.77	0.84	0.75
Lorenzo et al. Field Stars[g]								
B-V Bin	$\langle B-V\rangle$[b]	a	b	N[c]	ρ^{d}	r^{2d}	ρ^{e}	r^{2e}
0.55-0.60	n/a	n/a	n/a	0	n/a	n/a	n/a	n/a
0.60-0.65	0.64	28.71	2.03	20	0.66	0.44	0.68	0.45
0.65-0.70	0.67	9.06	0.41	20	0.52	0.34	0.40	0.15

[a] No restrictions were taken on Q values during the initial fit.

[b] Corresponds to the average $(B-V)$ color of the stars within the bin.

[c] Number of stars in the sample after outliers were cut.

[d] Spearman coefficient and the coefficient of determination for the fit before excluding outliers.

[e] Spearman coefficient and the coefficient of determination for the fit after excluding outliers.

[g] There were no stars to fit within color bin $0.55 \leq (B-V) < 0.60$ within this catalog.

we have only fit to those stars with a Q more negative than the value at which each τ-Q relation flattens out in each $(B-V)$ bin. We note that the flattening may not be as prominent in the $0.65 \leq (B-V) \leq 0.70$ range due to a lack of measurements with $Q > -1.0$ in this regime. Figure 2.5 shows four examples of the age versus Q fits calibrated utilizing our final merged field star catalog. The refined fits are shown in red.

Table 2.2 (top section) enumerates the refined-fit parameters denoted (a,b) as well as the coefficient of determination (r^2), the Spearman coefficient (ρ), and rms of the $\log(\tau)$ about each fit for each color bin. We found strong correlations between age and FUV parameter Q as demonstrated by the large ρ values.

We then fit the parameters a and b across the different color bins to investigate how they vary with the $(B-V)$ color of a dwarf star. Figure 2.6 shows that a and b as a function of $(B-V)$ may be fit with a quadratic curve. The $(B-V)$ value used for each point is the median color within each bin. The fits correspond to

$$a = -7282.49(B-V)^2 + 9526.26(B-V) - 3047.12 \tag{2.5}$$

and

$$b = -66.58(B-V)^2 + 79.66(B-V) - 21.22. \tag{2.6}$$

Given Equations 4.3, 3.4, 2.4, 2.5, and 2.6 one may calculate an age for an FGK dwarf star from *GALEX* FUV and Johnson $(B-V)$ magnitudes. Alternatively, one could make use of Equations 4.3, 3.4, and 2.4 and interpolate within the grid of a and b values listed in Table 2.2.

Table 2.2 Age Calibration Fits for FUV-Excess Parameter Q: Refined Fits[a]

Fit of Field Stars without Outliers [b]								
$(B-V)$ Bin	Rep. $(B-V)$[c]	a	b	N[d]	ρ[e]	r^2[f]	$Q_{\max}$[g]	rms[h]
0.55-0.60	0.575	33.98	2.68	69	0.88	0.84	-0.70	0.44
0.56-0.61	0.585	29.33	2.50	87	0.86	0.80	-0.70	0.52
0.57-0.62	0.595	32.69	2.51	95	0.85	0.78	-0.75	0.52
0.58-0.63	0.605	49.36	2.64	116	0.89	0.83	-0.80	0.54
0.59-0.64	0.615	53.39	2.60	135	0.86	0.82	-0.85	0.55
0.60-0.65	0.625	64.72	2.59	138	0.87	0.84	-0.90	0.53
0.61-0.66	0.635	63.13	2.48	150	0.89	0.86	-0.90	0.49
0.62-0.67	0.645	67.62	2.44	164	0.86	0.84	-0.92	0.51
0.63-0.68	0.655	75.98	2.42	152	0.87	0.84	-0.98	0.47
0.64-0.69	0.665	76.67	2.36	136	0.89	0.86	-0.98	0.44
0.65-0.70	0.675	65.03	2.24	131	0.89	0.85	-0.98	0.46
0.66-0.71	0.685	52.03	2.04	102	0.89	0.86	-0.98	0.37
Fits of Field Stars + Moving Groups + Clusters								
$(B-V)$ Bin	Rep. $(B-V)$[c]	a	b	N[d]	ρ[e]	r^2[f]	$Q_{\max}$[g]	rms[h]
0.55-0.60	0.575	32.09	2.65	76	0.88	0.85	-0.85	0.43
0.56-0.61	0.585	28.47	2.49	94	0.85	0.80	-0.87	0.51
0.57-0.62	0.595	31.30	2.49	102	0.84	0.79	-0.90	0.51
0.58-0.63	0.605	48.39	2.64	124	0.88	0.82	-0.85	0.55
0.59-0.64	0.615	54.56	2.62	143	0.87	0.82	-0.87	0.55
0.60-0.65	0.625	65.58	2.60	146	0.87	0.84	-0.90	0.53
0.61-0.66	0.635	68.75	2.54	158	0.90	0.85	-0.93	0.51
0.62-0.67	0.645	81.89	2.56	172	0.89	0.84	-0.94	0.52
0.63-0.68	0.655	73.60	2.42	160	0.87	0.85	-0.96	0.48
0.64-0.69	0.665	72.68	2.35	144	0.87	0.85	-1.00	0.47
0.65-0.70	0.675	61.96	2.24	139	0.88	0.84	-1.00	0.48
0.66-0.71	0.685	53.16	2.09	110	0.87	0.85	-1.00	0.41

[a] Fits were restricted to $< Q_{\max}$ depending on the $(B-V)$ bin.

[b] The refined fits for the compiled field star catalog after excluding outliers from individual catalogs.

[c] Corresponds to the representative $(B-V)$ color of each bin which is used to further constrain the $(B-V)$ color dependence of the parameters a and b.

[d] Number of stars within each bin.

[e] Spearman coefficient

[f] Coefficient of determination

[g] Within each bin we do not fit to stars with values of Q greater than $Q_{\max}$.

[h] rms of $\log(\tau)$ about each fit.

Often age estimates of coeval groups of stars are assumed to be more reliable than those estimated for individual field stars, as coeval population ages are determined using larger number statistics. We were motivated to incorporate moving groups and open clusters in addition to the collection of field stars in our calibration efforts.

Cochrane & Smith (2019) collected dwarf stars from 11 moving groups and performed polynomial fits of far-ultraviolet $(FUV - B)$ color as a function of Johnson $(B-V)$ color (see Table 13 of Cochrane & Smith 2019) for each individual group. Their main sequence two-color fits are of the form

$$(FUV - B) = \sum_{n=0}^{5} c_n (B - V)^n. \tag{2.7}$$

We estimated $(FUV - B)$ colors for main sequences of the moving groups listed in Cochrane & Smith (2019) using Equation 2.7 and representative values of $(B-V)$ equal to the midpoint colors for each of the 13 bins in Table 2.2. We have used the fitted $(FUV - B)$ versus $(B - V)$ relationships from Cochrane & Smith (2019) to account for scatter in the original observational data from which these relationships were derived. We chose not to try to refit their original stellar group data. These $(FUV-B)$ estimates were used to determine Q with Equation 3.4.

Main-sequence stars from the Hyades and Coma Berenices open clusters were fit to determine $(FUV - B)$ versus $(B - V)$ relationships by Smith (2018). For the Hyades cluster the best-fit line in the color range $0.30 \leq (B - V) \leq 0.60$ is given by

$$(FUV - B) = 4.47(\pm 0.38) + 10.08(\pm 0.80)(B - V), \tag{2.8}$$

while the Coma Berenices cluster has a best-fit line of

$$(FUV - B) = 3.84(\pm 0.18) + 11.32(\pm 0.41)(B - V) \tag{2.9}$$

in the color range $0.10 \leq (B - V) \leq 0.60$. These fits are only applicable for the first three color bins listed in Table 2.2. Representative values of $(B - V)$ were used to determine $(FUV - B)$ and then Q for the Hyades and Coma Berenices main sequences for each of these first four color bins.

The collection of dwarf field stars, excluding outliers, along with representative stars for each moving group and cluster were fit to Equation 2.4 for each of the color bins in Table 2.2. Fits were restricted to the FUV-excess range of $Q \lesssim -1.0$ for the reasons explained above. Figure 2.7 shows four examples of literature-reported ages versus FUV-excess parameter, Q, for field stars, moving group representatives, and cluster representatives. The red line represents the overall linear fit. The linear coefficients of fit (a and b), the coefficient of determination (r^2), the Spearman coefficient (ρ), and rms for the final $\log(\tau)$-Q fits are shown in the bottom section of Table 2.2. Again, we found significant correlations between τ and Q given the values of ρ for each bin.

The a and b parameters derived from our *combination* of field stars, moving group fiducial points, and cluster fiducial points were then fit by quadratic functions of $(B - V)$. These fits shown in Figure 2.8 resulted in the following equations

$$a = -9188.19(B - V)^2 + 11938.67(B - V) - 3807.59 \tag{2.10}$$

$$b = -80.79(B-V)^2 + 98.05(B-V) - 27.13. \quad (2.11)$$

These equations along with those in Equations 4.3, 3.4, and 2.4 may be used to estimate ages of FGK solar-type stars given FUV magnitudes and $(B-V)$ color. Alternatively interpolations can be made within the grid of a and b values in the lower half of Table 2.2.

We found that for redder stars the moving group points shift progressively away from the field star fits. This offset is not seen for solar-like $(B-V)$ colors, and the most reliable ages from the calibrations are therefore considered to be those derived for true solar analogs with $(B-V) = 0.55-0.65$. The ages used for the moving groups are isochrone-determined, and this may indicate that the isochrone ages are becoming systematically offset from the activity-age scale defined by the field stars as one moves into the K spectral type along the main sequence. Alternatively, the offset may reflect uncertainties in the ages adopted from the literature for some of the calibration stars. It is for this reason that we provide several calibrations of the Q parameter against stellar age using isolated field stars and a combination of open clusters, moving groups, and field stars.

Figure 2.5 investigates whether stellar metallicity might affect ultraviolet colors used in our FUV-age calibrations. Stars used in the calibration were divided into metallicity ranges $-0.8 \leq$ [Fe/H] < -0.2 (circles), $-0.2 \leq$ [Fe/H] < 0.1 (triangles), $0.1 \leq$ [Fe/H] < 0.5 (diamonds), or those which have no metallicity estimate quoted in Casagrande et al. (2011) (star symbols). We found no correlations between metallicity and FUV magnitude, as there are no obvious offsets between the three metallicity

groups in any of the four $(B-V)$ color ranges shown in Figure 2.5. However, this conclusion is limited by the small number of stars with [Fe/H] < -0.3 in our calibration sample.

The present work does not attempt to take interstellar reddening into account for the calibration sample. The sample of field stars is distributed across the sky and accurate reddening estimates, $E(B-V)$, would prove challenging to derive. The possibility that the FUV and optical colors of the calibration stars may be affected by interstellar reddening will therefore be a source of uncorrected scatter in the FUV-age calibration derived herein.

However, we did attempt to test for possible correlations between interstellar reddening and the FUV-excess parameter Q. The Gaia archive provides extinction values in the green band, A_G, for many stars within our calibration star catalog, although the uncertainties can be large, and one would not want the use of the A_G values to correct an observed Q value for interstellar reddening. Figure 2.9 shows the residuals of Q about our age-Q calibration fits versus this extinction. The residuals are the absolute difference in Q, estimated by FUV and $(B-V)$ colors from Equations 4.3 and 3.4, and a theoretical Q derived from the calibrated FUV-age relationship (Equations 2.4, 2.10 and 2.11). We do not observe any significant correlation, and so have not omitted any calibration stars on the basis of extinction values.

2.3.3 Associated Errors

Many literature-quoted ages from the field star catalogs utilized within this work are not accompanied with uncertainties. The scatter in the calibrations shown

in Figures 2.5 and 2.7 will be a consequence of several factors, including uncertainties in the literature-reported ages input into the calibration procedure and observational errors in the *FUV* magnitudes given in the *GALEX* GR6/7 data release[6]. We have attempted to quantify the extent to which errors in *FUV* magnitude measured for a star will propagate into uncertainties in ages which are determined through use of the above calibrations, and have demonstrated this in Figure 2.10. Equations 4.3, 3.4, 2.4, 2.10, and 2.11 were used to derive a Q value for a range of theoretical stellar ages (0.1-6 Gyr) given a hypothetical solar-like dwarf star with fixed $B - V = 0.65$. The resulting values of Q were then altered by adjusting the *FUV* magnitude by ± 0.02 and ± 0.05 to simulate an observational error in the *GALEX* flux. New stellar ages were derived for each adjusted value of Q. Figure 2.10 shows a plot of each new derived age versus the theoretical age, such that the departure of each curve from the exact 1:1 relation is a measure of how much error in τ can be expected just from photometric errors in *FUV* magnitude alone. We did not consider $Q > -1.0$ as this corresponds to a relatively flat portion of the *FUV*-age relationship curve and unreliable activity estimates. As such, the curves in Figure 2.10 are limited to $\tau = 6$ Gyr. As seen in this figure, as stellar age increases a given uncertainty in Q translates into a larger potential error in τ; a result which is a consequence of the intrinsic age-Q relation of dwarf stars. For example, for a solar-type G dwarf with age of around 6 Gyr an observational error of 0.05 mag in the Q index will translate into an error of ~ 1.0 Gyr in the derived age.

[6]A similar sample of late-F, G, and K type dwarf stars analyzed in Smith et al. (2017) have *FUV* uncertainties that were estimated to be ~ 0.12 mag.

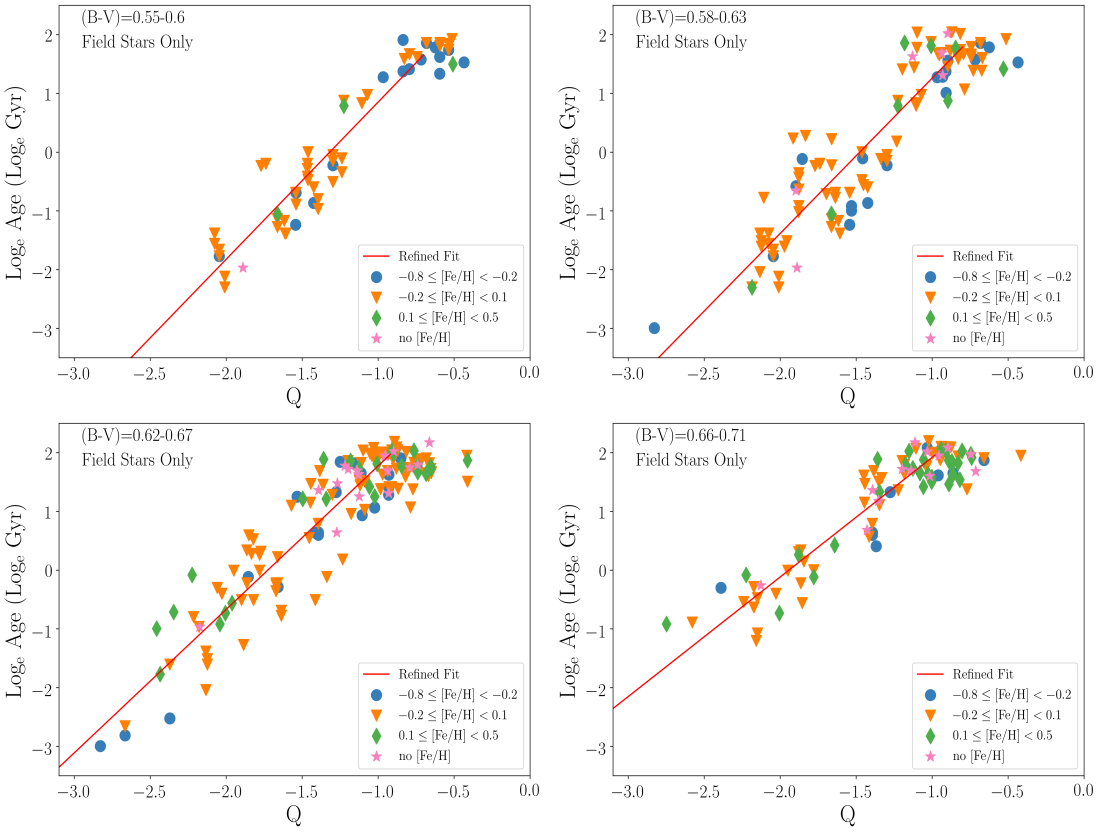

Figure 2.5 Four examples of the natural logarithm of literature-reported stellar age as a function of FUV-excess parameter Q for *field stars* only. The red line indicates the refined fit to combined stars from the four catalogs. Parameters of these fits can be found in the upper half of Table 2.2. Fits are restricted to stars with $Q \lesssim -1.0$, which depends on the flattening of the data in each $(B-V)$ range. Symbols denote stellar metal abundance according to the convention $-0.8 \leq$ [Fe/H] < -0.2 (circles), $-0.2 \leq$ [Fe/H] < 0.1 (triangles), $0.1 \leq$ [Fe/H] < 0.5 (diamonds), or no metallicity (stars) estimate quoted in Cassagrande 2011.

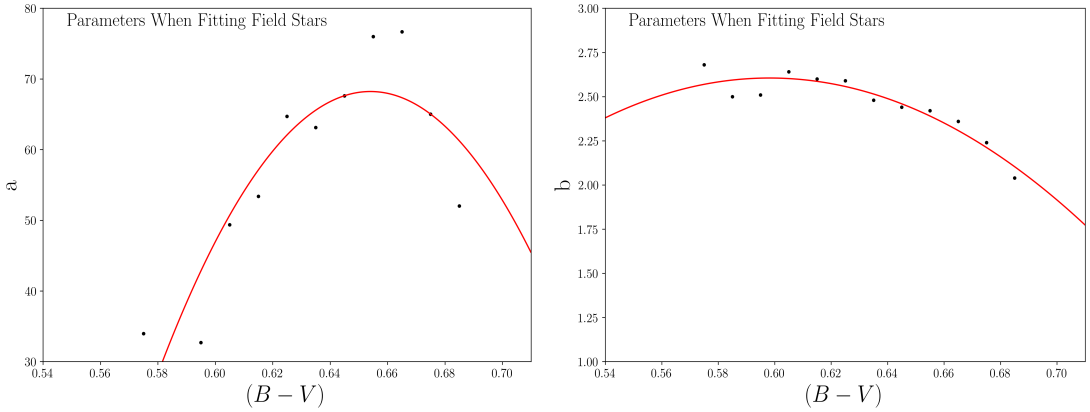

Figure 2.6 Parameters a and b from the upper half of Table 2.2 are fit with a quadratic function. These parameters are a result of fitting to field stars only. The plotted $(B-V)$ values are the median color within the 12 bins of Table 2.2.

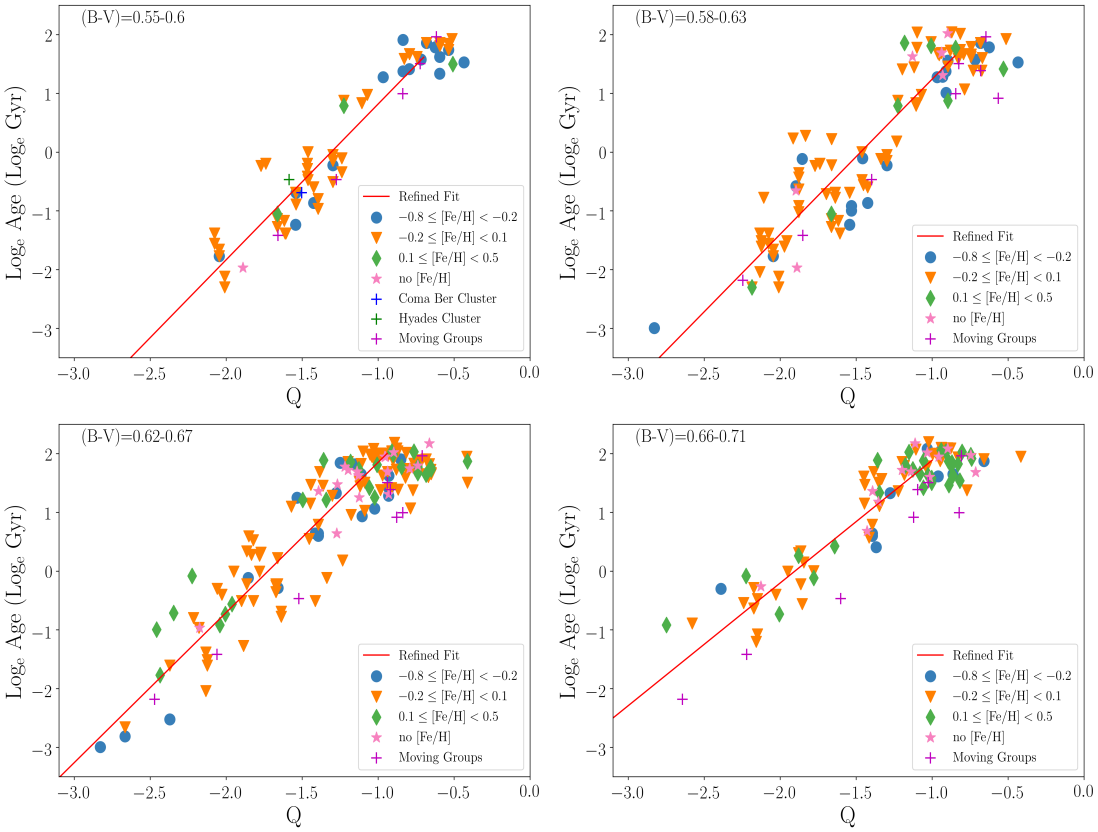

Figure 2.7 Age on a natural logarithmic scale versus FUV-excess parameter Q for field dwarfs, moving group stars, and open cluster stars within four example color ranges. The red line indicates the refined fits listed in the lower half of Table 2.2. Representative points for open cluster main sequences are only available for the upper left panels. Fits are restricted to stars with $Q \lesssim -1.0$.

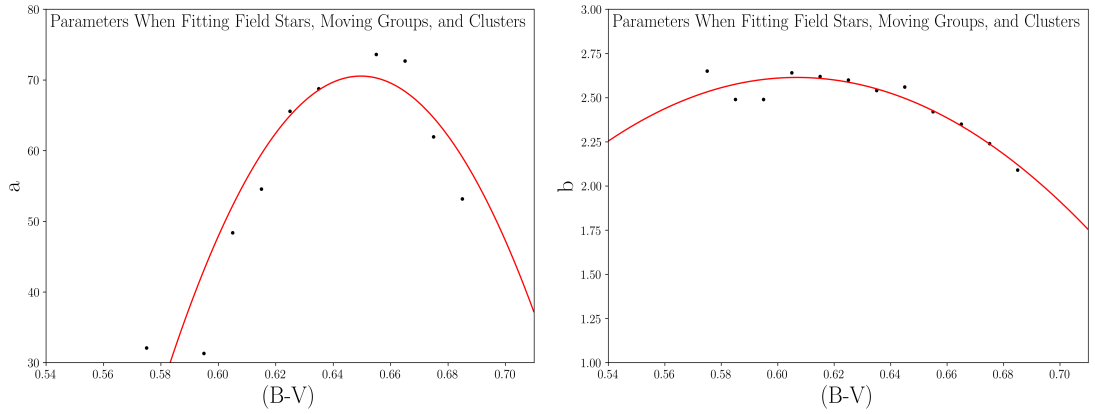

Figure 2.8 Parameters a and b from the lower half of Table 2.2 are fit with a quadratic function. These parameters are a result of fitting field stars, moving group, and open cluster main-sequence fiducial points. $(B-V)$ values are the median color within the 12 bins of Table 2.2.

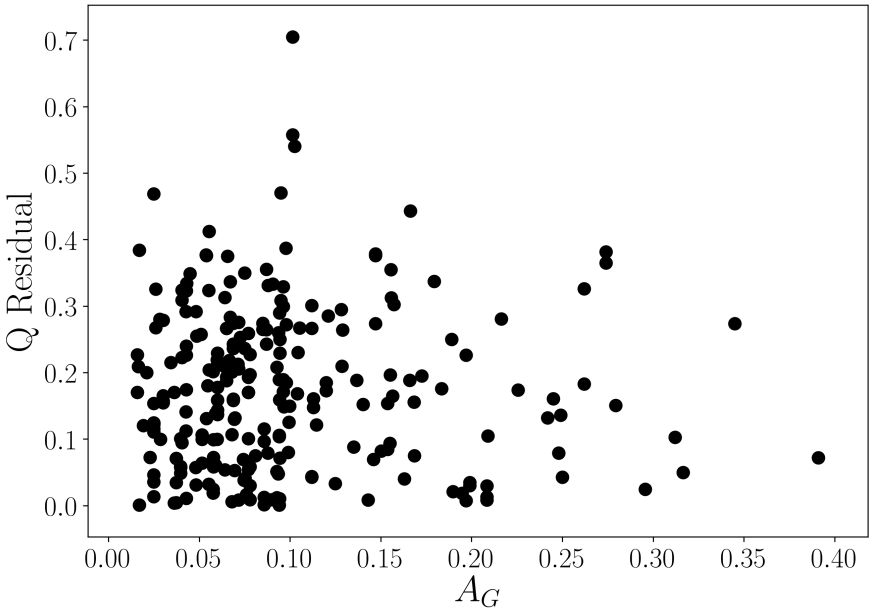

Figure 2.9 A test for possible correlations between interstellar reddening and the FUV-excess parameter, Q. Residuals are the absolute difference in Q, estimated by FUV and $(B-V)$ colors from Equations 4.3 and 3.4, and a theoretical Q derived from the calibrated FUV-age relationship (Equations 2.4, 2.10 and 2.11) Extinction values, A_G were collected from the Gaia DR2 catalog.

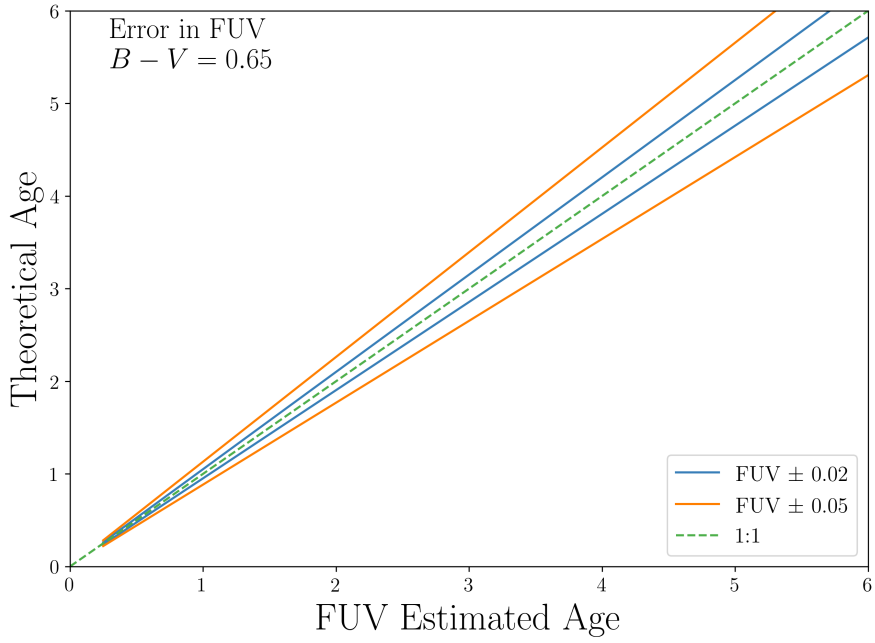

Figure 2.10 Errors in estimated ages for *FUV* magnitude measurement errors of ±0.02 (blue) and ±0.05 (orange). The green dashed line demonstrates a 1:1 exact match in age. For a given theoretical age the blue and orange curves show ages that would be estimated if the *FUV* magnitude was altered by an observational error of the indicated amount.

2.4 A Consistency Check: The Open Cluster NGC 752

Data for several open clusters with ages < 1 Gyr were used to derive the age-calibration of Section 2.3. Although open clusters can provide coeval samples of older G dwarfs, the equivalent *GALEX* photometry for such stars is scarce. Even the closest open clusters with ages greater than 1 Gyr are sufficiently distant that the G-dwarf region of the main-sequence is beyond the magnitude limit of the *GALEX* all-sky (AIS) images. Exposures of sufficiently long integration time to yield useful measurements of *FUV* magnitudes for G dwarfs in most open clusters would have required long pointed observations. Additionally, it was difficult to resolve crowded fields with *GALEX*, and Galactic midplane observations were avoided due to the brightness limits. This would have necessitated a *GALEX* Guest Investigator proposal, and there are very few that have acquired deep imaging for open clusters. One cluster for which deep *GALEX* imaging has been obtained is NGC 752 which has an age slightly greater than 1 Gyr. In this section we make use of the NGC 752 *GALEX* data to document the two-color diagram of the main sequence of this cluster and compare its observed $(FUV - B)$ color near the G-dwarf region with expectations from the FUV-age calibration of Section 2.3.

We find that given the FUV-age calibrations, $(FUV - B)$ colors inferred for theoretical stars with the appropriate age and $(B-V) = 0.6$ and $(B-V) = 0.65$ consistently fall within an extension of the observed main sequence of NGC 752. A collection of NGC 752 stars was identified in deep images from *GALEX* guest observer programs GI1_055001_NGC0752, GI5_063001_A262_FIELD2, and GI5_063001_A262_FIELD3. These

NGC 752 stars were selected from the WEBDA database (Netopil et al. 2012)[7], and only dwarfs with measured proper motions consistent with cluster membership were considered. A two-color diagram derived from *GALEX* FUV and Johnson B and V magnitudes (Daniel et al. 1994) for the set of observed cluster stars is shown in Figure 2.11 (black). Furthermore, two theoretical stars with a cluster age of 1.3 Gyr from Agüeros et al. (2018), derived with a Bayesian framework used to fit MESA isochrones, were adopted for representative colors of $(B-V) = 0.60$ and $(B-V) = 0.65$. Values of Q were determined for these two theoretical stars using Equations 2.4, 2.10, and 2.11, and these Q values were used in turn to determine values of $(FUV-B)$ from Equation 3.4. Reddening applicable to NGC 752 was added to the colors of the two theoretical points. We adopted the reddening $E(B-V) = 0.04$ from Taylor (2007). Sun et al. (2018) have published a comprehensive study of interstellar extinction in the *GALEX* photometric bandpasses and conclude that $E(FUV-B) = 3.4E(B-V)$. By comparison the absorption ratio of $R(FUV) = 6.8$ from Fitzpatrick (1999) leads to $E(FUV-B) = 2.7E(B-V)$. Consequently the reddening to NGC 752 in the FUV was taken as an average here to be $E(FUV-B) = 3.0E(B-V) = 0.12$.

These representative points derived from our FUV-age calibration and modified for interstellar reddening are shown in red in Figure 2.11. They fall on a plausible extension to the observed main sequence of NGC 752, so that our calibrations are consistent with NGC 752 cluster stars in the $(FUV-B)$ and $(B-V)$ two-color diagram. The *GALEX* photometry for NGC 752 shows increased scatter for dwarfs cooler than $(B-V) = 0.5$, presumably due to the faintness of these stars in the FUV band ex-

[7]The WEBDA astrometry are collected from ground-based observations.

posures. Thus we have not attempted to use the NGC 752 data as a direct input into the age calibration procedure of Section 2.3. Rather, the extrapolation of the data in Figure 2.11 has been used as a more limited consistency check on our calibration.

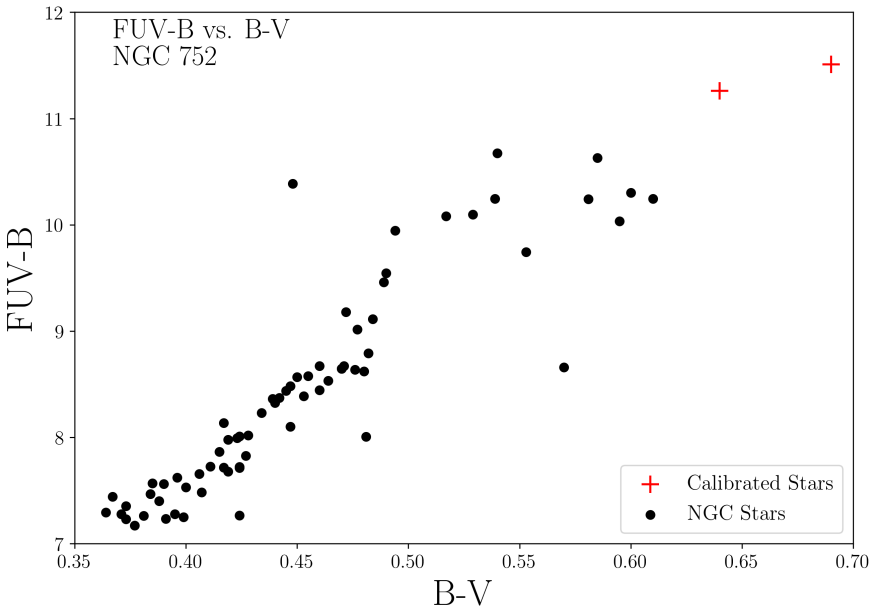

Figure 2.11 A two-color diagram demonstrates consistency between the FUV-age calibration from this work and main-sequence stars within the NGC 752 open cluster. The data points plotted for the cluster stars are the observed colors (i.e., they have not been corrected for interstellar reddening). Two theoretical points (red crosses) with intrinsic $(B-V) = 0.60$ and $(B-V) = 0.65$ plus FUV magnitudes derived from Equations 4.3, 3.4, 2.10 and 2.11 for an age of 1.3 Gyr have been plotted at a reddening applicable to NGC 752. These two fiducial points are consistent with an extension of the observed NGC 752 main sequence.

2.5 Activity Levels of Thin and Thick disk Stars

FGK dwarfs have a long history of being used to probe the chemical and kinematic history of the Galactic disk, and age is an important datum for such stellar populations studies. We have developed the FUV-age calibration of FGK dwarfs with

the goal of applying said calibration to stellar population studies within the Milky Way. In this section we illustrate one use of the Q parameter for probing the question of activity and age distributions among the thin and thick disk populations of stars in the solar neighborhood. Thin and thick disk stars are often determined to be such using kinematics, chemical abundances, or a combination of the two. In this section we utilize a collection of dwarf stars which are classified as either thin or thick disk stars as determined by their chemical abundances. We have used *GALEX FUV* measurements of these stars to determine their activity levels, Q, and FUV-derived ages.

Delgado Mena et al. (2017) determined chemical abundances of more than 1000 F, G and K-type dwarf stars with HARPS-GTO spectra. They have defined thick and thin disk stars by [α/Fe] where α is an average of Mg, Si, and Ti abundances (see Adibekyan et al. 2011). In Adibekyan et al. (2011) stars with $T_{\rm eff} = T_{\odot} \pm 300$ K were binned into five [Fe/H] ranges. The α abundance was clearly characterized by low-α and high-α populations within each bin. The thin and thick disk populations were then defined by the separation line between each low-α and high-α group. We have cross-matched stars in the Delgado Mena et al. (2017) catalog with the *GALEX* catalog. We then narrowed down the sample to stars with colors $0.575 \leq (B-V) \leq 0.685$ (corresponding to the minimum and maximum representative $(B-V)$ colors in Table 2.2) thereby obtaining a total of 175 stars listed in Table B.2 within Section B.2 of Appendix B. Of these stars, 21 are categorized as thick disk constituents and 154 are thin disk stars. Table B.2 lists the identifier of each star, the $(B-V)$ color, the *GALEX FUV* magnitude, the FUV-excess index Q, plus the [α/Fe] abundance as given by Delgado

Mena et al. (2017). Figure 2.12 shows a two-color diagram of theoretical isochrones. Given a theoretical age, Equations 4.3, 3.4, 2.4, 2.10, and 2.11 were used to determine $(FUV - B)$ for the isochrones. The "isochrones" are smooth which demonstrates that reasonable fits have been obtained across the $(B - V)$ bins chosen in our calibration. The Delgado Mena et al. (2017) sample of stars from Table B.2 is also plotted in Figure 2.12. We note that many stars from Delgado Mena et al. (2017) exist with ages greater than the upper limit to our age calibration. This is the nature of star formation within the Milky Way. According to a review of the cosmic star formation rate by Madau & Dickinson (2014) only $\sim 25\%$ of stars in a galaxy such as the Milky Way formed after $z = 0.7$ (a look-back time of 6.5 Gyr). We determined Q values for these stars using Equations 4.3 and 3.4. The left panel of Figure 2.13 shows the distributions of Q.

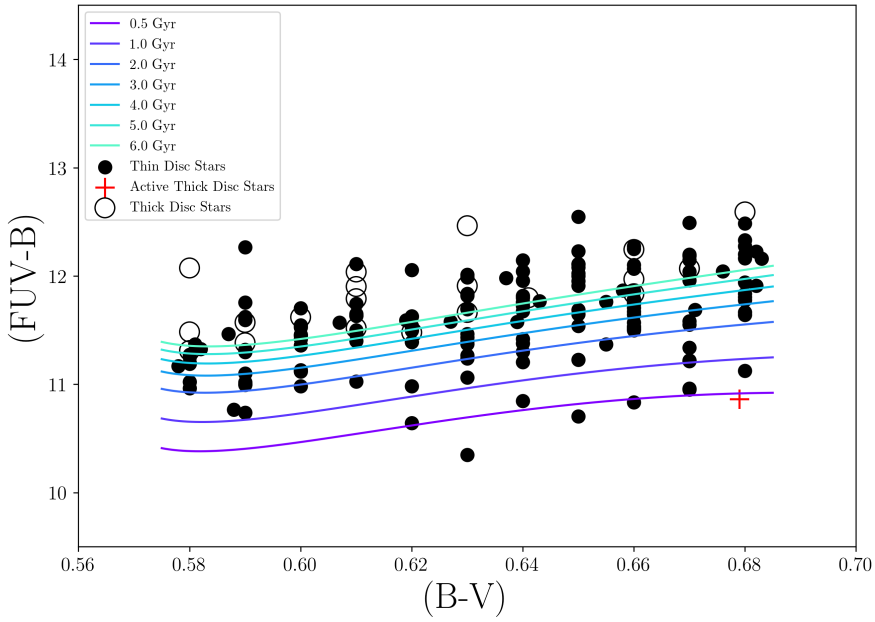

Figure 2.12 A two-color diagram of $(FUV - B)$ versus $(B - V)$. Each line represents an isochrone. Equations 4.3, 3.4, 2.4, 2.10, and 2.11 were used to determine $(FUV - B)$ for the isochrones. The data points show the stars from Delgado Mena et al. (2017) that are listed in Table B.2.

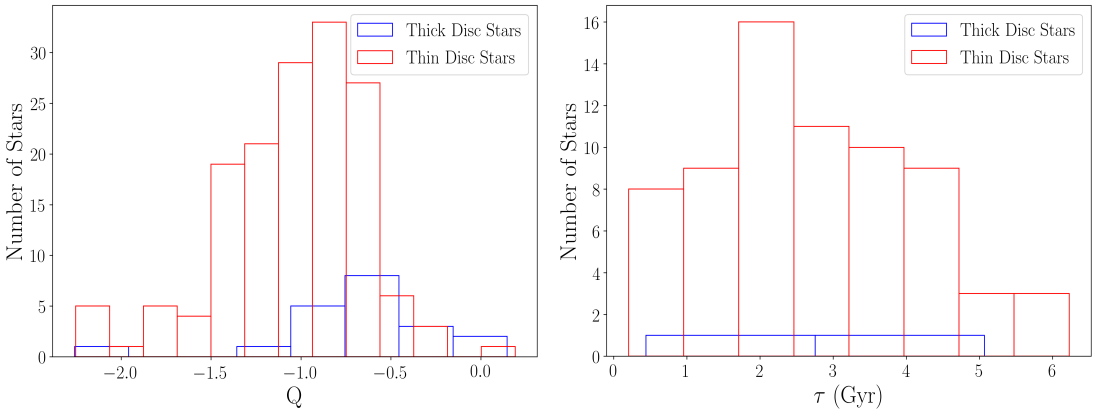

Figure 2.13 Left panel: the distribution of Q for the 175 dwarf stars from Table B.2. Right panel: the distribution of τ for 69 thin and two thick disk stars; designated as such using chemical abundances (Delgado Mena et al. 2017). The right panel does not include any stars with $Q > -1.0$

Kolmogorov-Smirnov (KS) tests were performed on the Q distributions. Both thin and thick disk Q distributions were compared to Gaussian and Cauchy distributions, as Cauchy distributions have extended tails. Tests gave small p-values and we concluded that neither distribution were Gaussian or Cauchy. A two-sample KS test in which the thin and thick disk distributions were compared revealed that they were not of the same parent distribution. The kurtosis for each distribution was determined to be 4.10 and 0.94 for the thick and thin disk populations respectively. Since both distributions have a positive kurtosis, they have heavier tails than a Gaussian distribution. The thick disk distribution has significantly less stars than those in the thin disk distribution. As such, the kurtosis comparison must be taken with caution. If we do not consider the thick disk star with $Q < -2.0$ our distribution changes and the kurtosis for this population becomes 0.24. Future work with a larger population of thick disk stars, categorized by their metallicities only, and which have *GALEX FUV* magnitudes will benefit a further exploration of this distribution.

Table 2.3 Q and τ of Thin and Thick Disk Distributions

Population	Mean	SD[a]	SEM[b]
	Q[c]		
Thick	-0.70	0.46	0.10
Thin	-1.03	0.40	0.03
	Age (Gyr)[d]		
Thick	2.8	2.3	0.3
Thin	2.8	1.5	1.1

[a] Standard deviation
[b] Standard error of the mean
[c] Q for all stars from Table B.2.
[d] Age for stars with $Q \leq -1.0$

Our FUV-age calibration cannot resolve stars with $Q \gtrsim -1.0$, which are the oldest stars in the thin and thick disk populations. We used Equations 2.4, 2.10, and 2.11 to estimate τ for the stars which have $Q \leq -1.0$. This corresponds to 69 thin disk and two thick disk stars. The left panel of Figure 2.13 shows the distribution of Q values for all 175 stars from Table B.2. By contrast, the right panel of Figure 2.13 show the distribution of τ (gigayears) values derived for the 71 stars from Table B.2 that have $Q < -1.0$.

The mean and standard deviations for the Q and τ distributions are given in Table 2.3. Once again, the statistics for Q are derived from the full sample of 175 stars from Table B.2, whereas only those stars with $Q \leq -1.0$ are included in the age data due to the restrictions on our age calibration that are diskussed in Section 2.3. The mean age of both thick and thin disk stars with $Q \leq -1.0$ is 2.8 Gyr, although with only two thick disk stars the comparison is not very meaningful. Furthermore, the limits on our

age calibration mean that we cannot probe differences in the age distributions of thick and thin disk stars much older than ~ 7 Gyr. We note that we are therefore significantly biased in this sample of stars with Q-derived ages as, due to the age limitation of our calibration, we are only considering the youngest stars in the thick disk population. Thus our most useful conclusions come from comparing the distributions of Q values.

In Figure 2.14 we plot [Fe/H] and [α/Fe], as determined by Delgado Mena et al. (2017), against Q for all stars from Table B.2. Although there is a clear separation of [α/Fe] metallicity between the two populations of stars, their Q values overlap in the low-activity regime. The mean values of Q for the thick and thin disk stars in the full sample of Table B.2 differ by 0.33, and this difference is comparable to three times the quadrature sum of the standard errors in the mean (Table 2.3). Thus, the mean Q values of the thick and thin disk samples do appear to be significantly different, consistent with the KS test returning a difference between the two Q distributions. The average value of Q for the thick disk sample is greater than for the thin disk sample, implying that the thick disk stars in Table B.2 are on average older than the thin disk (when uncalibrated stars older than 6-7 Gyr are included in the comparison).

First identified by Gilmore & Reid (1983), two distinct populations of stars within the Galaxy, the thin and thick disks, have been regularly investigated. Much time has been spent exploring the definitions of these populations and their formation histories.[8] There are two broad possibilities of thick disk formation: the disk formed in situ or it is a "puffed up" version of the thin disk.

[8]Investigations also include the possible nonexistence of the two populations. For example, Bovy et al. (2012) find no distinct populations, and that the thick disk is a tail of a continuous scale-height distribution.

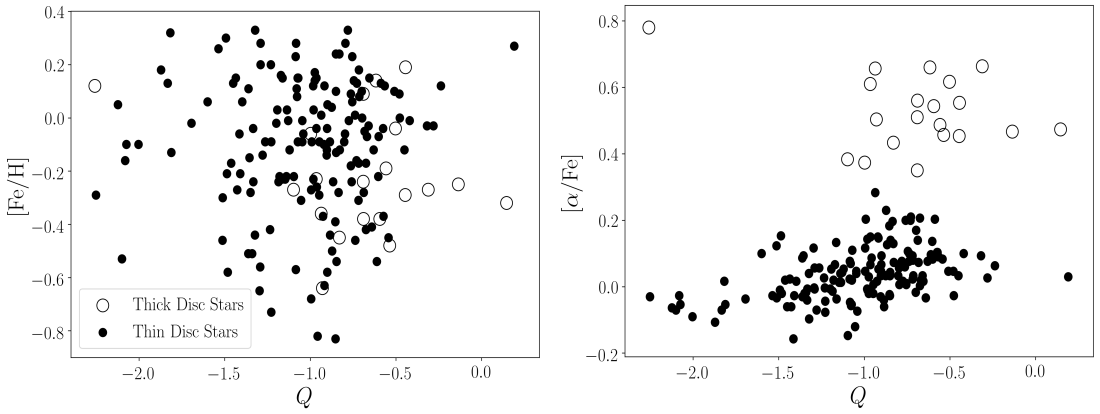

Figure 2.14 Metallicity versus FUV-excess parameter, Q, for all thin and thick disk stars from Table B.2.

In the former scenario early star formation produced metal poor stars which maintained their scale heights after the surrounding gas collapsed into the Galactic plane (Veltz et al. 2008; Robin et al. 2014; Navarro et al. 2018). These stars are identified as intermediate Population II, thick-disk stars. Younger Population I, thin-disk, stars formed later in the collapsed disk. A similar scenario describes a major merger (Veltz et al. 2008), or several mergers (Brook et al. 2004) early on in the Milky Way's formation history in which accretion formed the thick disk stars in situ. In this case the merger(s) must have occurred before the gas which formed the thin disk fully settled to avoid major disruption to the thin disk.

Alternatively, thick disk stars may have larger scale heights than thin disk stars due to dynamical heating. Early on in the Milky Way's formation a rapidly spinning gas cloud collapsed and settled (as described, for example, in Eggen et al. 1962). The thick disk stars then formed and their orbits have been heated or "puffed" up to greater distances above the Galactic mid-plane. Thin disk stars were formed later and have not experienced the same amount of scatter. Several mechanisms may have

contributed to the observed heating (Hänninen & Flynn 2002; Aumer et al. 2016) which likely include scatter from Giant Molecular Clouds and/or black holes (Lacey & Ostriker 1985; Hänninen & Flynn 2002). Heating may have been a consequence of the Milky Way's spiral structure or a possible bar (Barbanis & Woltjer 1967; Aumer et al. 2016). Additionally, minor mergers from satellite galaxies may have played a role (Walker et al. 1996; Moetazedian & Just 2016; Ting & Rix 2019).

Regardless of the precise forms of the Q and age distributions among the thin and thick disk stellar populations of the Milky Way, what Figure 2.14 does reveal is that a range in both [Fe/H] and [α/Fe] exists among Population I dwarfs of the same activity levels and thus ages. In other words, the chemical evolution of the Galactic disk has been spatially heterogeneous with regions of different [Fe/H] and [α/Fe] giving rise to star formation at the same time. Although the number of high-[α/Fe] stars in the right panel is admittedly small, the results do suggest that such stars have formed within the Milky Way up until at least 4 Gyr ago.

Based on the sample of stars from Delgado Mena et al. (2017) that have *GALEX FUV* measurements, age alone does not seem to be a sufficient datum for distinguishing between a thick and a thin disk star. Figure 2.13 indicates that high-[α/Fe] stars were being formed in the Milky Way up until 4 Gyr ago. The question remains: where were these high-[α] stars formed? If both solar-[α/Fe] and high-[α/Fe] stars were forming within a thin disk configuration, why would scattering processes that heat drive stars into a thick disk configuration only affect the high-[α/Fe] stars? Arguably many of the high-[α] stars either formed within a thick disk configuration at the

same time that solar-[α/Fe] stars were forming in a thin disk (an in situ picture), or the sites of high-[α/Fe] star formation were located such that subsequent heating processes would subsequently drive them into a thick disk configuration (a combined in situ plus scattering scenario). The formation of high-[α/Fe] stars within dwarf galaxies that were subsequently accreted onto the Milky Way and then scattered into a thick disk would be in accord with this second alternative. The implication of Figures 2.13 and 2.14 for such a combined scenario would be that dwarf galaxies were still being acquired some 4 Gyr ago, and such galaxies had interstellar gas of high-[α/Fe] abundance that was forming stars possibly just prior to, or because of, the accretion event.

There are some limitations to our conclusions. The FUV-dating estimates lack the resolution at old ages to be able to determine whether is a population of very old thick disk stars that formed before the Galactiuc gas collapsed into a thin disk morphology. Given that stars older than the Sun are expected to have low levels of activity, it would be among the oldest thick and thin disk stars that the current technique most lacking in leverage. By contrast, we are better placed to determine when the most recent thick disk dwarf stars formed given a large enough sample of such stars. In this context, it is noted that there is one quite active star in the present thick disk sample, which is depicted as a red cross in Figure 2.12. This is HD 16784 with an iron abundance of [Fe/H] $= -0.65$. It would seem worthwhile to further investigate the level of chromospheric activity of this star by using other activity indicators such as the Ca II H and K emission lines.

It has been the intent of this section to illustrate the potential that the Q

parameter may have for stellar population studies when used with larger numbers of thick disk stars in particular. Theoretical work on understanding the behavior of the *FUV* spectra of dwarf stars as a function of metal abundance would also be welcome. Many of the strongest emission lines in the *FUV* region of the spectrum arise from elements such as C, O, and Si, which are α elements. Thus in comparing two stars of the same [Fe/H] there arises the consideration of how the most prominent emission lines in the *FUV* may be affected by varying the [α/Fe] abundance ratio. Enhancing the α element might serve to strengthen *FUV* emission lines via direct abundance increases increases, however, elements such as C, O and Si can be important coolants of a chromosphere such that the temperature structure may be altered. Model chromosphere combined with synthetic spectrum calculations are needed to address the importance of such effects.

2.6 Potential Applications of *FUV*-Determined Ages

Purely empirical age calibrations for late-type dwarf stars have been demonstrated by utilizing only Johnson B, V and *GALEX FUV* magnitudes. The *FUV*-excess parameter, Q, shows promise as an age indicator for late-F, G, K type dwarf stars (provided that interstellar reddening is not a complication). Many previous works have demonstrated the use of coronal and chromospheric emission observations as stellar activity and hence age indicators of dwarf stars. This chapter has formulated a calibration which with *GALEX FUV* photometry can be added to the toolbox of stellar activity age-dating techniques, including those based on the Ca II H and K emission

lines or soft X-ray flux.[9]

Such a calibration has practicality in opening up the vast amount of *GALEX* near-all-sky *FUV* photometry for use in stellar age dating. Considerable overlap is expected to exist between the *GALEX FUV* survey and various large astrometric surveys, such as Gaia, and stellar abundance surveys such as the Geneva-Copenhagen and RAVE surveys. It follows that *FUV*-age dating could be incorporated into population studies of FGK dwarfs within the Galaxy. For example, the method of estimating dwarf star ages derived in this work may be used to further study the age-metallicity and age-velocity relations of dwarf stars within local regions of the Milky Way. Traditionally tests of the age-metallicity relation have utilized isochrone-derived ages, but these ages can widely vary given differing input parameters and modeling techniques (see e.g., Pont & Eyer 2004; Casagrande et al. 2011). The age-*FUV* relationship for late-F and G dwarfs could be used in conjunction with stellar catalogs such as the Geneva-Copenhagen Survey (Nordström et al. 2004a,b), which contains large numbers of such stars in the solar vicinity.

[9] In Section A.3 of Appendix A we explore a comparison between gyrochonology and *FUV*-determined ages. Both of these techniques rely on the spin-down phenomenon.

Chapter 3

Correlations in Chromospheric and Coronal Activity Indicators of Giant Stars

3.1 Introduction

Stars of FGK spectral type undergo mass loss during the main sequence stage of evolution via a coronal hot wind and rotational spin down. This mass loss, in turn, is associated with a decrease in surface magnetic field strength. Activity levels in the chromosphere, transition region, and corona are tied to the magnetic field strength and thus also decrease with age during the main sequence phase (Skumanich 1972). Such correlations suggest that FGK stars should be relatively inactive once they commence evolving to the red giant branch in the Hertzsprung-Russell diagram. Indeed, an ob-

serving program by Linsky & Haisch (1979) early in the *IUE* satellite mission showed an absence of coronal emission among a small sample of highly evolved late-type giants; although such stars were known to possess chromospheres through earlier studies such as Wilson (1967, 1976); Deutsch (1970); Bappu & Sivaraman (1977); Stencel (1978).

In years since, there has been active research into the surface activity levels of giant stars. Surveys have been made of soft X-ray coronal emission among giants in different regions of the H-R diagram (see e.g., Maggio et al. 1990; Haisch et al. 1991; Hünsch et al. 1996; Ayres et al. 1998; Gondoin 1999). Clarifying the absence of coronal emission among the coolest giants, Ayres et al. (1997) suggested that coronal loops are partially embedded in the chromosphere. This implies that coronae remain active into the subgiant and giant phases (see also Hünsch & Schröder 1996; Ayres et al. 2007). Observations with the *IUE* and *FUSE* satellites have enabled studies of far-ultraviolet emission lines arising in a transition region. Examples of such studies from samples of red giants, in varying stages of evolution, include Linsky & Haisch (1979); Ayres et al. (1981); Simon (1984); Hartmann et al. (1985); Simon & Drake (1989); Dupree et al. (2005). Additionally, Ayres et al. (1982) demonstrated that observed broad C IV profiles are typical of active giant stars. Chromospheric activity in giants is less elusive to optical observation, and thus has a long history of study going back to the discovery of the Wilson-Bappu effect (Wilson & Vainu Bappu 1957). Ground-based and *IUE* studies by Rutten & Pylyser (1988); Pasquini et al. (1990); Dupree et al. (1999); Pérez Martínez et al. (2011); Smith & Shetrone (2000), for example, have aided in further mapping out chromospheric activity in giants through observation of the Mg II h and k

and Ca II H and K emission lines.

Among red giants there is interest in activity levels in core Helium-burning (CHeB) stars, also known as red clump giants (see e.g., Baliunas et al. 1983). There are clues to be gleaned from understanding the surface activity levels of such stars. For example, one may interpret the evolution of internal angular momentum and magnetic breaking within these stars as they prepare to make a second ascent of the red giant branch. Core helium burning occurs with a violent flash for stars less than $\sim 2\ M_{\odot}$, or more gradually for higher mass stars. Works such as Maeder & Meynet (2014) explore how the core of CHeB stars may spin down and impact surface activity levels. The notable recent work of Schröder et al. (2020) show the first direct evidence of magnetic breaking during the Helium core burning phase. Through TIGRE high-resolution spectra they found that two Hyades, K-type, Helium-core burning giants are entering their blue loop. These two stars have more active chromospheres and coronae than two other observed Hyades giants which have already evolved onto the blue loop. This magnetic breaking is a similar phenomena to that which occurs in cool main sequence stars. Hence, it is of particular interest to investigate the activity levels of giant stars which are burning helium in their cores.

High-resolution spectroscopy is often used to trace activity levels in the chromosphere and transition region. For example, Ca II emission, which originates in the chromosphere, has been a prime tool among both giant and main sequence stars since the H and K Fraunhofer lines are dark in the photosphere. Upon proceeding to shorter wavelengths in the mid to far ultraviolet for FGK stars, photospheric flux is also re-

duced. The reduction allows chromospheric emission lines to be illuminated with greater contrast. Far-ultraviolet (FUV) brightness, as measured by the $GALEX$ satellite, has been found to trace Ca II H and K emission lines, and hence chromospheric activity among dwarf stars (Smith & Redenbaugh 2010; Findeisen et al. 2011; Crandall et al. 2020). Similarly soft X-ray emission Smith et al. (2017) is a tracer of coronal activity (see e.g. Pizzolato et al. 2003; Jackson et al. 2012; Booth et al. 2017). Such results for main sequence stars motivate an analogous study focusing on a $GALEX$-based FUV color of giant stars. In a previous paper, Smith (2018) documented correlations between an ($FUV - B$) color and the strength of the λ2800 Mg II h and k emission lines. The present work seeks to extend a comparison of FUV-based colors against other measures of red giant activity.

This work analyzes four indicators of atmospheric activity of giant stars of late spectral type: Mg II h and k emission lines, X-ray emission, far-ultraviolet emission, and $v\sin i$ rotation estimates. In Section 3.2 we lay out the sample of giant stars and their properties for which we have compiled data on the FUV, X-ray, and Mg II activity indicators. Section 3.3 demonstrates a clear relationship between X-ray luminosity as a coronal activity indicator and Mg II emission as a chromospheric activity indicator. Section 3.4 examines the activity levels of CHeB stars as seen in the far-ultraviolet and X-ray using $GALEX$ and $ROSAT$ space telescope observations. Within this section we investigate the differences in X-ray and FUV observations as tracers of giant star surface activity. To complete the work, we attempt to constrain the activity-rotation relationship of giants using FUV and $v\sin i$ data; a relationship which proves to be

elusive despite clear activity indication variances in our sample. A conclusion is given in Section 3.6.

3.2 Red Giant Sample

The basis of our stellar sample was compiled from the Hünsch et al. (1998) catalog of 450 giants and supergiants detected in the *ROSAT* all-sky survey (RASS). Hünsch et al. (1998) first selected 3,839 stars of spectral type A, F, G, K, M, and C, and luminosity classes I, II, III or intermediate classes within the Bright Star Catalogue (BSC) (Hoffleit & Warren 1991). Positions of these BSC giants and supergiants were then cross-matched with the RASS to detect locations with X-ray emission. The result was 450 giants and supergiants with *ROSAT* X-ray observations. Individual X-ray luminosities were not calculated in the Hünsch et al. (1998) compilation due to a lack of precise parallaxes. Instead, the X-ray to bolometric flux ratio is quoted. This ratio is used within our work to investigate coronal emission strength. This sample of giants and supergiants was further narrowed down for the needs of each proceeding section.

3.3 Mg II λ2800 Emission and X-ray Activity Indicators of Giants

A commonly-used indicator of stellar activity among red giant stars is the pair of λ2800 Mg II chromospheric emission lines. Pérez Martínez et al. (2011) studied a sample of red giants for which high-resolution spectra of these lines are available in the archives of the International Ultraviolet Explorer (*IUE*). They derived the flux

arriving at Earth in the combined Mg II h and k emission lines from the flux-calibrated *IUE* archive spectra. This observed flux was converted to a flux at the stellar surface. Their approach yielded two values of this stellar surface flux, since they calculated two values of stellar effective temperature $T_{\rm eff}$, one based on the observed $(V-K)$ color and a second based on the $(B-V)$ color. They also applied appropriate bolometric corrections to the V and K magnitudes in order to get two values for the bolometric luminosity. In this chapter we adopt a mean of the two surface flux determinations made by Pérez Martínez et al. (2011) and denote this as $F_{\rm MgII}$. Furthermore, we have calculated the ratio of the Mg II h and k surface flux to the bolometric surface flux for each star, according to

$$\log(F_{\rm MgII}/F_{\rm bol}) = \log F_{\rm MgII} - \log(\sigma T_{\rm eff}^4), \tag{3.1}$$

using the mean of the two effective temperature values from Pérez Martínez et al. (2011). Equation 3.1 can be rewritten in a form that is more practical for present purposes, namely

$$\log(F_{\rm MgII}/F_{\rm bol}) = \log f_{\rm MgII} - 4\log T_{\rm eff} + 4.25, \tag{3.2}$$

where $f_{\rm MgII}$ denotes the value of the Mg II h and k stellar surface flux as given by Pérez Martínez et al. (2011) in units of mW m^{-2}. Equation 3.2 was used to calculate a normalized flux ratio $(F_{\rm MgII}/F_{\rm bol})$ for those red giants considered in this section.

Cross-checking the *ROSAT* compilation of red giant detections from Hünsch

et al. (1998) (see Section 3.2) with the sample covered by Pérez Martínez et al. (2011) gives the stars listed in Table 3.1 wherein the HD number and the designation by constellation are listed. Both the $\log(L_X/L_{bol})$ and $\log(F_{MgII}/F_{bol})$ stellar activities are listed together with $(B-V)$ color and the absolute visual magnitude. The values of $(B-V)$ color in Table 3.1 are those given by Pérez Martínez et al. (2011), while absolute visual magnitudes M_V were calculated by combining V magnitudes from Mermilliod et al. (1997) with stellar parallaxes obtained from the SIMBAD data base (Wenger et al. 2000). Most of the parallaxes given by SIMBAD for the stars in Table 3.1 come in turn from the *Gaia* Data Release 2 (Gaia Collaboration et al. 2018a), although some are from the *Tycho-Gaia* Astrometric Solution (Gaia Collaboration et al. 2016) or *Hipparcos* (van Leeuwen 2007). Binarity is often addressed as a concern when interpreting the activity levels of FGK giants in particular. Information on the binary status of each star is codified in Table 3.1 according to the following convention: S indicates stars not noted from a SIMBAD query to be a binary, D corresponds to a star that is listed in one or more double star catalogs but which is not designated as a spectroscopic binary in SIMBAD, SB indicates those stars that are listed as spectroscopic binaries in SIMBAD, while chromospherically active RS CVn stars are separately identified. The list in Table 3.1 also contains one long period variable (LPV), a flare star (HD 133208), a BY Dra variable (HD 203387), the rotationally variable (Ro) star HD 111812, and one Cepheid (HD 102350) which itself is a member of a binary system. Nearly all stars listed in Table 3.1 are members of a binary system. We are presuming that this reflects a penchant for proposers of *IUE* time to favor active giants as opposed to chromospherically quiet

evolved stars.

The soft X-ray luminosity normalized to the bolometric luminosity is plotted in Figure 3.1, versus an analogous flux ratio for the Mg II h and k emission lines. Symbols in the figure depict the binarity status. A correlation is evident, albeit with some scatter. The most X-ray luminous giants are the RS CVn stars which also exhibit strong Mg II h and k emission. Most of the other giants in the sample with $\log(L_{\rm X}/L_{\rm bol}) > -6.0$ are binaries or other exotica, although there are two giants in this X-ray regime that are not known binaries and which evince slightly enhanced Mg II h and k emission. Many of the stars in Figure 3.1 are relatively quiet with $\log(L_{\rm X}/L_{\rm bol}) < -6.0$ and $\log(F_{\rm MgII}/F_{\rm bol}) < -4.8$. Among the giants in this "quiet" category, there is no correlation between the two activity indicators, although there is a range in normalized X-ray flux of more than a factor of ten. Giants with intermediate levels of λ2800 Mg II emission, such that $-4.8 < \log(F_{\rm MgII}/F_{\rm bol}) < -4.5$, are rather interesting since they have very little difference in Mg emission but almost a factor of 100 spread in normalized X-ray flux.[10] Thus it seems that (i) relatively high-activity stars contribute much of the correlation seen in Figure 3.1, and (ii) there can be a large range in $\log(L_{\rm X}/L_{\rm bol})$ among giants with comparable Mg II h and k emission and $(B-V)$ color.

[10] An interesting comparison pair here is HD 4128 and HD 84441 neither of which are indicated by SIMBAD to be binaries, yet HD 4128 has a greater $\log(L_{\rm X}/L_{\rm bol})$ by a factor of 30. Of these two HD 84441 (HIP 47908) has a spectral classification as listed by SIMBAD of G1III although others sources suggest G0II. Massarotti et al. (2008) measured a project rotation speed of $v\sin i = 8.0$ km s^{-1} which is quite high for a isolated giant star. By contrast, HD 4128 (HIP 3419) is a high proper-motion star of spectral type G9.5III that has been the subject of a number of X-ray (*Einstein*, *ROSAT*, and *ASCA*) detections, yet Massarotti et al. (2008) measured a lower $v\sin i$ (= 6.8 km s^{-1}) than for HD 84441.

Table 3.1 Cross-matched Sample with *ROSAT* Observations and Mg II h and k Measurements

HD	$\log(L_X/L_{bol})$	$\log(F_{MgII}/F_{bol})$	$(B-V)$	M_V	Binarity[a]	Name
1522	-6.94	-5.2	1.19	-1.08	D	ι Cet
3627	-7.03	-5.3	1.26	0.71	SB	δ And
4128	-5.39	-4.7	1.01	-0.32	n	β Cet
4502	-4.81	-4.0	1.08	0.24	RS CVn	ζ And
9746	-4.40	-3.6	1.20	-0.06	RS CVn	OP And
13480	-4.58	-4.2	0.74	0.20	SB, CABS	ι Tri
17506	-6.70	-5.2	1.56	-3.39	D	η Per
19476	-6.88	-5.1	0.97	1.11	D	κ Per
27371	-5.59	-4.1	0.97	0.17	D	γ Tau
27697	-6.87	-5.0	0.97	0.36	SB	δ Tau
28305	-7.01	-5.1	1.00	0.27	D	ϵ Tau
28307	-5.22	-4.7	0.94	0.46	SB	θ^{01} Tau
40409	-6.79	-5.2	1.01	2.55	n	36 Dor
42995	-7.20	-5.1	1.57	-2.08	SB	η Gem
62044	-4.08	-3.8	1.11	1.44	RS CVn	σ Gem
62345	-6.54	-5.1	0.92	0.39	D	κ Gem
62509	-7.73	-5.1	0.99	1.07	D	β Gem
71369	-6.44	-5.1	0.84	-0.33	D	UMa
82210	-4.46	-4.2	0.77	2.05	RS CVn	24 UMa
84441	-7.00	-4.7	0.78	-1.42	n	ϵ Leo
93497	-5.16	-4.5	0.89	-0.09	D	μ Vel
93813	-7.00	-5.2	1.22	-0.11	n	ν Hya
102350	-6.58	-4.9	0.85	-1.29	D, Cepheid	.
106677	-3.96	-3.9	1.10	0.45	RS CVn	DK Dra
108907	-6.53	-5.2	1.56	-1.44	SB	4 Dra
109379	-7.44	-5.1	0.88	-0.60	n	β Crv
111812	-4.48	-4.4	0.65	0.19	Ro	31 Com
113226	-6.47	-5.0	0.92	0.20	D	ϵ Vir
115659	-6.02	-5.1	0.91	-0.07	SB	γ Hya
133208	-6.76	-5.2	0.93	-0.68	Flare	β Boo
141714	-4.91	-4.3	0.78	1.04	RS CVn	δ CrB
147675	-5.27	-4.6	0.91	0.48	n	γ Aps
148387	-7.62	-5.1	0.90	0.47	n	η Dra
148856	-6.50	-5.1	0.93	-0.37	SB	β Her
150798	-6.92	-5.0	1.41	-3.48	D	α TrA
150997	-6.58	-4.7	0.90	0.88	D	η Her
153751	-4.86	-4.4	0.86	-0.62	RS CVn	ϵ UMi
159181	-5.90	-4.4	0.92	-2.53	D	β Dra
163993	-4.95	-4.7	0.92	0.58	LPV	Her
203387	-4.94	-4.5	0.87	0.38	BY Dra	ι Cap
205435	-5.18	-4.5	0.87	1.11	n	ρ Cyg
211416	-7.08	-4.6	1.37	-1.08	SB	α Tuc
216489	-4.02	-3.0	1.10	0.98	RS CVn	IM Peg
218356	-5.23	-3.4	1.23	-1.55	SB	56 Peg

[a] n: not listed as a binary star in SIMBAD, CABS: chromospherically active binary, D: in one or more double star catalogs but not listed as spectroscopic binary in SIMBAD, LPV: long period variable, Ro: rotationally variable, FK Com type variable, SB: listed as spectroscopic binary in SIMBAD

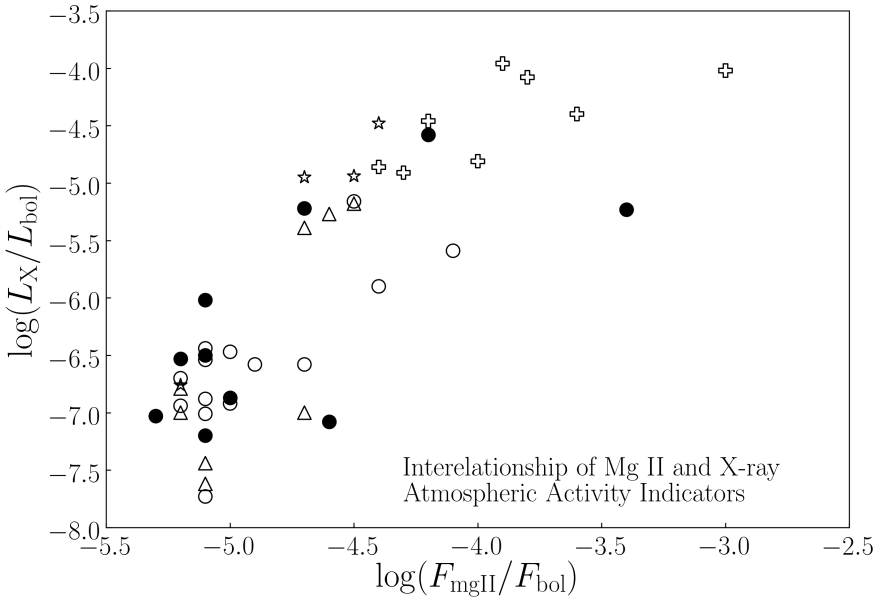

Figure 3.1 $\log(L_X/L_{bol}) > -6.0$ versus $\log(F_{MgII}/F_{bol})$ for giant stars in Table 3.1. Symbols pertain to binarity as follows: open triangle (star not listed to be a binary by SIMBAD), open circle (double star according to SIMBAD), filled circle (spectroscopic binary), plus symbol (RS CVn star), five-point star (other type of variable).

3.4 Activity of Giants in the Far-Ultraviolet and X-ray

In addition to investigating Mg II *h* and *k* emission as a chromospheric activity indicator, this chapter also seeks to demonstrate the chromospheric activity levels of giant stars with the use of far-ultraviolet photometry. We have analyzed the activity levels of giants with the use of Galaxy Evolution Explorer (*GALEX*) *FUV* magnitude observations. The primary goal of the *GALEX* mission was to observe UV luminosity functions of external galaxies and investigate their star formation histories (see Martin et al. 2005; Salim et al. 2005; Treyer et al. 2005). Along the way, the telescope also observed a plethora of stars, including giants, within the Milky Way. As such, we cross-correlated the Hünsch et al. (1998) sample of 450 giants with the *GALEX* source

catalog, and collected *FUV* magnitude measurements from the GR6/7 *GALEX* data release through the Mikulski Archive for Space Telescopes (Conti et al. 2011).

The activity-*FUV* relationship for FGK main sequence stars, as observed and calibrated by Smith & Redenbaugh (2010); Crandall et al. (2020), is dependent on $(B-V)$ color. A similar circumstance might be expected for red giants which requires an optical color sensitive to photospheric temperature in addition to the above mentioned FUV photometry data. Throughout this chapter we use either *Gaia* colors or Johnson $(B-V)$ for this purpose. The *Gaia* catalog is accessible to all and is often used as the new standard due to its unprecedented precision in measurement.

3.4.1 A *ROSAT*-*GALEX* Cross-matched Sample of Giants

As noted above, we have cross-matched the Hünsch et al. (1998) sample of *ROSAT*-detected giant stars with FUV sources in the *GALEX* GR6/7 catalog. We further cross-matched this sample with *Gaia* early-release DR3 to find those with green and blue photometry, amounting to 191 giants. These stars are listed in Appendix C as Table C.1 with their HD identifiers, *GALEX FUV*, *Gaia* green and blue magnitudes, and *ROSAT* X-ray luminosities. Johnson *BV* photometry is also available for these stars from a variety of sources including the paper of Hünsch et al. (1998) and various *Hipparcos* catalogs.

Uncertainties in the *Gaia* photometry are derived from data in the *Gaia* catalog. Magnitude errors are not directly listed within the catalog because they are asymmetric. The asymmetry does not impact the overall conclusions of this work. As such,

we used the following formula to calculate the standard deviation of *Gaia* magnitudes.

$$\sigma^2_{\rm mag} = \left(\frac{1.086\sigma_F}{F}\right)^2 + \sigma^2_{\rm zp}, \tag{3.3}$$

where F is the observed flux and $\sigma^2_{\rm zp}$ is the zero point error (Jordi 2018). The Vega magnitude zero point errors estimated by the *Gaia* Collaboration are $\sigma_G = 0.0018$, $\sigma_{G_{BP}} = 0.0014$, and $\sigma_{G_{RP}} = 0.0019$.

Errors associated with *GALEX FUV* magnitudes are derived using small number statistics. That is, any star with multiple *GALEX* observations will have an associated error in our plots. The *FUV* error analysis was based on Table 1 of Jeffers (1952), in which for a given sample, the standard deviation is the ratio of the range and a constant mean value given in the table. These errors in *FUV* are relatively small, ranging from 0.008-0.8. In addition, most stars do not have these errors as there were only 78 giants with multiple *GALEX* observations.

We are interested in exploring *GALEX* far-ultraviolet photometry as an indicator of stellar activity in red giants. In order to facilitate this effort we have formulated two combined *FUV*-optical colors: $(FUV - G_{BP})$ from a combination of *GALEX FUV* and *Gaia* photometry, and $(FUV - B)$ from combining *GALEX* and Johnson photometry. It is this second color that has been calibrated as an activity and age indicator for FGK main sequence stars by Crandall et al. (2020).

3.4.2 *Gaia* Color-Magnitude Diagrams for the *ROSAT-GALEX* Giant Sample

Figure 3.2 presents a photometric Hertzsprung-Russell (HR) diagram of the crossed-matched *ROSAT-GALEX* sample of giant stars in which *Gaia* eDR3 (Gaia Collaboration et al. 2018a) observations are used to provide magnitude and color data. Herein, M_G is the *Gaia* green absolute magnitude obtained using *Gaia* parallaxes while the photospheric color plotted is $(G_{BP} - G_{RP})$. The sample can divided into two main groups with a gap around $(G_{BP} - G_{RP}) = 0.8$. To the left of this gap are stars belonging to a main sequence population, or else are very slightly post-main sequence, whereas the red giants are to the right. This figure is similar to that of Figure 10 in the *Gaia* Collaboration's paper on the Hertzsprung-Russell diagram (Gaia Collaboration et al. 2018b), although our sample is much smaller. The HR diagram from the *Gaia* Collaboration is particularly useful due to it being extensively populated by stars in the core-helium-burning phase of evolution. A comparison with Figure 3.2 reveals that a large fraction of the stars in our *ROSAT-GALEX* giant sample are also likely to be in this stage of evolution. This is in contrast to stars ascending the red giant branch (RGB) for the first or second time.

The stars plotted in Figure 3.2 are also shown in a different version of the HR diagram in Figure 3.3 in which M_G is plotted versus the $(G_{BP} - G)$ color. We will employ this particular *Gaia* color below as it is most analogous to the Johnson $(B-V)$ color that we will also use in several following sections.

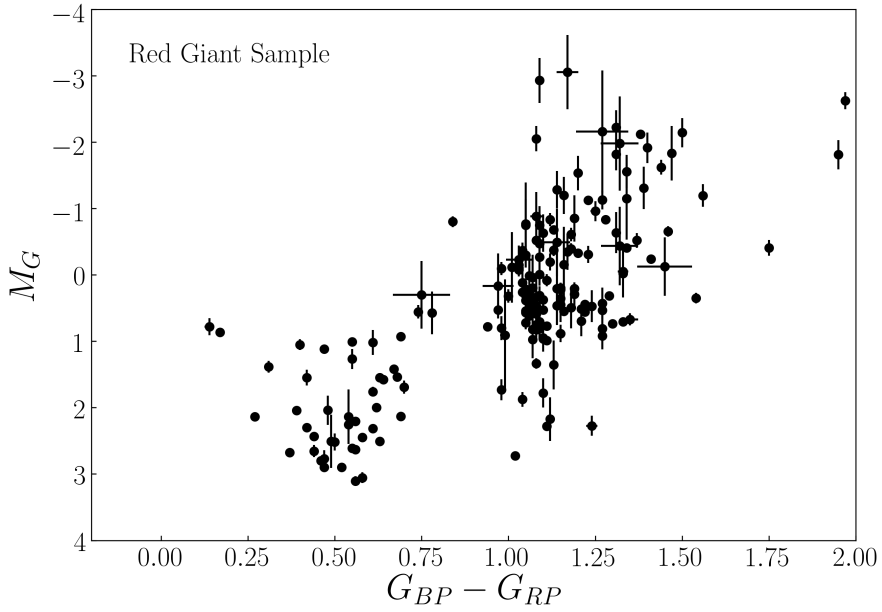

Figure 3.2 An HR diagram of the red giant sample as obtained from *Gaia* photometry and parallaxes: the *Gaia* absolute G magnitude versus the $(G_{BP} - G_{RP})$ color which covers the full wavelength range of the *Gaia* photometric system. Stars to the left of $(G_{BP} - G_{RP}) \lessapprox 0.8$ are close to the main sequence, while stars to the right of this dividing line comprise the red giant sample used in this work.

3.4.3 Identifying CHeB Stars

As noted above, the red-giant sample discussed in Section 3.2 contains core-helium-burning stars. We have identified candidates for CHeB stars in Figure 3.3 through a comparison with MESA evolutionary tracks (Dotter 2016; Choi et al. 2016; Paxton et al. 2011, 2013, 2015). The CHeB stars were expected to fall within $0.4 \lessapprox (G_{BP} - G) \lessapprox 0.8$ and $-1.0 \lessapprox M_G \lessapprox 1.0$. We plotted a range of MESA models and concluded that CHeB stars are bound by the $0.75 M_\odot$ and $3.0 M_\odot$ evolutionary tracks, as represented by the blue and purple lines in Figure 3.3 respectively. The red dots between these tracks in Figure 3.3 are identified as candidate CHeB stars.

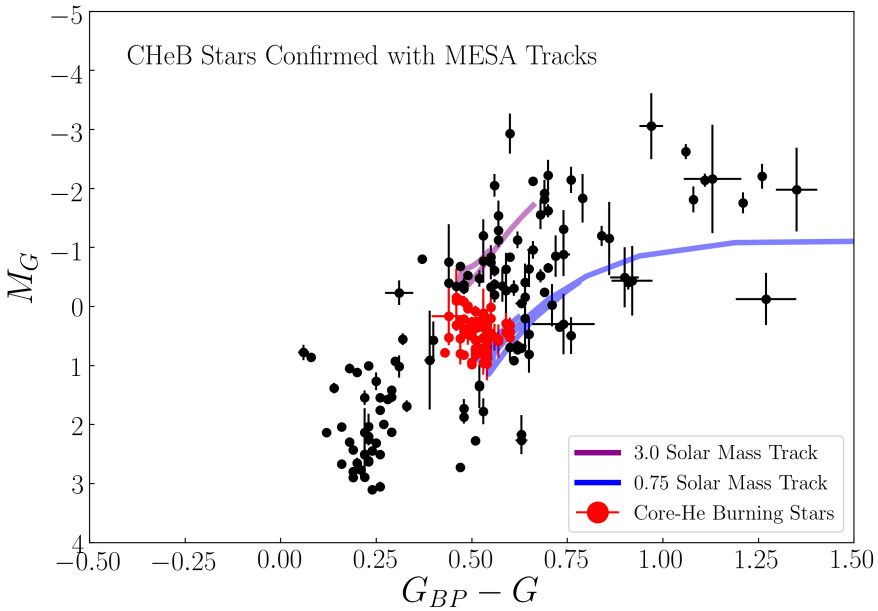

Figure 3.3 An HR diagram of the red giant sample as derived from *Gaia* data. By comparison with Figure 3.2 the color plotted here is $(G_{BP} - G)$. Red dots denote the CHeB stars suggested by the MESA evolutionary tracks. The $0.75M_{\odot}$ (blue) and $3.0M_{\odot}$ (purple) lines are the CHeB segments of the evolutionary tracks, which form a boundary around those stars that are presumed here to be in the core-helium-burning phase of evolution.

3.4.4 A *GALEX-Gaia* Two-Color Diagram

Chromospheric emission is greatly dominated by photospheric flux at most optical wavelengths. However, far-ultraviolet broadband photometry is sensitive to chromospheric and transition region flux,, including that from emission lines. Thus, a color such as $(FUV - G_{BP})$ is expected to be sensitive to stellar activity. Figure 3.4 shows a two-color plot of $(FUV - G_{BP})$ versus $(G_{BP} - G)$ for the *ROSAT-GALEX* red giants selected for this work. The red symbols denote the Population I equivalent of horizontal branch stars (from Figure 3.3) that are likely burning helium in their cores. There is a notable range of $(FUV - G_{BP})$ color among these CHeB stars, suggestive of a range in

chromospheric activity levels.

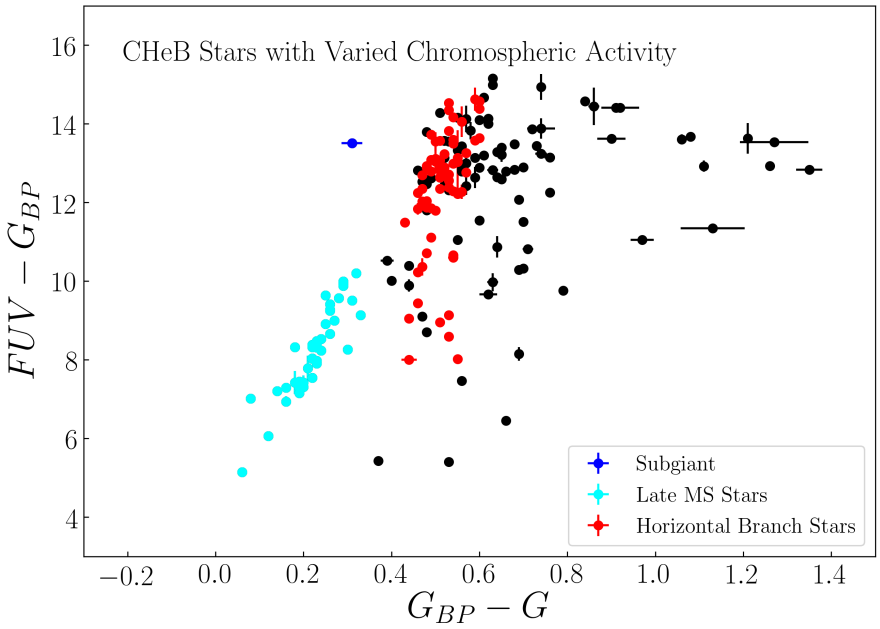

Figure 3.4 An FUV-optical two-color diagram of the red giant sample with *ROSAT* X-ray data plus *GALEX FUV* and *Gaia* photometry. The FUV-based color ($FUV - G_{BP}$) is plotted versus optical ($G_{BP} - G$). The red circles denote horizontal branch CHeB stars as inferred from MESA evolutionary tracks. There is a range in the ($FUV - G_{BP}$) color of the CHeB stars suggestive of a range in chromospheric activity. The dark blue symbol corresponds to an inactive subgiant. The cyan symbols refer to late main-sequence stars. Both cyan and blue symbols refer to pre-RGB stars.

In Figure 3.4 there is a group of bluer stars with a clear separation of activity levels. We have plotted these stars along with MESA evolutionary tracks to identify their evolutionary phase. Figure 3.5 denotes this set of stars in cyan. This population is comprised of late main-sequence stars, which are still maintaining relatively active chromospheres as observed in the far-ultraviolet. The dark blue star in the figure represents an inactive subgiant, as it mostly falls on the red giant segment of the tracks. We defined this star as a subgiant due to its evolutionary position, but not in terms of luminosity. As shown in Figure 3.4, the subgiant is quite inactive; indicating that it has

evolved and spun down. Both late main-sequence and subgiant stars are pre-Hayashi track stars.

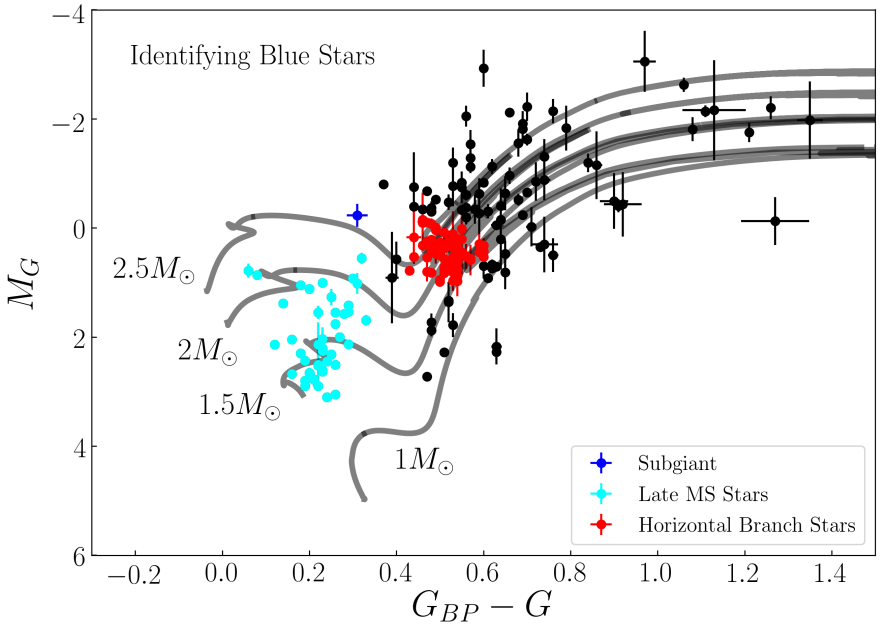

Figure 3.5 MESA evolutionary tracks of 1, 1.5, 2, and 2.5 solar masses over-plot on CHeB stars (red) and two sets of bluer stars. The cyan stars are likely lower mass stars which are exiting the main sequence. The blue star is a more massive subgiant in the evolutionary sense.

3.4.5 An FUV-Excess Parameter

Crandall et al. (2020) calibrated a relationship between FUV magnitude as an indicator of activity and stellar age for dwarf stars. However, it is important to note that this calibration was dependent on Johnson $(B-V)$ color. Dwarf stars with $(B-V) \leq 0.55$ likely have photospheric contamination of the *GALEX* FUV band and so the calibration was unreliable in that color range. Figure 3.6 shows the distribution of $(B-V)$ measurements for those subgiant and late-main sequence stars in the Hünsch

et al. (1998) catalog that forms the basis of our *ROSAT-GALEX* sample. The majority of these stars have $(B-V) \leq 0.55$. As such, the photospheric flux likely impacts the reliability of the *FUV* magnitude as an indicator of their chromospheric activity.

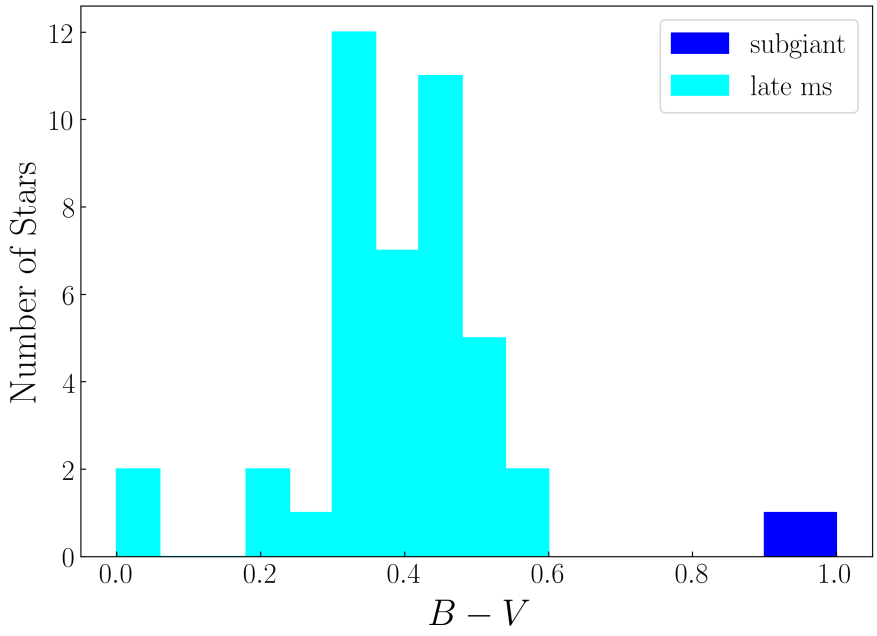

Figure 3.6 Distributions of $(B-V)$ color for the subgiant and late-main-sequence stars in the *ROSAT-GALEX* cross-matched sample.

To quantify chromospheric effects on *FUV*-optical colors of giant stars, Figure 3.7 shows a two-color plot for a large sample of giant stars drawn from a rotational velocity study by Massarotti et al. (2008). Both *GALEX FUV* magnitudes and Johnson B and V magnitudes from the *Hipparcos* Input Catalogue have been compiled here for the Massarotti et al. (2008) sample. The stars in their sample have a fuller coverage at redder $(B-V)$ color than the stars in our *ROSAT-GALEX* cross-matched sample. The two-color diagram in Figure 3.7 shows $(FUV-B)$ versus $(B-V)$ for giants with $(B-V) > 0.75$, and as such does not include late-main-sequence stars such as those

from the Hünsch et al. (1998) *ROSAT* sample.

To compare FUV and X-ray emission as activity indicators we first introduce a FUV-excess parameter, Q_{FUV}, based on the Massarotti et al. (2008) sample (see similar excess parameters defined in Crandall et al. 2020; Dixon et al. 2020; Smith et al. 2017; Findeisen et al. 2011). Here Q_{FUV} is defined as

$$Q_{FUV} = (FUV - B) - u, \tag{3.4}$$

where B is the Johnson blue magnitude and u corresponds to an empirically-chosen relation between $(FUV - B)$ and $(B - V)$ for red giants having minimal levels of chromospheric activity. The minimum-activity locus of u versus $(B - V)$ is plotted in Figure 3.7 as a red line, and it is intended here to represent the boundary of minimum FUV-activity for a given $(B-V)$ color among the Massarotti et al. (2008) sample. The locus for u was determined to fit the quadratic function

$$u = -7.36(B - V)^2 + 16.62(B - V) + 4.84. \tag{3.5}$$

We have used Johnson BV photometry rather than *Gaia* photometry to define the FUV-excess parameter Q_{FUV} such that our following results for giant stars can be readily compared with the work of Crandall et al. (2020) for main sequence stars.

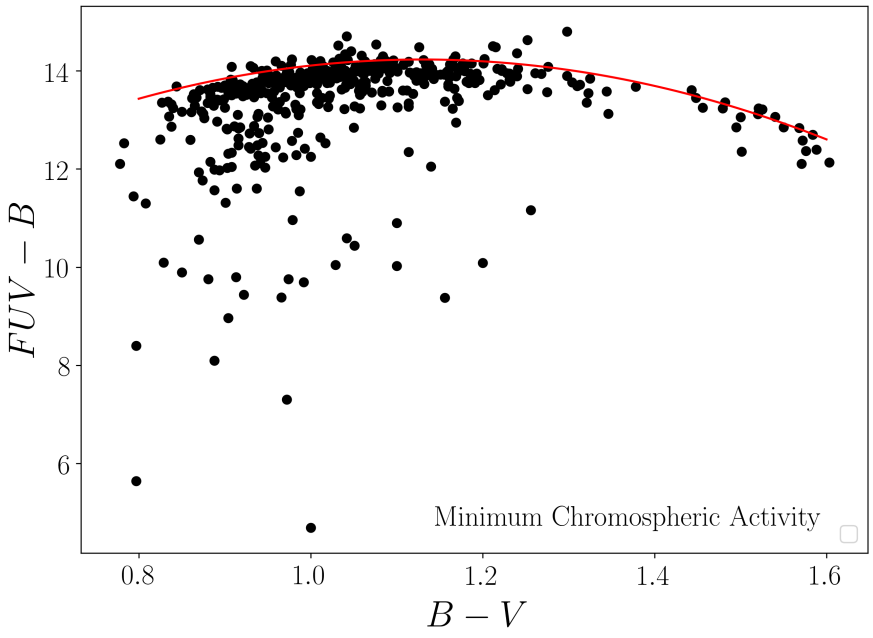

Figure 3.7 A $(FUV-B, B-V)$ two-color diagram for the Massarotti et al. (2008) sample of red giants with *GALEX* *FUV* and Johnson photometry. The red line represents an empirically chosen-color, defined in the text as u, which is taken to correspond to the $(FUV - B)$ color as a function of $(B - V)$ for red giants with minimal levels of chromospheric activity.

3.4.6 An X-ray and *FUV* Activity Comparison

We next compare the chromospheric activity parameter Q_{FUV} based on *GALEX* observations to coronal activity using *ROSAT* X-ray observations. Figure 3.8 shows the *FUV*-excess parameter Q_{FUV} versus X-ray to bolometric luminosity ratio, $\log(L_{\rm X}/L_{\rm bol})$. Not included are stars from Figure 3.5 with $0.0 \leq (B - V) \leq 0.6$, as this is a range in which we were unable to define the minimum chromospheric-activiy locus, u, in Figure 3.7. This limit excludes all of the late-main sequence stars (cyan), and reduces the sample size to one subgiant, 59 CheB, and 79 other giant stars.

Correlations between Q_{FUV} and $\log(L_{\rm X}/L_{\rm bol})$ in Figure 3.8 were constrained for three samples: all giants in the figure (green), CHeB stars (red), and other giants

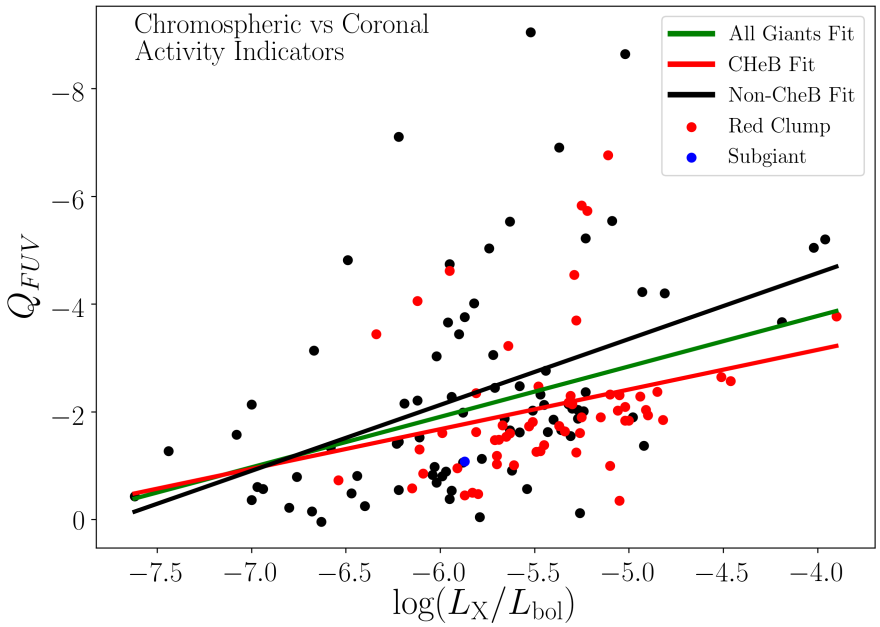

Figure 3.8 A comparison of chromospheric activity level as seen in the *FUV*, denoted by *FUV*-excess parameter Q_{FUV}, and coronal activity level, denoted by $\log(L_X/L_{bol})$. Stars in the CHeB phase (red) and other giants (black) show a range of both coronal and chromospheric activity levels. Correlations were fitted for three samples: all giants in the figure (green line), CHeB stars (red line), and other giants (black line).

(black). These fits take the forms of

$$Q_{FUV} = -0.74 \log(L_X/L_{bol}) - 6.09 \tag{3.6}$$

for the red clump fit,

$$Q_{FUV} = -1.22 \log(L_X/L_{bol}) - 9.47 \tag{3.7}$$

for the other giant fit (non-CHeB giants), and

$$Q_{FUV} = -0.94 \log(L_X/L_{bol}) - 7.52 \tag{3.8}$$

Table 3.2 Fits for FUV-Excess Parameter Q_{FUV} versus $\log(L_{\rm X}/L_{\rm bol})$

Sample[a]	N[b]	a[c]	b[c]	ρ[d]	r^2[e]	rms[f]
CHeB Giants	59	-0.74	-6.09	-0.42	0.07	1.28
Non-CHeB Giants	79	-1.22	-9.47	-0.49	0.19	1.76
All Giants and Subgiant	139	-0.94	-7.52	-0.43	0.12	1.60

[a] Sample of giants
[b] Number of stars within each sample
[c] Fit parameters of $Q_{FUV} = a\log(L_{\rm X}/L_{\rm bol}) + b$
[d] Spearman Coefficient
[e] Coefficient of Determination
[f] Root mean square variation of Q_{FUV}) about each fit

for all giants in the figure. The rms scatter in Q_{FUV} about the fits to CHeB giants, non-CHeB giants, and the full sample in Figure 3.8 are 1.28, 1.76, and 1.60 mag, respectively. This scatter is considerable compared to the observational uncertainty in the FUV magnitude, which in turn dominates the uncertainty in Q_{FUV}. The fit parameters, rms about Q_{FUV}, as well as the Spearman correlation coefficient, ρ, and coefficient of determination are listed in Table 3.2. We note that these fits have significant errors due to the scatter in Q_{FUV}. There is also little correlation between Q_{FUV} and $\log(L_{\rm X}/L_{\rm bol})$ as evident in the poor Spearman coefficients.

Figure 3.8 shows that while we see a range of atmospheric activity for giants, as indicated by both FUV and X-ray observations, there is significant scatter between the two indicators. We investigated binarity as a possible contribution to this phenomenon. In Figure 3.9 we show the X-ray ratio versus Q_{FUV} while targeting certain populations of stars: no variable stars, RS CVn, visual, symbiotic, or spectroscopic binaries (top left); no spectroscopic, RS CVn, or symbiotics binaries (top right); only spectroscopic,

RS CVn, and symbiotic binaries (bottom left); and all RS CVn, visual, symbiotic, and spectroscopic binaries (bottom right). Binarity for each star was found in the SIMBAD online data system. There is a reduced amount of scatter in Q_{FUV} for the population that does not include any binaries or variable stars.

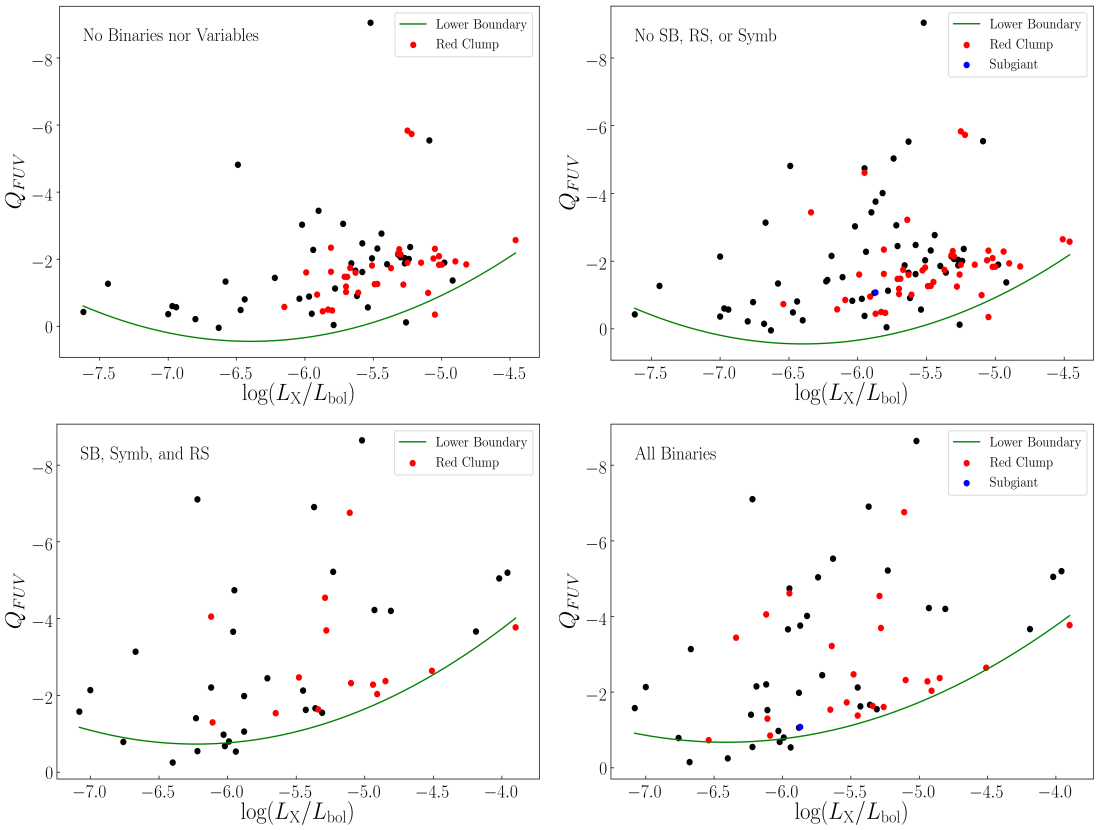

Figure 3.9 Far-ultraviolet excess parameter (Q_{FUV}) versus the ratio of X-ray luminosity over bolometric luminosity for four populations: no variable stars, RS CVn variables, visual, symbiotic, or spectroscopic binaries (top left); no spectroscopic, RS CVn, or symbiotic binaries (top right); only spectroscopic, RS CVn, and symbiotic binaries (bottom left); and all RS CVn, visual, symbiotic, and spectroscopic binaries (bottom right). Green lines indicate a lower boundary for Q_{FUV} as calculated for the samples in each panel.

In addition to the least squares fits discussed above, a lower boundary for

Q_{FUV} is shown as a green quadratic fit in Figure 3.9. The boundaries take the forms

$$Q_{FUV} = -0.70 \log(L_{\rm X}/L_{\rm bol})^2 - 8.99 \log(L_{\rm X}/L_{\rm bol}) - 28.29 \tag{3.9}$$

for the sample of giants without binaries or variables,

$$Q_{FUV} = -0.70 \log(L_{\rm X}/L_{\rm bol})^2 - 8.99 \log(L_{\rm X}/L_{\rm bol}) - 28.29 \tag{3.10}$$

for the sample without spectroscopic, RS CVn, or symbiotic binaries,

$$Q_{FUV} = -0.60 \log(L_{\rm X}/L_{\rm bol})^2 - 7.53 \log(L_{\rm X}/L_{\rm bol}) - 24.19 \tag{3.11}$$

for the sample of spectroscopic, RS CVn, and symbiotic binaries, and

$$Q_{FUV} = -0.53 \log(L_{\rm X}/L_{\rm bol})^2 - 6.81 \log(L_{\rm X}/L_{\rm bol}) - 22.51 \tag{3.12}$$

for the sample with all binaries. These lower boundaries were determined by fitting the most positive Q giant at a given $L_{\rm X}/L_{\rm bol}$. The top two panels of Figure 3.9 have identical lower boundaries, as there is little difference in these two samples for giants existing near the boundaries.

There are five stars with $Q_{FUV} < -4$ in the top left panel of Figure 3.9 which are not binaries nor variables: HD 24497, HD 28525, HD 47442, HD 11025, and HD 12055. These giants are quite active as indicated by their Q_{FUV} values. However, their activity is more apparent in the ultra-violet than in X-ray. As they are single stars, their

activity levels are not impacted by companions. Additionally, they are not pulsating. It was of interest to investigate their *GALEX FUV* measurements. The left panel of Figure 3.10 shows Q_{FUV} versus *GALEX FUV* magnitudes for the population of stars in the top left panel of Figure 3.9. The five stars with $Q_{FUV} < -4$ have the brightest *FUV* apparent magnitudes in the sample, indicating that their *GALEX* observations would not likely have errors from being faint sources. A plot of Q_{FUV} versus Johnson $(B-V)$ color for this population is shown in the right panel of Figure 3.10, from which it is apparent that these five stars are not different in effective temperature from the CHeB and giant peers. The nature of these sources is unclear to us. It is possible that these are observational artifacts or a confusion of two unresolved sources in the *GALEX FUV* images. One possible explanation for the very negative Q_{FUV} values for the five stars might be a white dwarf companion, but there is no indication from the SIMBAD database to suggest such might be the case.

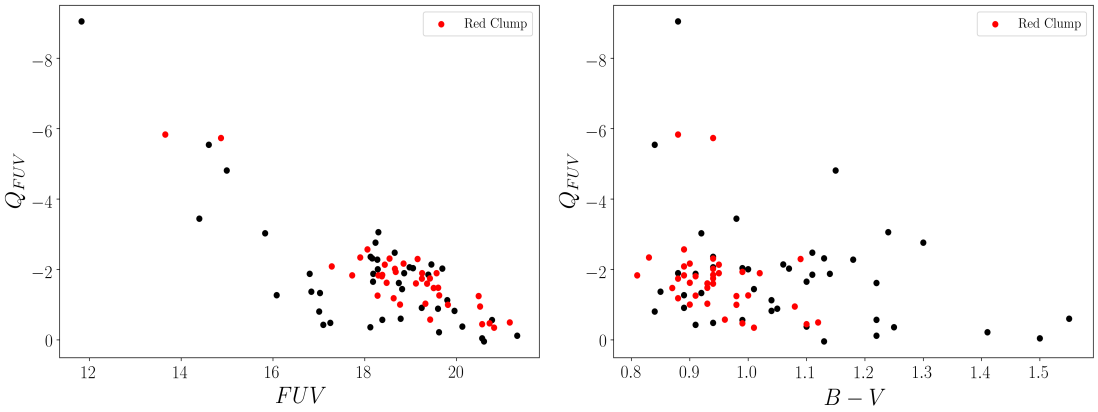

Figure 3.10 *FUV*-excess parameter, Q_{FUV}, versus *GALEX FUV* observations (left) and Johnson colors, $(B-V)$, (right) for the single giants (no binaries nor variables) in top left panel of Figure 3.9. Relatively active stars with $Q_{FUV} < -4$ are bright in the *FUV*.

In addition, far-ultraviolet saturation can lead to an underestimation of flux

for *GALEX* sources brighter than both *NUV* and *FUV* $m_{\rm AB} \sim 15$ (Morrissey et al. 2007). As such, we have recreated the top left panel of Figure 3.9 without the sources with $FUV > 15$ in Figure 3.11. The fit between $(FUV - G_{BP})$ color versus the ratio of X-ray luminosity over bolometric luminosity is shown in green and has an rms about $(FUV - G_{BP})$ of 0.64. The Spearman coefficient, ρ, for the population is -0.53 and has an $r^2 = 0.27$. We conclude that the correlation shown in fit of Figure 3.11 is not a strong one.

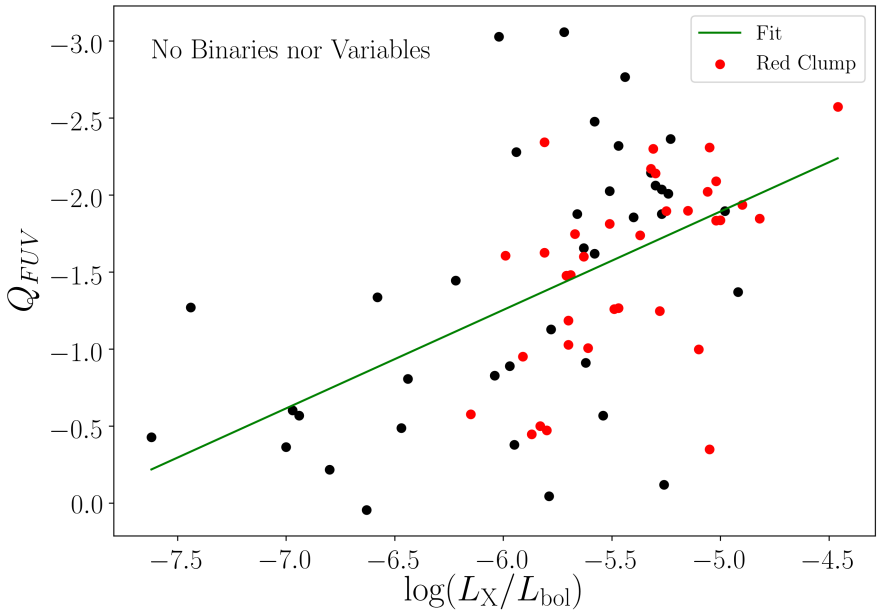

Figure 3.11 $(FUV - G_{BP})$ color versus the ratio of X-ray luminosity over bolometric luminosity for the population of stars without binaries or variables and $FUV \leq 15\ m_{\rm AB}$. The linear fit is shown in green and has an rms fit about $(FUV - G_{BP})$ of 0.65.

While red clump stars show a range in chromospheric activity, the late-main sequence stars do not trace similarly in the far-ultraviolet as in X-ray wavelengths. This is evident in the scatter shown in Figures 3.8, 3.9 and 3.11. We do note that we do not suspect binarity to play a significant role in this scatter.

This work demonstrated a greater utility in identifying activity levels with Mg emission lines as compared to broadband *FUV* chromospheric emission. The benefit of using Mg II emission lines is that they arise from a single species in a single ionization state, and thus probe a specific region of the chromosphere. By comparison when utilizing *FUV* emission as an activity indicator we are sampling a combined sum of multiple emission lines from a variety of species in different ionization states. Thus, the chromospheric emission lines within the *GALEX FUV* band do not vary in strength in the same way as a function of effective temperature. That is, not all emission lines reach their maximum populations at a given effective temperature. Thus, there is a downside of having a heterogeneous blend of emission lines varying with effective temperature in different ways. This variance may act to obscure the manner in which *FUV* brightness traces atmospheric activity. Chromospheric emission line strengths of G and K-type cool stars were compared in Ayres et al. (1981). In their Figures 2 and 3, they demonstrated that K stars have weaker chromospheric emission line strengths than G stars. This is particularly the case for giant stars. Thus, despite the fact that the K stars have less photospheric contamination in the *FUV* band, the contrast between the chromospheric and photospheric contributions is less defined than for G stars. This heterogeneity of emission lines within the *FUV* passband may be why it is more difficult to interpret activity levels with the *FUV* indicator than with the single strong pair of Mg emission lines. CHeB stars have emission lines more similar to G-type stars and so it is reasonable to more obviously track their *FUV* activity.

3.5 The Stellar Activity-Rotation Relationship in Giants

Many observations show a relationship of a slowing stellar rotation with age in FGK dwarf stars. However, the relationship may not be the same for giants as for dwarfs. Wang et al. (2020) showed a relation of R_X versus $P_{\rm rot}^{-2}R^{-4}$, where R_X is the X-ray to bolometric luminosity ratio, $P_{\rm rot}$ is the rotation period and R is the stellar radius for dwarf stars. They did not find the same relationship for giants. In this section we examine the stellar activity - rotation relationship of giants stars using *GALEX FUV* and *NUV* and $v\sin i$ rotation measurements.

3.5.1 *FUV*-Rotation Relation

A large sample of red giant stars with rotational velocities were needed in order to have a reasonable number of stars when cross-matched with the *GALEX* catalog. The sample used in this analysis was derived from Massarotti et al. (2008) who determined rotational velocity measurements for 761 giants within 100 pc of the Sun. Massarotti et al. (2008) determined rotational velocities for all giants with spectra observed with CFA Digital Speedometers (Latham 1992) on the Wyeth Reflector at Oak Ridge Observatory and Tillinghast Reflector and MMT at the Whipple Observatory. Spectra was then cross-correlated with synthetic spectra templates from Kurucz (1992). We cross-matched the Massarotti et al. (2008) catalog with the *GALEX* archive and *Hipparcos* catalog which resulted in a sample of 267 giants with rotational velocities and *FUV* and Johnson B magnitudes. Three of these stars have quoted rotational velocities of $v\sin i > 32$ km/s. There are zero stars with rotational velocities between $v\sin i \sim 15$

km/s and these three stars. With such a large gap, it is not enlightening to include the three fast rotating stars in our attempt to correlate Q_{FUV} and rotational velocity. These three stars are HIP3693 (RS CVn, K1 giant Koevari et al. 2007), HIP75127 (K1 giant Houk & Swift 1999), and HIP112748 (G8 giant Keenan & McNeil 1989). We were then left with 262 giant stars in our sample.

Figure 3.12 shows *GALEX FUV*-excess parameter, Q_{FUV}, versus Massarotti et al. (2008) rotational velocities for the 262 giants. Q_{FUV} values were determined by Equations 3.4 and 4.3. We do not see a clear correlation between ultraviolet radiation and rotation for stars with $v\sin i <$ 7 km/s in this figure. A possible explanation for the scatter in Figure 3.12 is that we do not know the inclinations. Such variations in $v\sin i$ may obscure any trends. Stars bright in the *FUV* may have intrinsically high rotation, but the inclination is close to the line of sight of the star. Thus, we would not see the full rotation. The lack of correlation we observed in Figure 3.12 would then be a projection effect.

We further investigated the giants in Figure 3.12 with very negative Q_{FUV} values, those with $Q_{FUV} \leq -4.0$. Eleven stars fall in that regime, with eight of them being binaries: HIP7097, HIP10661, HIP23221, HIP52085, HIP53240, HIP62886, HIP74896, and HIP78481. HIP68904 is identified as a pulsating star (Strassmeier et al. 2011), which may impact observations of activity levels. The remaining two stars, HIP79882 and HIP94490, designated with "+" symbols in Figure 3.12 are not binaries, but high proper motion giants.

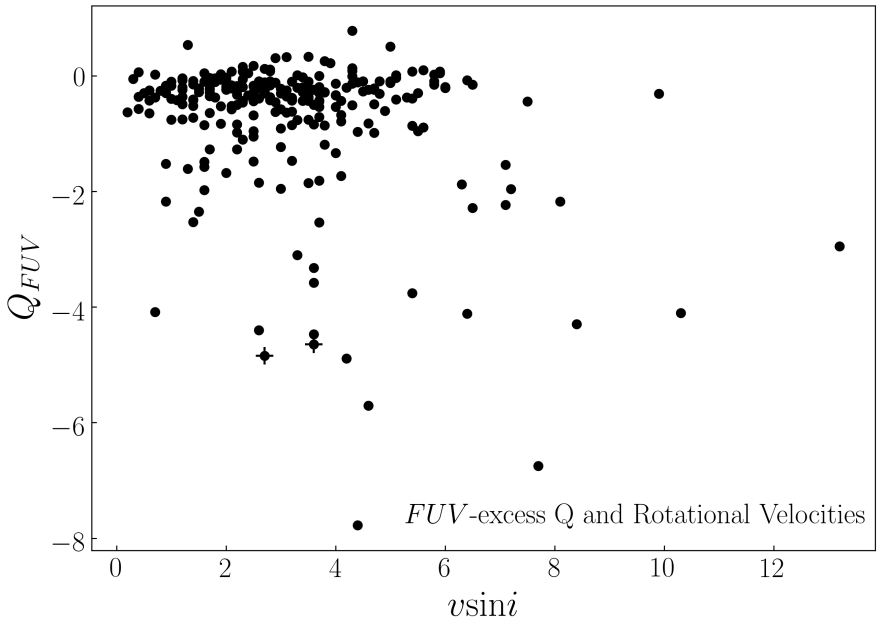

Figure 3.12 *GALEX* FUV-excess parameter, Q, versus rotational velocities for giant stars from Massarotti et al. (2008). We do not include six stars with $v\sin i > 15$, as there is large scatter at this regime. The two giants with a "+"" symbol are those with very negative Q_{FUV} values, < -4, but are not a binary.

3.5.2 NUV-Rotation Relation

Near-ultraviolet (NUV) emission has been shown to correlate with rotational velocities for red giants stars by Dixon et al. (2020). Similar to the analysis in Dixon et al. (2020) we defined an NUV-excess, described here as Q_{NUV}. This excess is defined by

$$Q_{NUV} = (NUV - B) - u, \tag{3.13}$$

where NUV is *GALEX* observed near-ultraviolet emission, B is the Johnson magnitude, and u is now a boundary value that defines the NUV-excess. Figure 3.13 shows a two-color diagram of the Massarotti et al. (2008) sample of giants with *GALEX* NUV observations. The red line in this figure defines u, and it is likely an effective temperature

trend. It is not a locus purely defined by chromospheric activity, as the NUV passband contains both photospheric and chromospheric light. The locus is defined by

$$u = -4.30(B-V) + 14.91(B-V) - 3.73. \tag{3.14}$$

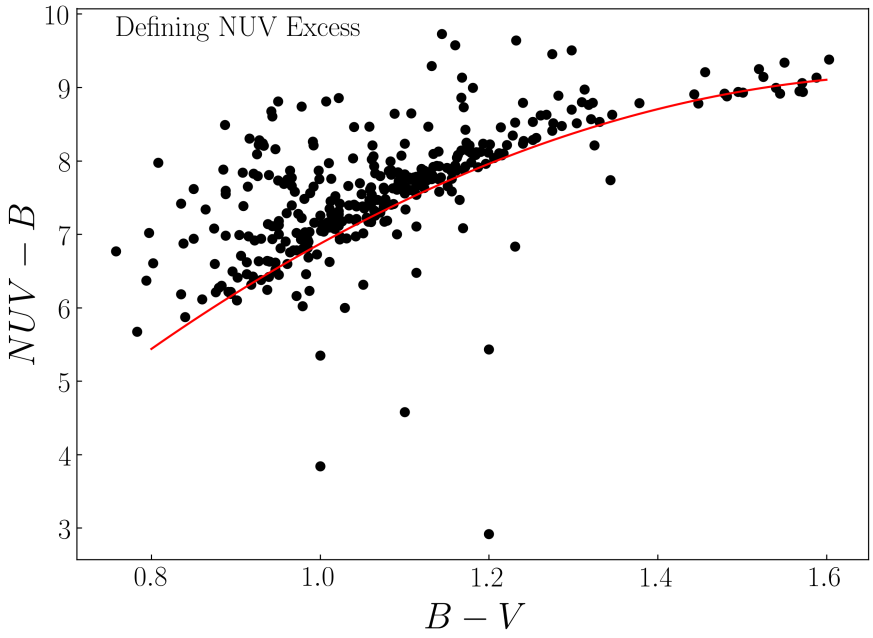

Figure 3.13 Two-color diagram of Massarotti et al. (2008) sample of giants with *GALEX* NUV observations. Johnson $(B-V)$ colors were collected from the *Hipparcos* catalog.

We show the NUV-excess, Q_{NUV}, versus rotational velocities, $v\sin i$, in Figure 3.14. A clear correlation is not evident, and we were were unable to fit this relationship. Dixon et al. (2020) demonstrated and fit such a relationship in their Figure 7. However, we note that their sample contained a larger number of stars with $v\sin i > 10$ km/s. Below this limit the relationship is less evident in both our work and theirs.

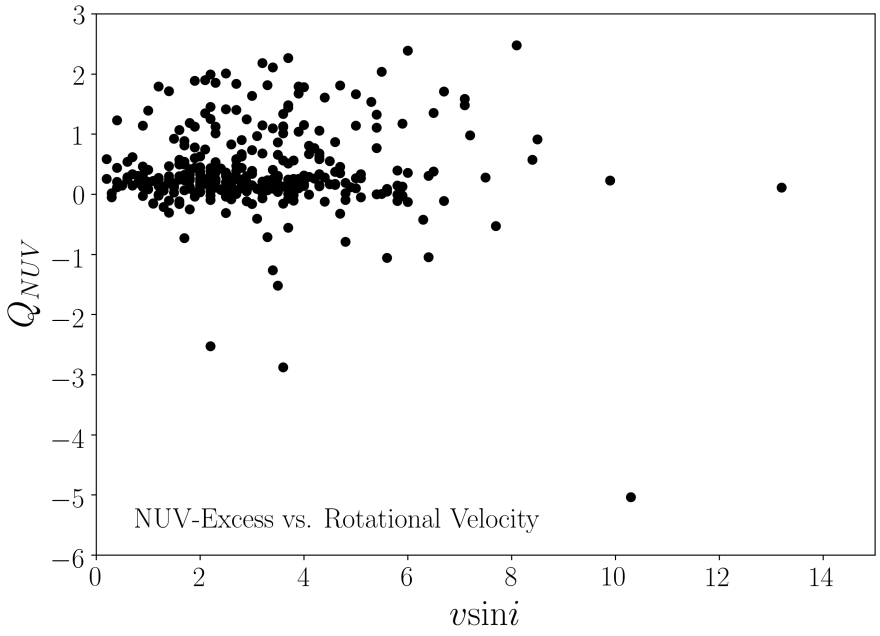

Figure 3.14 Near-ultraviolet excess parameter, Q_{NUV}, versus rotational velocities from Massarotti et al. (2008).

3.6 Conclusion

A sample of 450 giants and subgiants from Hünsch & Schröder (1996) was cross-matched with Pérez Martínez et al. (2011) to obtain a sample of giants with Mg II and *ROSAT* X-ray emission flux. We found an evident correlation between $\log(L_{\rm X}/L_{\rm bol}) > -6.0$ and $\log(F_{\rm MgII}/F_{\rm bol}) < -4.8$ for this cross-matched sample. This correlation was apparent even though the sample was primarily comprised of binary giants. We find that relatively high-activity stars mostly contribute to this correlation, and that there is a large range of $\log(L_{\rm X}/L_{\rm bol})$ for giants with comparable $\log(F_{\rm MgII}/F_{\rm bol})$ and $(B-V)$ color.

We identified 66 core-helium burning stars from the Hünsch & Schröder (1996) catalog of 450 giants and subgiants. These giants have *ROSAT* X-ray emission ob-

servations and were verified as CHeB with MESA evolutionary tracks. Additionally, these 66 giants have *GALEX FUV* emission observations and *Gaia* G_{BP} magnitudes. The CHeB stars in our sample demonstrate a wide range of $(FUV - G_{BP})$ colors: $8.00 \leq (FUV - G_{BP}) \leq 14.63$. As FUV magnitudes have been demonstrated as a chromospheric activity indicator, we conclude that there is a varied range of activity levels for the CHeB stars. This range of activity levels demonstrates that CHeB stars may be receiving a magnetic field boost in this late stage of stellar evolution.

While we see a range of stellar activity in the far-ultraviolet of CHeB stars, the activity is not traced by FUV and X-ray emission in a similar manner. Despite this difference, we constrained a relationship between $(FUV - G_{BP})$ and $\log(L_{\rm X}/L_{\rm bol})$ for giants with Johnson colors $(B - V) > 0.62$ and $(FUV - G_{BP}) > 11$. Binaries were not included in this constrained, linear relationship. Additionally, identified subgiants and late-MS stars, while still clearly separated in activity levels as seen in the far-ultraviolet, share a similar range in activity levels to CHeB giants as observed with X-ray observations.

We endeavored to constrain correlations between rotational velocities and *GALEX* ultraviolet emission for a sample of giants from Massarotti et al. (2008). However, a clear correlation was not evident between ultraviolet emission and $v\sin i$. The scatter in our plots may be a consequence of a lack of inclination constraints, thus obscuring a relationship.

Chapter 4

Age-Velocity Relations with *GALEX* *FUV*-Determined Ages of Solar Neighborhood Dwarf Stars

4.1 Introduction

The velocity dispersion of solar neighborhood, FGK main sequence stars has been shown to increase with age. This so-called age-velocity dispersion relation (AVR) has been examined over the decades (Strömberg 1946; Spitzer & Schwarzchild 1951; Wielen 1977; Seabroke & Gilmore 2007; Soubiran et al. 2008). Constraints on this relation lend to a better understanding of the mechanisms which formed the Milky Way

galaxy. The velocity dispersion increase with stellar age may be the result of several factors, including how the Milky Way initially formed. Rix & Bovy (2013) reviews the study of Galactic evolution and mechanisms that may have played a role to form the current state of the AVR. One explanation posits that orbits of stars were determined at birth. Vertical gradients of age and metallicity in this case are fixed as a consequence of the initial gas settlement of the disc, and radial gradients are formed "inside out" (see e.g. Veltz et al. 2008; Robin et al. 2014; Navarro et al. 2018). The initial determination of orbits may in turn have been the result of several mechanisms, including early mergers (Brook et al. 2004, 2012), accretion from satellite galaxies (Abadi et al. 2003), and trends in the star formation (Bird et al. 2013). Alternately, the observed AVR is often argued to be the result of orbital scattering or dynamical heating of a stellar distribution after gas settled into a thin disc. As such, older stars subsequently had more time to gravitationally interact with other massive objects and become scattered into altered orbits.

A number of numerical modeling studies have been made to explore the latter possibility that heating mechanisms may play a significant role in producing the observed AVR. Simulations have demonstrated how gravitational interactions can cause heating through a variety of mechanisms. In earlier studies Giant Molecular Clouds (GMCs) were presumed to be the main driver of Galactic heating (Spitzer & Schwarzchild 1951, 1953), yet in recent years simulations have shown that multiple mechanisms contribute to the observed AVR (see, for example, Hänninen & Flynn 2002; Aumer et al. 2016). The spiral arm structure and a possible bar (Barbanis & Woltjer 1967; Aumer et al. 2016),

black holes (Lacey & Ostriker 1985; Hänninen & Flynn 2002), and satellite mergers (Walker et al. 1996; Moetazedian & Just 2016; Ting & Rix 2019) may all play a role in Galactic heating. The resulting models can be tested with observations of the solar neighborhood AVR.

More often than not, the stellar ages utilized in observational determinations of the local AVR are based upon isochrone-determination techniques. In isochrone fitting one makes use of a comparison between an observed color magnitude diagram which contains the stars of interest and theoretical isochrones or evolutionary tracks for stellar models of varied ages. This method is useful when age-dating co-evolved stars such as clusters and moving groups, but can result in uncertain ages when age-dating single stars. The Geneva-Copenhagen Survey (GCS) (**?**) contains a plethora of stars which have been used to construct AVRs (Holmberg 2009; Casagrande et al. 2011), and it is often used as a standard for comparison. The GCS contains 16,682 G and F-type stars within the solar neighborhood with metallicity, rotation, age, kinematics, and Galactic orbits determinations. Kinematics for this sample used *Hipparcos* parallaxes, Tycho-2 proper motions, and $uvby\beta$ photometry. Stellar ages within this work were determined with isochrone modeling. This well-used sample can test our understanding of the Milky Way's evolution by providing the data from which a local stellar AVR can be derived. For example, Figure 8 of Holmberg (2009) uses distances, ages, and kinematics from the GCS to show synthetic age-velocity relations for three different disc heating scenarios (scattering, heating saturation, and a late minor merger). Like with many AVR analyses, the GCS AVR is often derived using isochrone-determined stellar

ages. We see in Figure 17 of Casagrande et al. (2011) that the use of different isochrone models can alter the shape of the AVR given the GCS sample.

While in recent years isochrone ages have been improved through the use of Bayesian techniques, stars greater than ∼2 Gyr still have significant scatter between determined-ages as compared within the literature (see Figure 4a of Lin et al. 2018). Such scatter illustrates a need for additional types of age-dating techniques which may be applied to single stars. Then one may compare AVRs constructed with stellar ages determined from a variety of methods. Ages of FGK main sequence stars based on the time-varying behavior of stellar activity can provide one such potential alternative (Strömberg 1946; Roman 1950a,b).

In Crandall et al. (2020) the stellar activity-age relationship is the basis of a calibration between stellar age and far-ultraviolet (FUV) brightness which can be added to the toolbox of other age-dating techniques. Therein FUV magnitude observations from the Galaxy Evolution Explorer Telescope ($GALEX$) are shown to be tracers of chromospheric activity (see e.g. Smith & Redenbaugh 2010) and hence age (Findeisen et al. 2011). Crandall et al. (2020) derived an FUV-age calibration through which ages may be determined without introducing errors associated with model-based methodologies, such as isochrone fitting.

The FUV-age relationship in Crandall et al. (2020) is calibrated in a combined *GALEX* FUV and Johnson B & V color space. In Section 4.2 of this work we re-calibrate the relationship in *GALEX* plus *Gaia* color space, as *Gaia* photometry is now available for a much larger number of stars than is $(B-V)$ photometry. In Section

4.3 the updated FUV-age calibration is utilized to determine model-independent ages of 660 GCS stars. A stellar AVR is constructed using FUV-determined ages and unprecedentedly precise *Gaia* kinematics. The resultant observational AVR is fitted to a power law whose coefficients are compared with other determinations in the literature. Finally, we utilize perigalactic radii, eccentricities, and FUV-determined ages to show that the stars in our sample follow an "inside out" and "upside down" formation history pattern. Section 4.5 summarizes our findings.

4.2 A Far-Ultraviolet Excess Correlation with Stellar Age

Far-ultraviolet (FUV) emission has been shown to be an indicator of chromospheric activity and hence age (Smith & Redenbaugh 2010; Findeisen et al. 2011; Smith et al. 2017) among FGK main sequence stars. Within Crandall et al. (2020), this relationship was characterized such that one may use *GALEX* FUV magnitudes and Johnson $(B-V)$ colors to estimate the age of FGK dwarf stars. The relationship takes the form

$$log_e(\tau) = log_e(a) + bQ, \tag{4.1}$$

where τ is the stellar age in Gyr, Q is an FUV-excess parameter, and a and b are linear fit parameters. The Q parameter is dependent on *GALEX* FUV magnitude and Johnson $(B-V)$ color. The fit parameters a and b are also dependent on $(B-V)$. However, $(B-V)$ colors are not always available for a stellar sample. With the recent *Gaia* data releases we find that *Gaia* colors are now available for many more Galactic FGK stars than Johnson photometry. As such, within this Section we establish a new

FUV-age relationship for Sun-like stars through the use of *Gaia* colors.

4.2.1 Data Compilation

Development of our new age-calibration comes from a similar *FUV*-based analysis to (Crandall et al. 2020) in which stellar age data from four catalogs were combined to produce a set of calibration stars. Each of these catalogs, Ballering et al. (2013); Isaacson & Fischer (2010); Sierchio et al. (2014); Lorenzo-Oliveira et al. (2018), contain FGK dwarf stars with solar-like luminosities, metallicities, and spectral types. The ages in these four catalogs were primarily determined by stellar activity indicators such as the chromospheric Ca II HK emission index $\log R'_{\rm HK}$. Ballering et al. (2013) and Sierchio et al. (2014) utilized chromospheric and X-ray activity indicators supplemented with surface gravity measurements and gyrochronology, if available, to derive stellar ages. Their estimated ages were then checked against isochrone-determined estimates for consistency. Ages estimated in Isaacson & Fischer (2010) were derived via $\log R'_{\rm HK}$ and calibrations from Mamajek & Hillenbrand (2008). Finally, ages for a few stars in our sample from Lorenzo-Oliveira et al. (2018) were solely estimated from Yonsei-Yale isochrones (Yi et al. 2001; Kim et al. 2002). The oldest star in our sample is 9 Gyr. We treated each stellar entry in these papers separately, i.e., if a star appears in more than one catalog the age values were not combined, as the methods used to determine ages from each source are not always comparable.

Many of the stars in the catalogs have *GALEX FUV* and *Gaia* $G_{\rm BP}$ and G magnitudes, information vital to the *FUV*-age calibration. *GALEX* magnitudes were extracted from the GR6/7 data release, with many of said observations coming from

the All-Sky Imaging Survey collected from the Mikulski Archive for Space Telescopes (Conti et al. 2011). *Gaia* magnitudes were collected from Data Release 2 (DR2) and early Data Release 3 (eDR3) (Gaia Collaboration et al. 2018a).

Additionally, our sample consisted of stars which have Johnson $(B-V)$ colors for the purpose of extracting Sun-like stars with Solar magnitudes and colors. The Johnson colors were collected from the *Hipparcos* catalog. We only considered those dwarfs which fell into a solar color range of $0.55 \leq (B-V) \leq 0.71$ and an absolute magnitude within ± 0.5 mag of the Sun: $4.3 \leq M_{\rm V} \leq 5.3$. More luminous stars have weakened chromospheric activity emission lines used in age-estimations within the catalogs, and so will not have as reliable ages. Absolute magnitudes were determined with *Gaia* parallaxes. These restrictions ensure that we considered stars with spectral types and luminosities similar to that of the Sun.

After the above color and magnitude cuts were placed on the sample of stars from Isaacson & Fischer (2010); Ballering et al. (2013); Sierchio et al. (2014); Lorenzo-Oliveira et al. (2018), we were left with a collection of 401 stars with Sun-like luminosities, effective temperatures, and spectral types. To address metallicity, a histogram of [Fe/H] is plotted (Figure 4.1) for all stars. The metallicity values are taken from Casagrande et al. (2011), and fall within a range of $-1.5 \leq$[Fe/H]≤ 0.76. Of the stars within the sample, 74% or 295 dwarfs, fall within a solar-like metallicity range of $-0.2 \leq$[Fe/H]≤ 0.2. The sample has a near Sun-like range in [Fe/H] and we did not see a need to reduce the sample further based on metallicity. There may be concern with metallicity effects contributing to errors in an FUV-age relationship, however, Figures

6 and 8 of (Crandall et al. 2020) show no correlations between metallicity and this relationship.

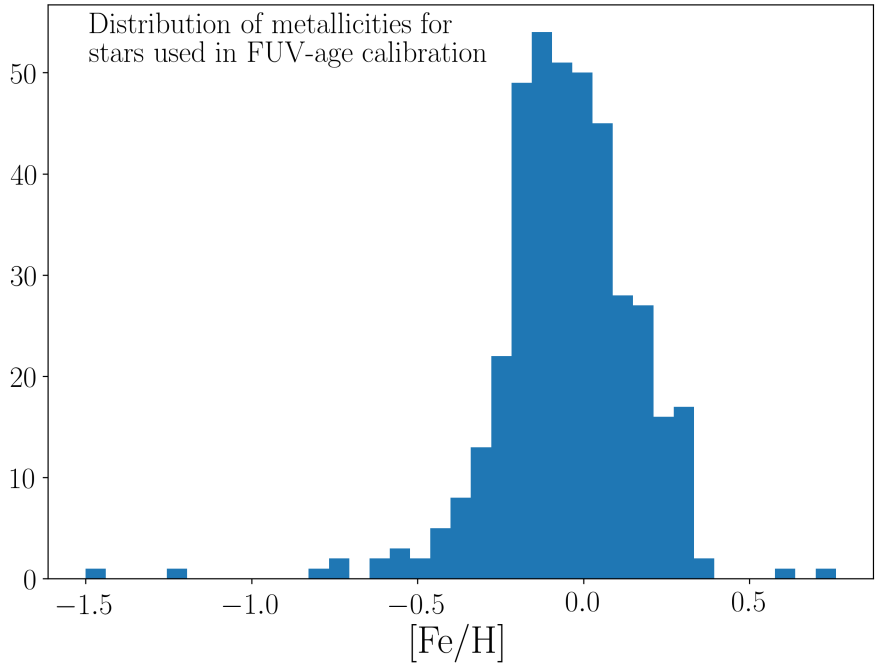

Figure 4.1 A metallicity histogram of 401 stars used in the FUV-age calibration. Of the stars within the sample, 74% or 295 dwarfs, fall within a solar-like metallicity range of $-0.2 \leq$[Fe/H]≤ 0.2.

4.2.2 Constraining the FUV-Age Relation

In a similar manner to Crandall et al. (2020) we define an FUV-excess parameter Q as

$$Q = (FUV - G_{BP}) - u_{\rm FUV}, \tag{4.2}$$

where G_{BP} is the *Gaia* blue magnitude and $u_{\rm FUV}$ is an upper boundary to the value of $(FUV - G_{BP})$ as a function of $(G_{BP} - G)$. This boundary, which is shown in Figure 4.2, represents a minimum chromospheric activity level against which to define an FUV

excess, i.e., Q is equal to the difference between the observed $(FUV - G_{BP})$ color and the boundary value at the relevant stellar $(G_{BP} - G)$.

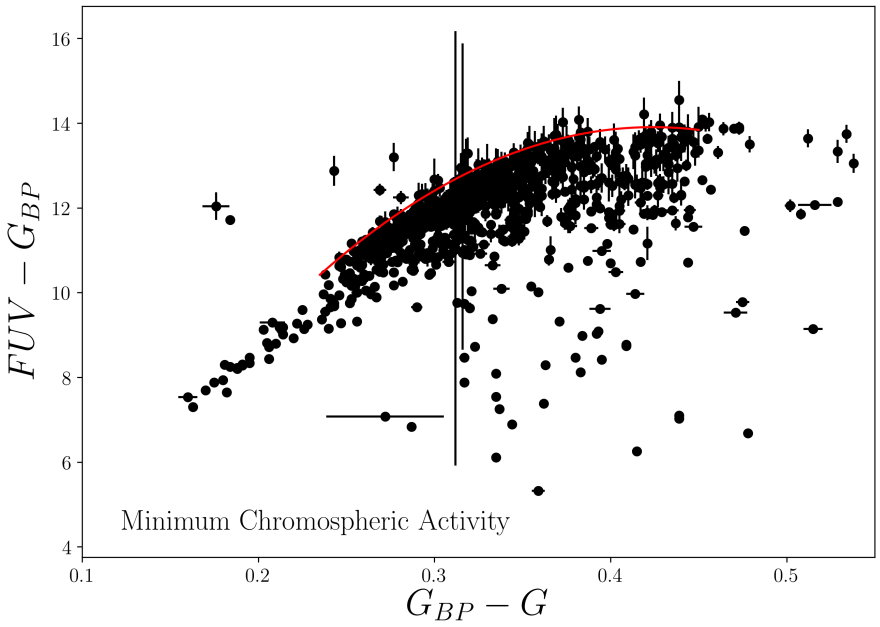

Figure 4.2 A FUV-optical two-color diagram of FGK stars from Isaacson & Fischer (2010); Ballering et al. (2013); Sierchio et al. (2014); Lorenzo-Oliveira et al. (2018) with *GALEX FUV* and *Gaia* magnitudes. Within the color range $0.27 \leq (G_{BP} - G) \leq 0.43$ there is a range of $(FUV - G_{BP})$ colors indicating a range of chromospheric activity levels at any given optical color.

Figure 4.2 is a two-color diagram of $(FUV - G_{BP})$ versus $(G_{BP} - G)$ for all FGK stars in our sample with optical colors of $0.10 \leq (G_{BP} - G) \leq 0.55$. The few dwarfs outside of this range are very scattered in their two-color relationship and are not included in Figure 4.2. A minimum chromospheric boundary, the $u_{\rm FUV}$ referred to above, is clearly defined in the figure and was fit by the red line therein, which has the equation

$$u_{\rm FUV} = -97.38(G_{BP} - G)^2 + 82.61(G_{BP} - G) - 3.61. \tag{4.3}$$

Figure 4.2 also reveals significant spread in values of $(FUV - G_{BP})$ at a given optical color within the range $0.27 < (G_{BP} - G) < 0.43$. Such varied $(FUV - G_{BP})$ behavior demonstrates a range of FUV chromospheric activity levels among FGK dwarfs at a given $(G_{BP} - G)$.

To constrain the FUV-age relationship with *Gaia* colors, we plot literature-reported ages from the four samples listed in Section 4.2.1 against the Q values for each star. As shown in Figure 4.2 this relationship is dependent on $(G_{BP} - G)$, and so we plot τ against Q in color bins. The defined eight bins of width 0.5 range between $0.27 \leq (G_{BP} - G) \leq 0.40$, e.g., bin 1 is $0.27 \leq (G_{BP} - G) < 0.32$, bin 2 is $0.28 \leq (G_{BP} - G) < 0.33$, etc. Figure 4.3 shows four bins as examples. There is a flattening of the relationship for more positive Q values, corresponding to less active stars. The slope changes with each $(G_{BP} - G)$ bin from anywhere between $Q = -0.51$ to $Q = -0.40$. For each bin we then only fit up to the point of flattening, which we call Q_{max}. These values are listed in Table 4.1.

Duplicate stars from the four samples (Lorenzo-Oliveira et al. 2018; Sierchio et al. 2014; Ballering et al. 2013; Isaacson & Fischer 2010) were treated separately in constraining the FUV-age relationship. That is, no ages were combined in the form of an average or the like. Ages were not combined because the methodologies in deriving ages within the four samples differed significantly enough [11] that we could not reasonably compare them.

Table 4.1 displays each bin with its corresponding color range, average color, number of stars in each bin (N), Q_{max}, linear fit parameters a and b, Spearman's

[11] with the exception of Ballering et al. (2013) and Sierchio et al. (2014)

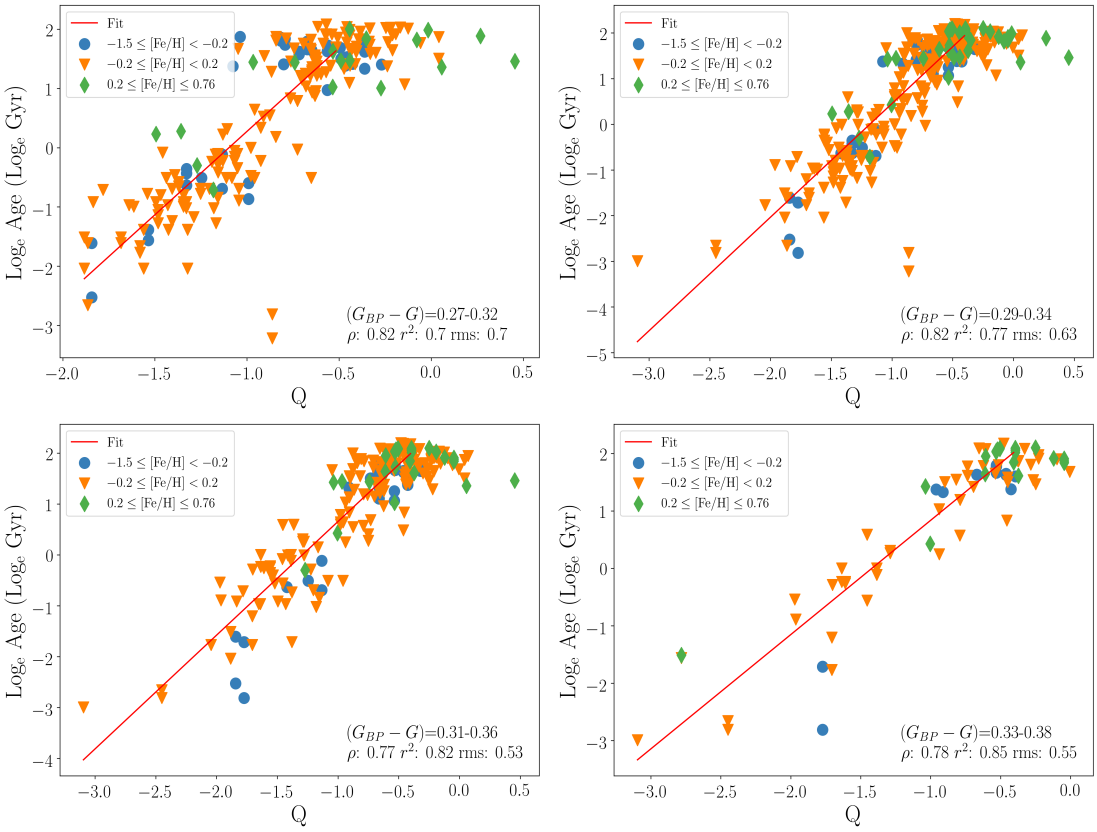

Figure 4.3 Literature-reported ages, $\mathrm{Log_e}(\tau)$, versus FUV-excess parameter Q. Dwarf stars were divided into *Gaia* $(G_{BP} - G)$ color bins. Four of the eight bins which were constrained are shown as examples. The Spearman's correlation coefficient, ρ, coefficient of determination, r^2, and RMS about τ for each fit are displayed. The calibration stars were binned into three metallicity ranges: $-1.5 \leq$[Fe/H]< -0.2 (blue circles), $-0.2 \leq$[Fe/H]< 0.2 (orange triangles), and $0.2 \leq$[Fe/H]≤ 0.76 (green diamonds).

correlation coefficient (ρ), coefficient of determination (r^2), and RMS of fit about age. We found reasonably high ρ and r^2 values for each fit and conclude that the FUV-age relationship is well fit with the linear function Equation 4.1.

Figure 4.3 also shows the metallicity, [Fe/H], values for each dwarf star used in the FUV-age calibration. As described above, theses metallicity values were taken from Casagrande et al. (2011) and fall within a range of $-1.5 \leq$[Fe/H]≤ 0.76. The calibration stars were binned into three metallicity ranges and are shown in Figure

Table 4.1 Age Calibration Fits for FUV-Excess Parameter Q

Bin	$(G_{BP}-G)$ Range	$\langle G_{BP}-G\rangle$[a]	a	b	N[b]	${Q_{max}}$[c]	ρ[d]	r^2[e]	RMS[f]
1	0.27-0.32	0.30	21.97	2.82	238	-0.51	0.82	0.70	0.70
2	0.28-0.33	0.31	19.53	2.61	296	-0.40	0.82	0.75	0.63
3	0.29-0.34	0.32	18.91	2.49	321	-0.40	0.82	0.77	0.63
4	0.3-0.35	0.32	17.70	2.33	293	-0.40	0.80	0.75	0.65
5	0.31-0.36	0.33	18.0	2.24	229	-0.40	0.77	0.82	0.53
6	0.32-0.37	0.33	16.18	2.04	158	-0.40	0.80	0.83	0.53
7	0.33-0.38	0.34	16.89	1.99	89	-0.40	0.78	0.85	0.55
8	0.34-0.39	0.35	15.26	1.68	29	-0.46	0.84	0.90	0.35

[a] Average $(G_{BP}-G)$ color.
[b] Number of stars within each bin.
[c] Q value at which the relationship flattens and we stop the fit
[d] Spearman coefficient
[e] Coefficient of determination
[f] RMS of $\log(\tau)$ about each fit.

4.3: $-1.5 \leq$[Fe/H]< -0.2 (blue circles), $-0.2 \leq$[Fe/H]< 0.2 (orange triangles), and $0.2 \leq$[Fe/H]≤ 0.76 (green diamonds). In general, we do not see a clear correlation between metallicity and the FUV-excess parameter Q. That is, for the bins of $-1.5 \leq$[Fe/H]$<$ -0.2 (blue circles) and $-0.2 \leq$[Fe/H]< 0.2 (orange triangles) we see a variety of activity levels as indicated by Q for any given metallcity. However, in the more metal rich population, $0.2 \leq$[Fe/H]≤ 0.76 (green diamonds) we see a shift towards more active stars or more positive Q values. A more positive Q star would correlate with a less active, old star. These stars are most often found to be metal-poor, and as such this population requires further investigation.

We investigated the apparent trend of metal-rich stars by plotting age, τ, against metallicity [Fe/H] for the calibration sample. Figure 4.4 shows this plots. We do not see a major difference in age ranges for the three metallicity bins. The range of

age for the metal-rich bin is $0.22 \leq \tau \leq 8.17$. As such, we do not anticipate metallicity to impact the validity of the FUV-age relation for the metal-rich stars. We also note that Figure 4.4 shows that the most metal-rich star within the range $-1.5 \leq$[Fe/H]< -0.2 has an age comparable to the Sun. This is consistent with the expectation that metal rich stars are quite young.

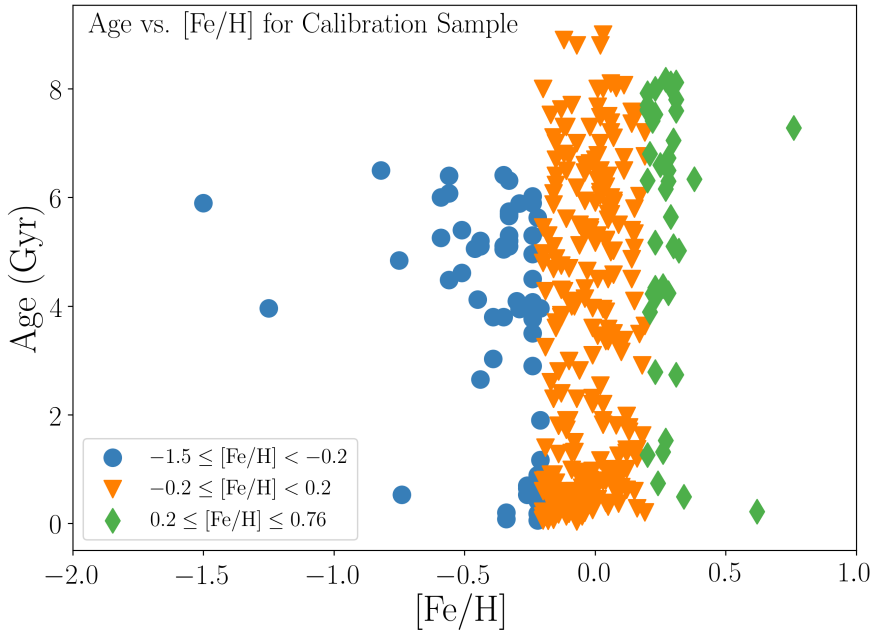

Figure 4.4 $\log_e(\tau)$ versus [Fe/H] for the calibration sample. Metallicities were pulled from Casagrande et al. (2011).

In the final step of the FUV-age calibration process we fit the parameters $\log_e(a)$ and b as functions of $(G_{BP} - G)$ color bins. This illuminates how the fit parameters in Table 4.1 vary with *Gaia* color. Figure 4.5 shows $\log_e(a)$ and b parameters versus $(G_{BP} - G)$, where representative colors are the median $(G_{BP} - G)$ within each bin from Table 4.1. The parameter $\log_e(a)$ is fit with the linear function

$$log_e(a) = -4.44(G_{BP} - G) + 4.35, \tag{4.4}$$

and the parameter b is fit by the linear function

$$b = -14.84(G_{\rm BP} - G) + 7.17. \tag{4.5}$$

Errors shown in Figure 4.5 are the sum of the square of residuals about $\log_e(a)$ and b. With Equations 4.1 - 4.5 one can empirically estimate the age of an FGK type, solar-like star. Alternatively, one may interpolate a grid of a and b values given in Table 4.1.

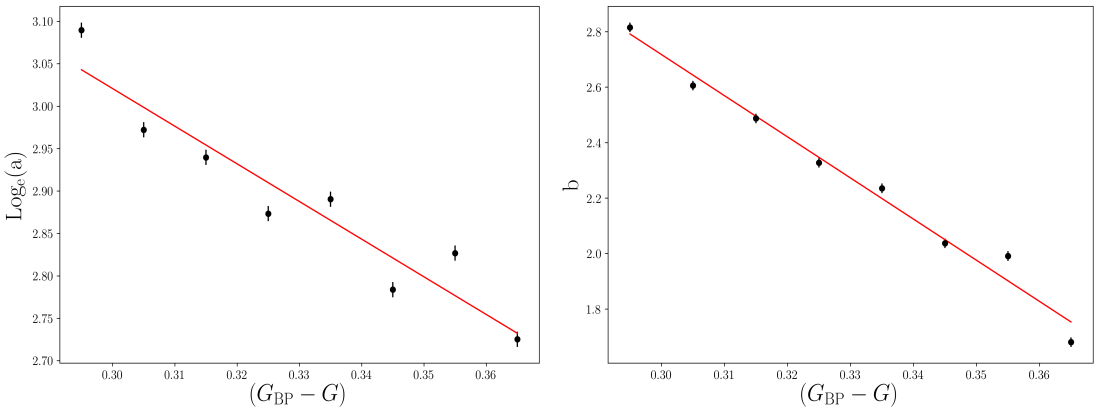

Figure 4.5 Fit parameters $\log_e(a)$ and b from Table 4.1 versus representative $(G_{\rm BP} - G)$ colors. Representative colors were the median $(G_{\rm BP} - G)$ within each bin from Table 4.1. The red lines represent linear fits to parameters $\log_e(a)$ and b. Errors shown are the sum of the square of residuals about $\log_e(a)$ and b.

4.2.3 Related Errors

The reader likely notes the lack of errors in Figure 4.3. Several factors could contribute to an error in the fits given in this figure and Table 4.1, including errors in age determinations, metallicity effects, and errors in the *FUV* observations. The four sources from which ages were pulled (Lorenzo-Oliveira et al. 2018; Sierchio et al. 2014; Ballering et al. 2013; Isaacson & Fischer 2010) did not have associated errors

quoted. As such, we did not include errors for $\log_e(\tau)$. Crandall et al. (2020) explored the possibility of metallciity effects in the FUV-age relation and found no correlations [12]. The extent to which *GALEX* GR6/7 FUV magnitude observations were quantified in Section 3.3 of Crandall et al. (2020). They concluded that for a solar-type G dwarf there would be an error of $\sim$ 1.0 Gyr in an FUV-derived age of 6.0 Gyr, assuming an observational error of 0.05 mag.

We performed a similar analysis in which we assumed a *GALEX* systematic error of 0.02 and 0.05 mag. For a theoretical star with solar color of $(G_{\rm BP} - G) = 0.33$ (Casagrande & VandenBerg 2018), we found an associated error in age using Equations 4.1 - 4.5. Figure 4.6 shows this plot. Here the green dashed line demonstrates a 1:1 exact match in age, while the blue and orange lines give an error in age for theoretical *GALEX* FUV systematic errors of $\pm$0.02 and $\pm$0.05, respectively. From Figure 4.6 we can conclude that for a 6 Gyr star, a systematic FUV error would translate to an age estimate error of $\sim$ 1 Gyr.[13] As such, like with Crandall et al. (2020), we have limited our calibration to stellar ages up to 6 Gyr.

[12] However, they note that this is likely the case due to the metallicity restriction of their stellar sample to have near-solar abundances. This work also imposes a similar restriction.

[13] as in Crandall et al. (2020)

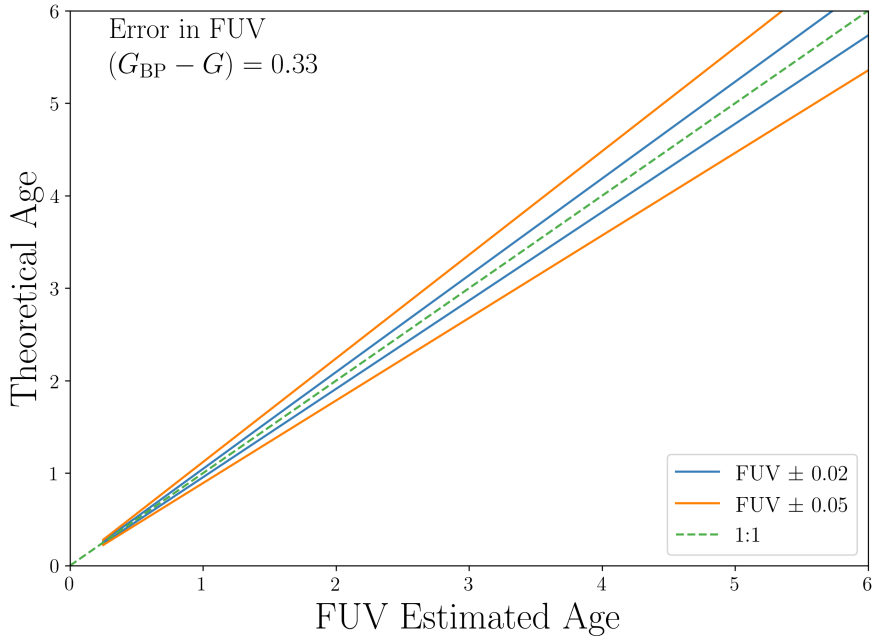

Figure 4.6 Estimated errors of *FUV*-determined ages for a theoretical star with a solar Gaia color $(G_{BP} - G) = 0.33$. The green dashed line demonstrates a 1:1 exact match in age, while the blue and orange lines give an error in age for theoretical *GALEX FUV* systematic errors of ± 0.02 and ± 0.05, respectively.

4.3 The Age-Velocity Relation

FUV-based ages for FGK dwarf stars can be combined with measurements of their space motions, and applied to a study of correlations between age and kinematics of stars in local regions of the Galaxy. As noted in Section 1, the age-velocity relation (AVR) is a general trend which shows that velocity dispersion increases as a function of stellar age within the solar neighborhood. More often than not, an AVR is constructed using isochrone-determined ages. In this section we utilize the Casagrande et al. (2011) sample of thousands of Geneva-Copenhagen Survey dwarf stars to construct an AVR with empirical *FUV*-determined ages.

4.3.1 The Stellar Sample

The basis for the stellar sample which we use to construct an AVR is the Casagrande et al. (2011) collection of solar neighborhood dwarf stars. Casagrande et al. (2011) reanalyzed the Geneva-Copenhagen Survey with new effective temperatures and metallicities (Nordström et al. 2004b), which were then used to estimate the ages of FGK type stars with the BASTI (Pietrinferni et al. 2004, 2006, 2009) and Padova (Bertelli et al. 2008, 2009) isochrone models.

The above sample was comprised of 12,329 dwarf stars. We then discarded stars that do not have *GALEX FUV* or Gaia G and G_{BP} magnitudes. Additionally, stars without Gaia parallax measurements were omitted, as this information is used to make an absolute magnitude cut on the sample. The FUV-age calibration in Section 4.2 is only valid for stars with absolute magnitudes $4.3 \leq M_{\rm V} \leq 5.3$. As such, we did not include stars outside of this solar-analog range. Absolute visual magnitudes for each star were determined by

$$M_{\rm V} = V + 5.0(1.0 + \log_{10} p), \tag{4.6}$$

where V is the Johnson magnitude and p is the parallax in arc sec. The FUV-age calibration is also restricted by the Johnson color range $0.55 \leq (B - V) \leq 0.71$ and *Gaia* color range $0.24 \leq (G - G_{BP}) \leq 0.39$, and stars outside of these ranges were not included in the sample. The final magnitude and color-cut sample contained 660 dwarf stars.

4.3.2 An AVR with Literature-Reported Ages

We first constructed a baseline AVR, Figure 4.7, with the Casagrande et al. (2011) sample without performing any of the color, magnitude or metallicity cuts mentioned above. The ages in this figure are determined by Casagrande et al. (2011) with Padova isochrones in which a probability distribution was constructed using a Bayesian framework and a median value is the final derived age (see Appendix A of Casagrande et al. 2011).

Each of the three velocity dispersions were constructed from the 3D velocity components UVW, which were also quoted in Casagrande et al. (2011) and denoted in the Geneva-Copenhagen Survey (Nordström et al. 2004b). To determine the velocity dispersion in a given axis we first binned the 12,329 stars by age in bin width of 0.5 Gyr from 0-10 Gyr. We then utilized the median absolute deviation (MAD) to determine dispersions σ_U, σ_V, and σ_W. For example,

$$\sigma_U = \text{median}|U_i - \tilde{U}| \tag{4.7}$$

where U_i is a given star's U velocity and $\tilde{U}$ is the median velocity for a given bin. We also determined the MAD age (τ) for a given bin by

$$\text{MAD}(\tau) = \text{median}|\tau_i - \tilde{\tau}|. \tag{4.8}$$

The first three panels in Figure 4.7 show the MAD velocity dispersions for the three kinematic components. We also constructed a final AVR represented by a dispersion

which we denote s. This dispersion is a quadrature sum of the U, V, and W velocity dispersions:

$$s = \sqrt{\sigma_U^2 + \sigma_V^2 + \sigma_W^2}. \tag{4.9}$$

The MAD(τ) and s values are shown in the bottom right panel of Figure 4.7. Again, this AVR represents the constructed Casagrande et al. (2011) relation using their data without color, magnitude, or metallicity cuts made to the sample. The shape of this AVR is comparable to that of Figure 17 in Casagrande et al. (2011). Errors are not shown in Figure 4.7 as UVW velocity errors are not given in the Casagrande et al. (2011) sample.

Traditionally, an AVR is fit with a power law function and we have done so in each panel in Figure 4.7, represented by the red curve. The best-fit power laws are

$$\sigma_U = 15.75\tau^{0.27}, \tag{4.10}$$

$$\sigma_V = 7.87\tau^{0.42}, \tag{4.11}$$

$$\sigma_W = 6.33\tau^{0.36}, \tag{4.12}$$

and

$$s = 18.66\tau^{0.32} \tag{4.13}$$

where τ is the Padova isochrone-determined age in Gyr. The root-mean-square (RMS) residuals about the velocity dispersion fits are 1.52, 1.15, 1.00, and 1.37 km s^{-1} for σ_U, σ_V, σ_W, and s, respectively. These fits are noted in Table 4.2.

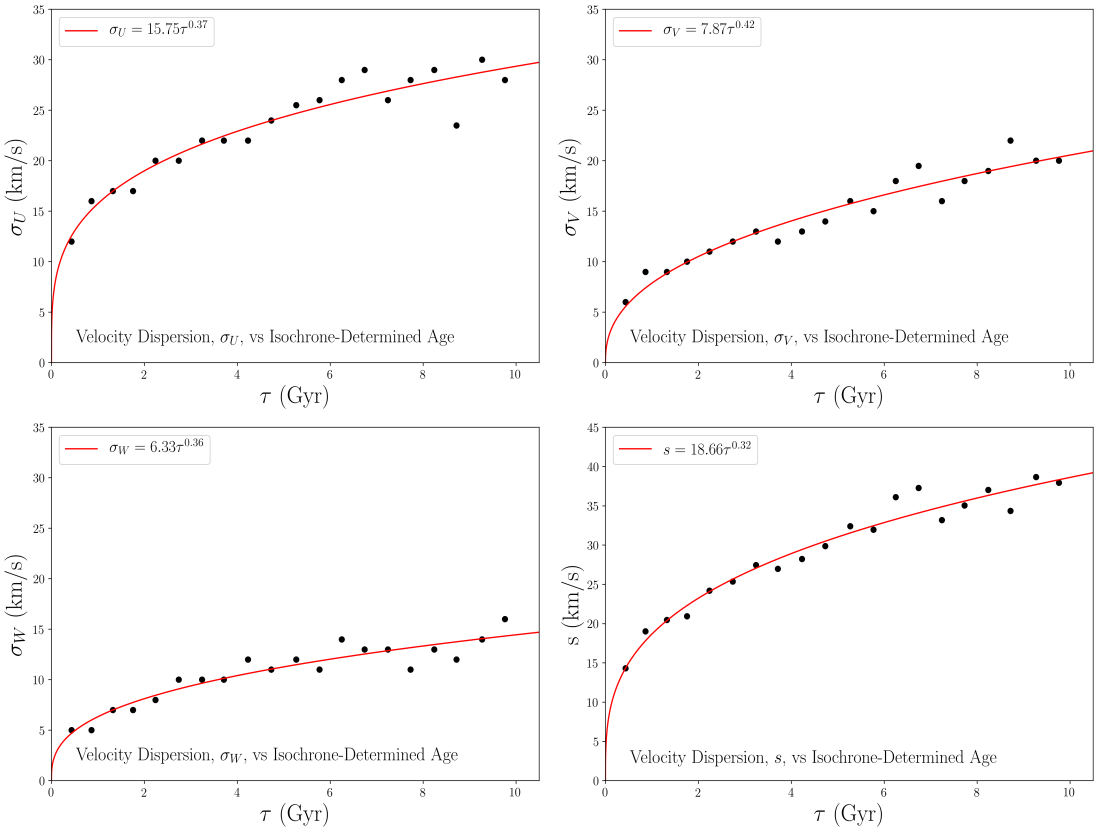

Figure 4.7 Age versus velocity dispersion plots derived using data from the Casagrande et al. (2011) sample of 12,329 dwarf stars. No metallicity, color, or magnitude cuts were made to this sample. Velocity dispersions for UVW were determined using the median absolute deviation, and ages were determined with Padova isochrones. The combined velocity dispersion, s, is the quadrature sum of the UVW velocity dispersions. Each relation is fit by a power law function (red).

4.3.3 An AVR with FUV-Determined Ages

The stellar age-dating tool developed in Section 4.2, in which we calibrated a relationship between *GALEX* FUV magnitudes and age, is useful because it is a purely empirical relationship. One need not rely on stellar models with varying accuracies and user inputs to age-date a star. Hence, this tool uniquely compliments other age-dating techniques based on isochrones.

Table 4.2 Power Law Fits to Age *vs.* Velocity Dispersion Relations

Age Determination[a]	Velocity Determination[b]	Velocity Dispersion	β[c] km/s	RMS[d]
Isochrone	GCS	σ_U	0.27	1.52
Isochrone	GCS	σ_V	0.42	1.15
Isochrone	GCS	σ_W	0.36	1.00
Isochrone	GCS	s	0.32	1.37
FUV	GCS	σ_U	0.21	3.16
FUV	GCS	σ_V	0.24	3.12
FUV	GCS	σ_W	0.34	2.41
FUV	GCS	s	0.24	2.10
Isochrone	*Gaia*	σ_U	0.28	1.76
Isochrone	*Gaia*	σ_V	0.44	1.91
Isochrone	*Gaia*	σ_W	0.42	0.80
Isochrone	*Gaia*	s	0.34	1.65
FUV	*Gaia*	σ_U	0.21	2.82
FUV	Gaia	σ_V	0.29	3.02
FUV	*Gaia*	σ_W	0.31	2.75
FUV	*Gaia*	s	0.21	2.47

[a]The method used to determine ages. Isochrone ages are quoted in Casagrande et al. (2011) and *FUV* ages are estimated using the calibration in Section 4.2.

[b]GCS velocities quoted in Casagrande et al. (2011) are taken from the Geneva-Copenhagen Survey, while *Gaia* velocities were determined here from *Gaia* proper motions, parallaxes, and radial velocities.

[c]Power law fit parameter β

[d]RMS about the velocity dispersion fit

We have taken the compilation of Casagrande et al. (2011) dwarf stars with the absolute magnitude and color cuts described in Section 4.3.1 and estimated their ages with *GALEX FUV* observations. Equations 4.1 - 4.5 were used to determine the *FUV* age, τ, for each of the 660 stars in the sample.

The stars were then binned by age in order to determine a MAD representative value. However, in this case, the sample was reduced from the original 12,329 Casagrande et al. (2011) stars to 660 after color and magnitude cuts. As such, there

were significantly fewer stars older than $\sim$ 4 Gyr. We accounted for this by binning with varying bin widths. Velocity dispersions σ_U, σ_V, σ_W, and s were then calculated in the same manner as the full Casagrande et al. (2011) sample using the MAD for both velocity and age.

Figure 4.8 shows all four velocity dispersions when utilizing *FUV*-determined ages. We note more scatter for stars older than $\sim$ 4 Gyr. Additionally, the velocity dispersion in the V and W directions are flatter and have a smaller dispersion range. We also note that the *FUV*-age relationship is best for stars younger than $\sim$ 6 Gyr, as an estimated associated *FUV* error is 1 Gyr for a 6 Gyr old star. Each dispersion was fit with a power law function:

$$\sigma_U = 16.44\tau^{0.21}, \tag{4.14}$$

$$\sigma_V = 10.94\tau^{0.24}, \tag{4.15}$$

$$\sigma_W = 7.10\tau^{0.34}, \tag{4.16}$$

and

$$s = 21.28\tau^{0.24} \tag{4.17}$$

where τ is the *GALEX* *FUV*-determined age. The RMS values about the velocity dispersions are 3.16, 3.12, 2.41, and 2.10 for σ_U, σ_V, σ_W, and s, respectively. Power law fit parameters for these AVRs are listed in Table 4.2.

The power law fit parameter, β, gives insight into the formation history of the Milky Way. As described in Ting & Rix (2019), most studies agree that the velocity dispersion towards the North Galactic pole, σ_W, fit with a power law results in a pa-

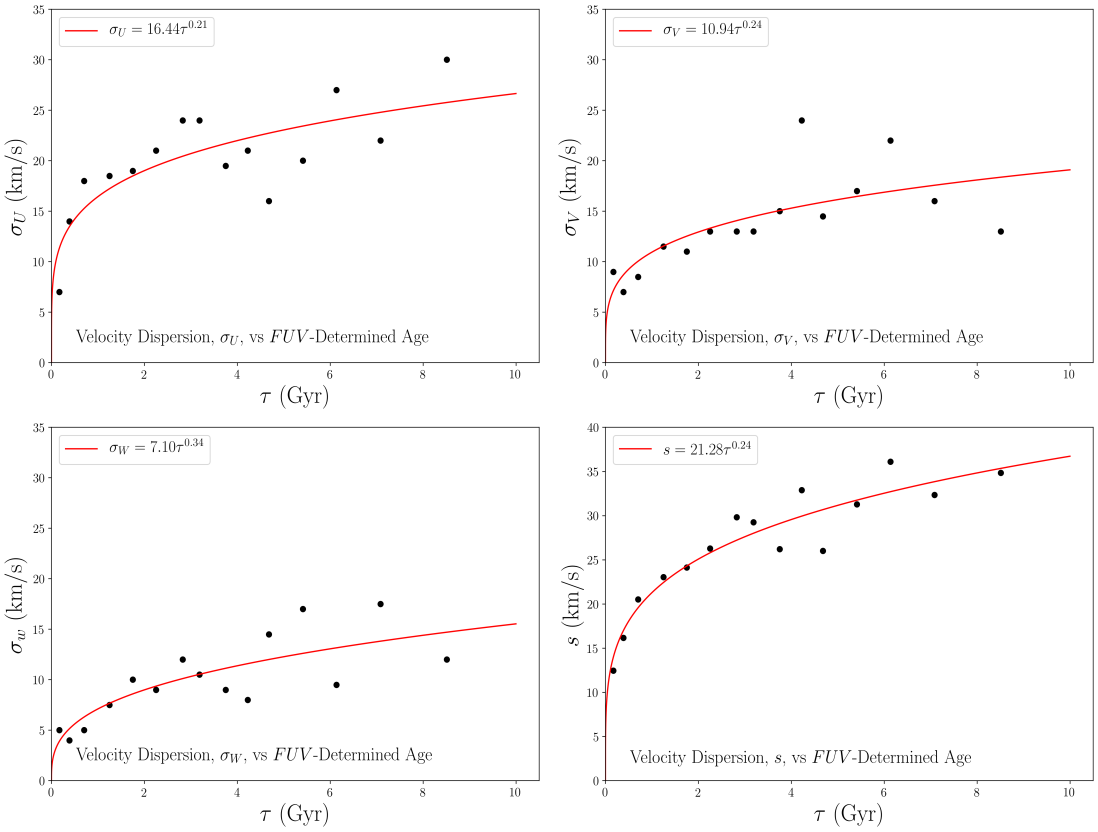

Figure 4.8 Age-velocity relation plots for the Casagrande et al. (2011) sample with magnitude and color-cuts (660 stars) and FUV-determined ages. Velocity dispersions for UVW were determined using the median absolute deviation. The combined velocity dispersion, s, is the quadrature sum of the UVW velocity dispersions. The relation is fit by a power law function (red).

rameter $\beta \sim 0.5$. Our fits to an AVR in this direction vary between $0.31 \leq \beta \leq 0.42$, which is not quite in agreement with the majority of sources. However, simple simulations of an AVR created solely by heating due to Giant Molecular Clouds (GMC) have resulted in a fit parameter of $\beta \sim 0.25$ (Hänninen & Flynn 2002; Kokubo & Ida 1992). Indeed, there is no consensus on the shape of the age-velocity relation. In fact, Spitzer & Schwarzchild (1951) who first highlighted such a relation, found their mean velocity dispersion was fit to a function with $\beta = 1/3$. The heating mechanism within their

work was purely from GMC scattering. In our work we created AVRs with Casagrande et al. (2011) isochrone-determined ages, and found a $\beta \sim 1/3$ (see Table 4.2). In another example, Holmberg (2009) simulated AVRs using synthetic Geneva-Copenhagen Survey observations. They show in their Figure 8 (panel a) that if only GMCs or other local heating agents contributed to heating, the AVR would continuously rise in velocity dispersion. Our AVR Figure 4.8, as well as that constructed with Casagrande et al. (2011) velocities and ages (Figure 4.7), show a flattening of the curve around 2-3 Gyr. Holmberg (2009) further demonstrates in panels c and d of the same figure, that a minor merger occurring at the 3 Gyr mark would cause such a flattening. To be sure, there are discrepancies in the fit parameters of AVRs constructed by both observations and simulations. One heating mechanism alone may not be enough to describe velocity dispersion observations. There may very well be several mechanisms which play a role. Furthermore, simulations allow for a broader range of Galactic interaction, while observations are still restricted to near the Solar neighborhood. The constraints of local data in our observations certainly impact our interpretations of the age-velocity relation.

4.3.4 AVR with *Gaia*-Determined Velocities

An obvious additional step in constructing age-velocity relations was to determine the 3D velocities of the Casagrande et al. (2011) sample with Gaia kinematic information. We compiled a sample of Casagrande et al. (2011) stars with RA, DEC, proper motions, radial velocities, and parallax observations from *Gaia*; a total of 11,350 stars. UVW velocities were determined by inputting the *Gaia* kinematics into the PyAstronomy package (Czesla et al. 2019).

The AVR plots with *Gaia*-determined velocity dispersions and isochrone-determined stellar ages are shown in Figure 4.9. As before, the AVRs were fit with a power law function:

$$\sigma_U = 16.23\tau^{0.28}, \tag{4.18}$$

$$\sigma_V = 7.86\tau^{0.44}, \tag{4.19}$$

$$\sigma_W = 6.02\tau^{0.42}, \tag{4.20}$$

and

$$s = 18.91\tau^{0.34} \tag{4.21}$$

where τ is the Padova isochrone-determined age. The RMS values about the velocity dispersions are 1.76, 1.91, 0.80, and 1.65 for σ_U, σ_V, σ_W, and s, respectively. The fits and RMS values are also given in Table 4.2. The RMS about the velocity dispersions are smaller than the fits of the Casagrande et al. (2011) velocity-determined sample. The narrower ranges of velocity dispersions are also evident in Figure 4.9 compared to Figure 4.7.

Finally, we constructed AVR plots using *Gaia*-determined velocities and *FUV*-determined ages. All four velocity dispersions are shown in Figure 4.10 along with the power law fit to each relation. Similar to the AVR in Figure 4.8, this sample only includes stars with *GALEX FUV* magnitudes, colors within $0.55 \leq (B-V) \leq 0.71$ and $0.24 \leq (G - G_{BP}) \leq 0.39$, and absolute magnitudes within $4.3 \leq M_{\rm V} \leq 5.3$; a total of

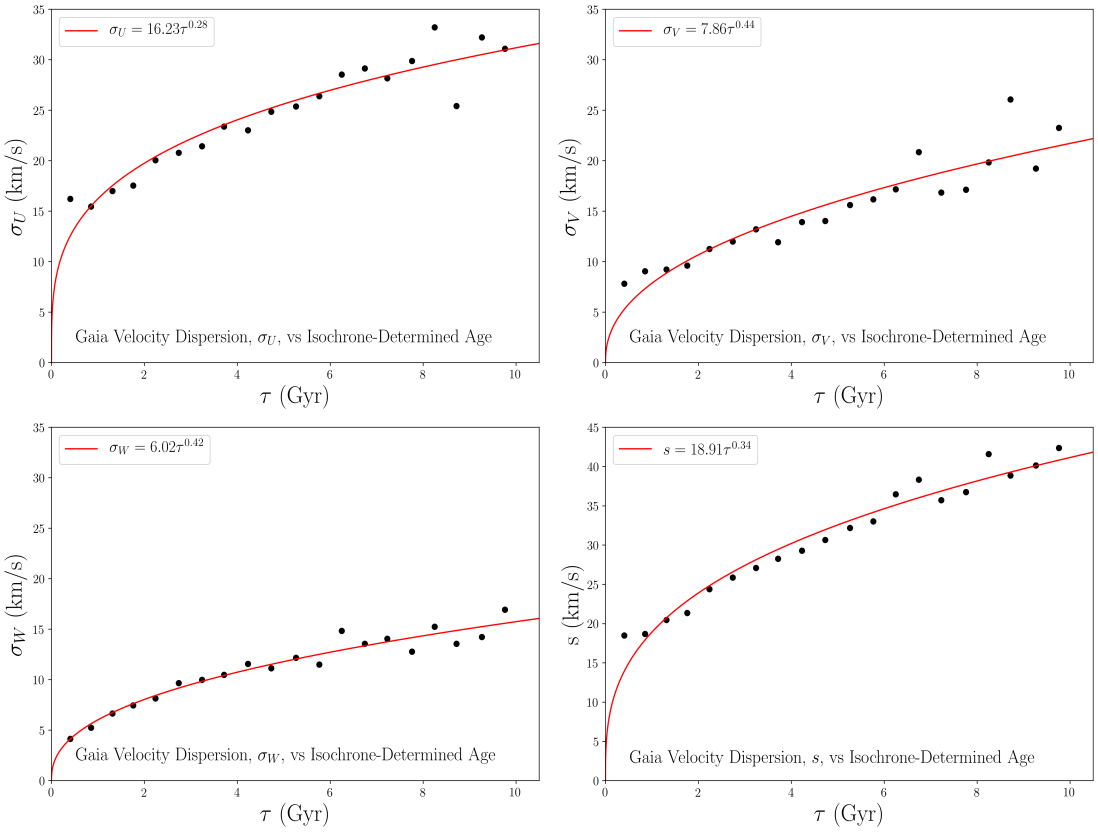

Figure 4.9 Age-velocity relation plots for the Casagrande et al. (2011) sample isochrone-determined ages and *Gaia*-determined velocity dispersions. Velocity dispersions for UVW were determined using the median absolute deviation. The combined velocity dispersion, s, is the quadrature sum of the UVW velocity dispersions. The relation is fit by a power law function (red).

598 stars. Each plot was fit with a power law function:

$$\sigma_U = 15.90\tau^{0.21}, \tag{4.22}$$

$$\sigma_V = 11.64\tau^{0.29}, \tag{4.23}$$

$$\sigma_W = 7.48\tau^{0.31}, \tag{4.24}$$

and

$$s = 21.48\tau^{0.21} \tag{4.25}$$

where τ is the FUV-determined age. The RMS values about the velocity dispersions are 2.82, 3.02, 2.75, and 2.47 for σ_U, σ_V, σ_W, and s, respectively The relations shown in Figure 4.10 are not as clearly defined as in 4.9. This is likely a consequence of a lower number of stars in this sample as compared to that in Figure 4.9. We note that there are no significant differences in power law fits when comparing the Casagrande et al. (2011) and *Gaia* velocities.

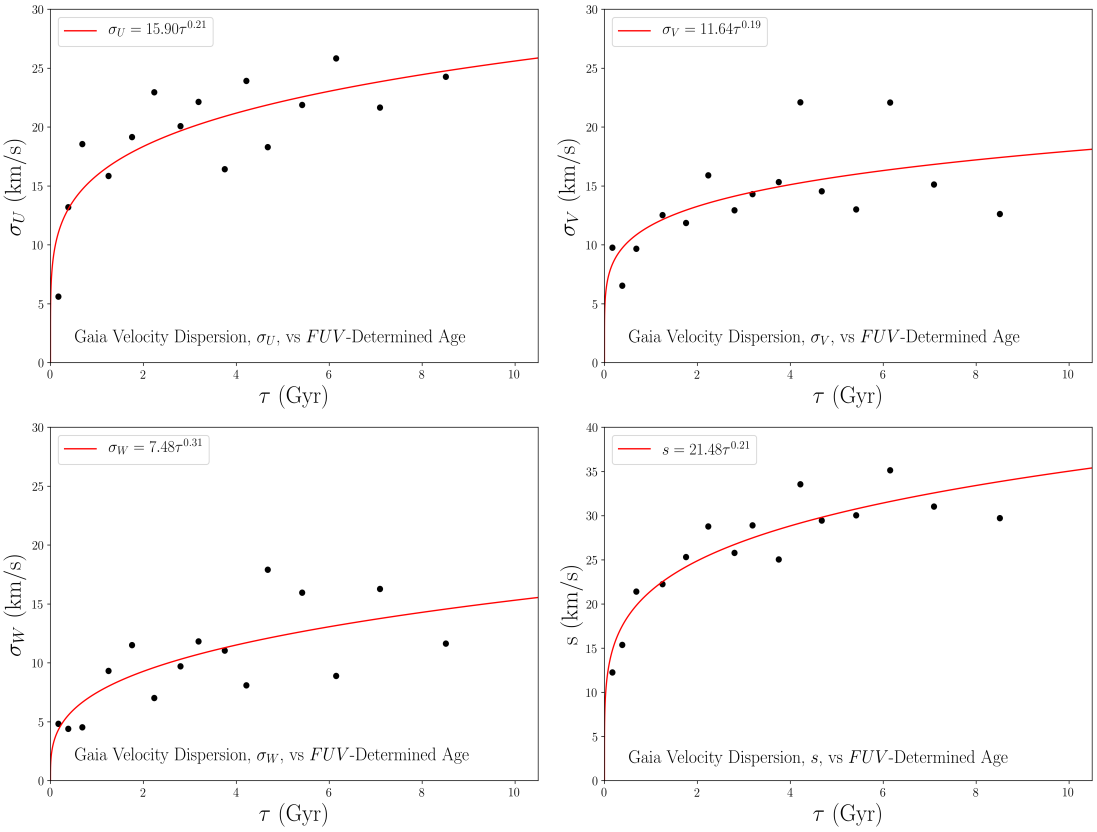

Figure 4.10 Age-velocity relation plots for the Casagrande et al. (2011) sample *FUV*-determined ages and *Gaia*-determined velocity dispersions. Velocity dispersions for UVW were determined using the median absolute deviation. The combined velocity dispersion, s, is the quadrature sum of the UVW velocity dispersions. The relation is fit by a power law function (red).

4.4 Metallicity, Chromospheric Activity, and Age

Similar to the AVR, the age-metallicity relation (AMR) is often used to interpret the formation history of the Milky Way. Twarog (1980a,b) has shown an age-metallicity relationship (AMR) for main sequence stars within the Milky Way which has since been used to test chemical evolution hypotheses (Casagrande et al. 2011; Holmberg et al. 2007; Holmberg 2009). The common consensus of the Milky Way's structure consists of younger stars which reside closer to the Galactic plane and tend to be more

metal rich, while older stars are more vertically dispersed and metal-poor.

We explored a possible AMR for our sample of stars by first investigating the relationship between metallicity and chromospheric activity indicator Q. Metallicity estimates, [Fe/H] and [α/Fe], in this work are from Casagrande et al. (2011) in which a new metallicity scale was derived for the Geneva-Copenhagen Survey sample of solar neighborhood stars. These metallicity estimates are not accompanied with errors within the Casagrande et al. (2011) catalog. We only considered stars from the sample which have *GALEX FUV* observations. In addition, stars were only considered if they fell within *Gaia* color range $0.27 < (G_{BP} - G) < 0.40$, as this range reveals the variance of chromospheric activity within the *FUV* broadband range without significant photospheric contamination. This sub-sample consisted of 4,644 stars. Activity indicator, Q, estimates were derived for each of the stars using Equations 4.2 and 4.3.

Figure 4.11 shows the Casagrande et al. (2011) metallicity [Fe/H] and [α/Fe] versus chromospheric activity indicator Q. We comparedFigure 4.11 to Figure 16 of Casagrande et al. (2011) and noticed a similar trend between our activity-metallicity relationship and their age-metallicity relationship. That is, for stars with metallicity $-0.5 \lesssim [Fe/H] \lesssim 0.5$, there is a wide distribution of both age and activity levels.

We further reduced the GCS stars in Figure 4.11 to only include those with color and magnitudes within the ranges $0.55 \leq (B - V) \leq 0.71$, $4.3 \leq M_{\rm V} \leq 5.3$, and $0.27 < (G_{BP} - G) < 0.40$. The calibration between *FUV* magnitudes and stellar ages is only valid for stars within these ranges. We then determined ages for each star using equations 4.1, 4.4, and 4.5. These ages are shown against metallicity [Fe/H] and [α/Fe]

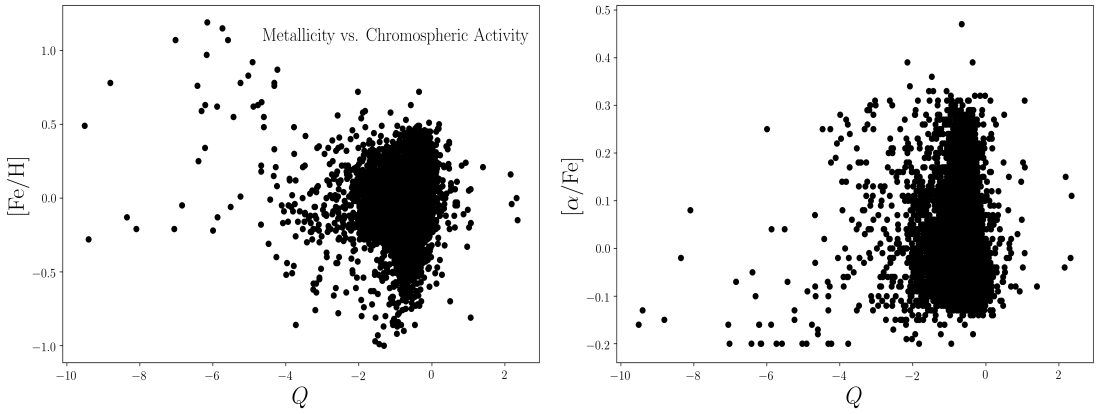

Figure 4.11 Metallicity, [Fe/H] and [α/Fe], from Casagrande et al. (2011) as a function of chromospheric activity indicator Q.

in Figure 4.12. Similar to Figure 16 of Casagrande et al. (2011), there appears to be little to no relationship between metallicity and age in this figure.

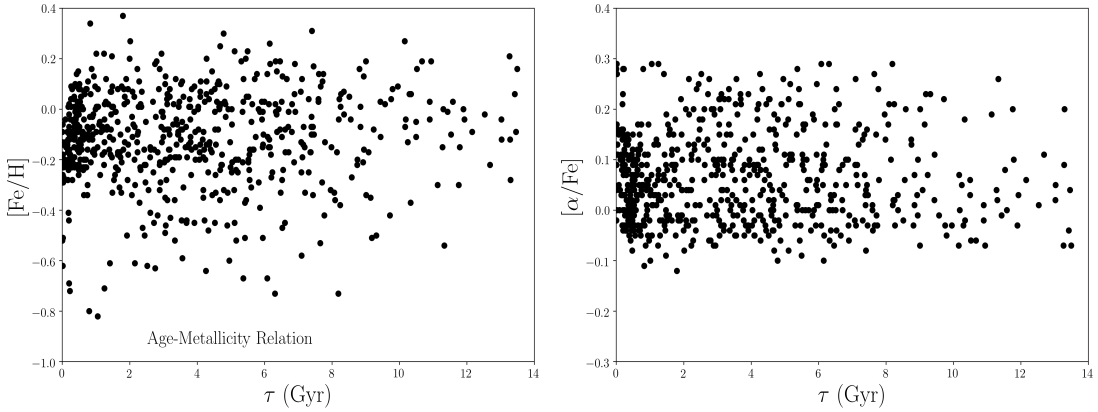

Figure 4.12 Age-metallicity plot with *FUV*-determined ages and metallicities from Casagrande et al. (2011).

In addition to kinematic information, Casagrande et al. (2011) also provide the perigalactic radii ($r_{\rm min}$), apogalactic radii ($r_{\rm max}$), and eccentricity values for their sample. Figure 4.13 shows each of these values as a function of *GALEX FUV*-determined ages. Interestingly, Figure 4.13 suggests that some stars of age $\sim$ 5-8 Gyr have orbits which are significantly different than the Sun's. We further investigated this by examin-

ing the ten stars in the bottom panel of Figure 4.13 which have eccentricity > 0.4. These stars have small $r_{\rm min}$; with a range of $0.63 \leq r_{\rm min} \leq 4.94$. The same stars are shown in red in the top left panel of Figure 4.13. In addition, these ten stars have metallicities smaller than the Sun: $-0.82 \leq$[Fe/H]≤ -0.37. A star with high eccentricity will also have a small perigalactic radius, or more accurately, a large difference between $r_{\rm min}$ and $r_{\rm max}$.

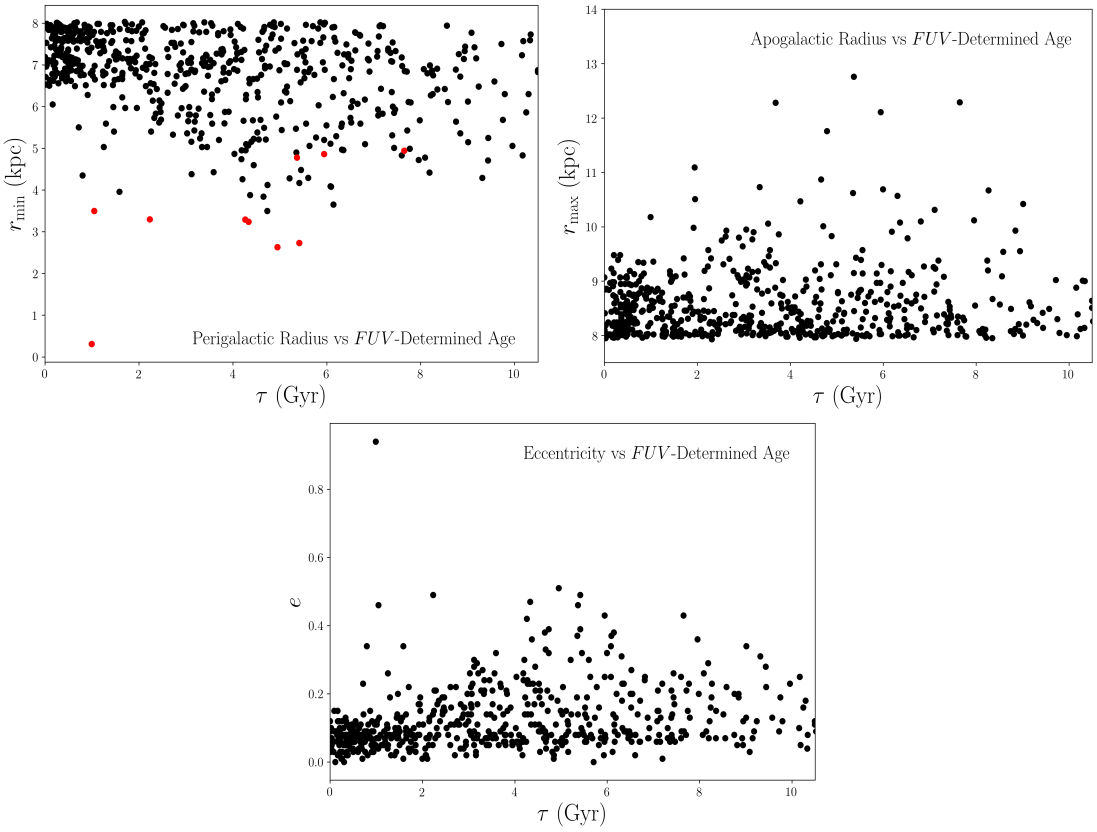

Figure 4.13 Perigalactic radii ($r_{\rm min}$), apogalactic radii ($r_{\rm max}$), and eccentricity given by Casagrande et al. (2011) as a function of FUV-determined ages (τ). Red stars in the top left panel have large eccentricity: $e > 0.4$.

The age-metallicity plots of Figure 4.12 were then recreated with four different populations: two populations segregated at $r_{\rm min} < 6.0$ and $r_{\rm min} \geq 6.0$ (Figure 4.14),

and two populations segregated by eccentricity at $e < 0.4$ and $e \geq 0.4$ (Figure 4.15). We note that these cutoffs are arbitrary and were determined to (1) have enough stars in the outstanding population to base a conclusion on and (2) still isolate the outstanding population. Both Figures show [Fe/H] and [α/Fe] against *FUV*-determined ages. These figures demonstrate that the population of stars with high eccentricity and small perigalactic radii are not young. Very few stars with $r_{\min} < 6.0$ formed in the last couple of billion years.

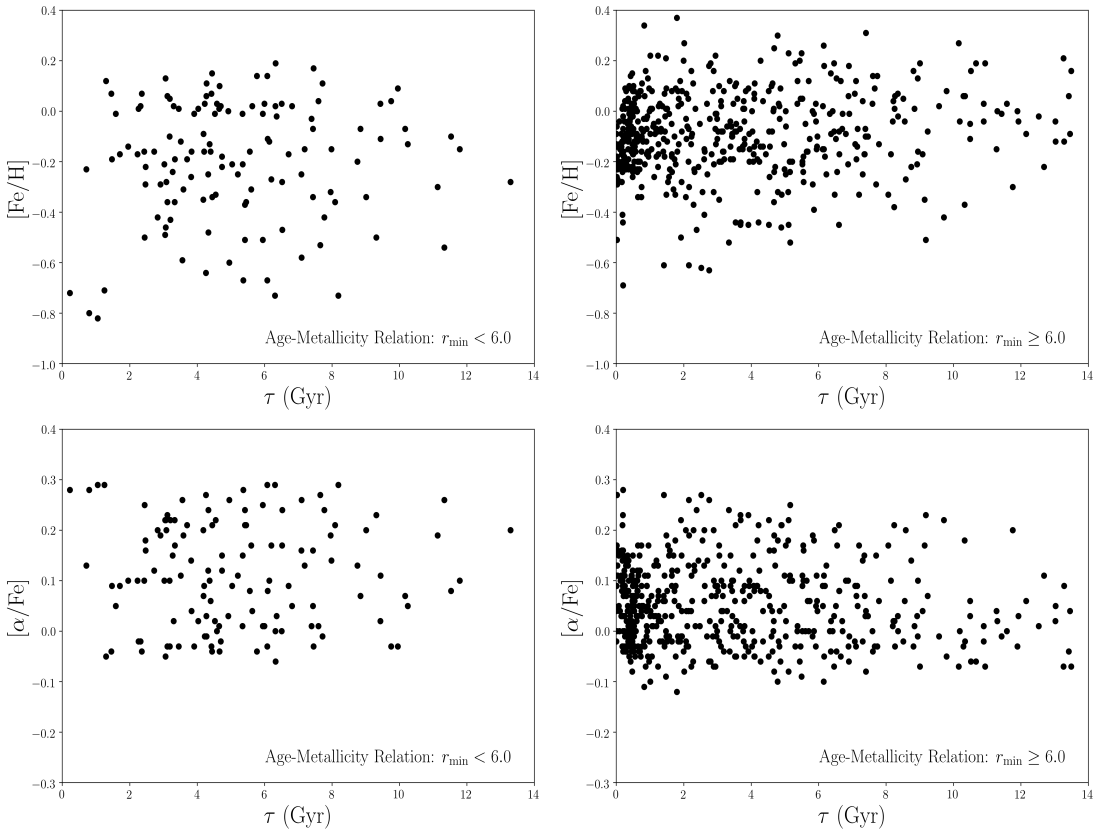

Figure 4.14 Metallicity against *FUV*-determined ages for two populations of stars: $r_{\min} < 6.0$ and $r_{\min} \geq 6.0$.

These fairly old stars with low metallicity, large eccentricity, and small perigalactic radii are consistent with a radial mixing by dynamical heating model. Here,

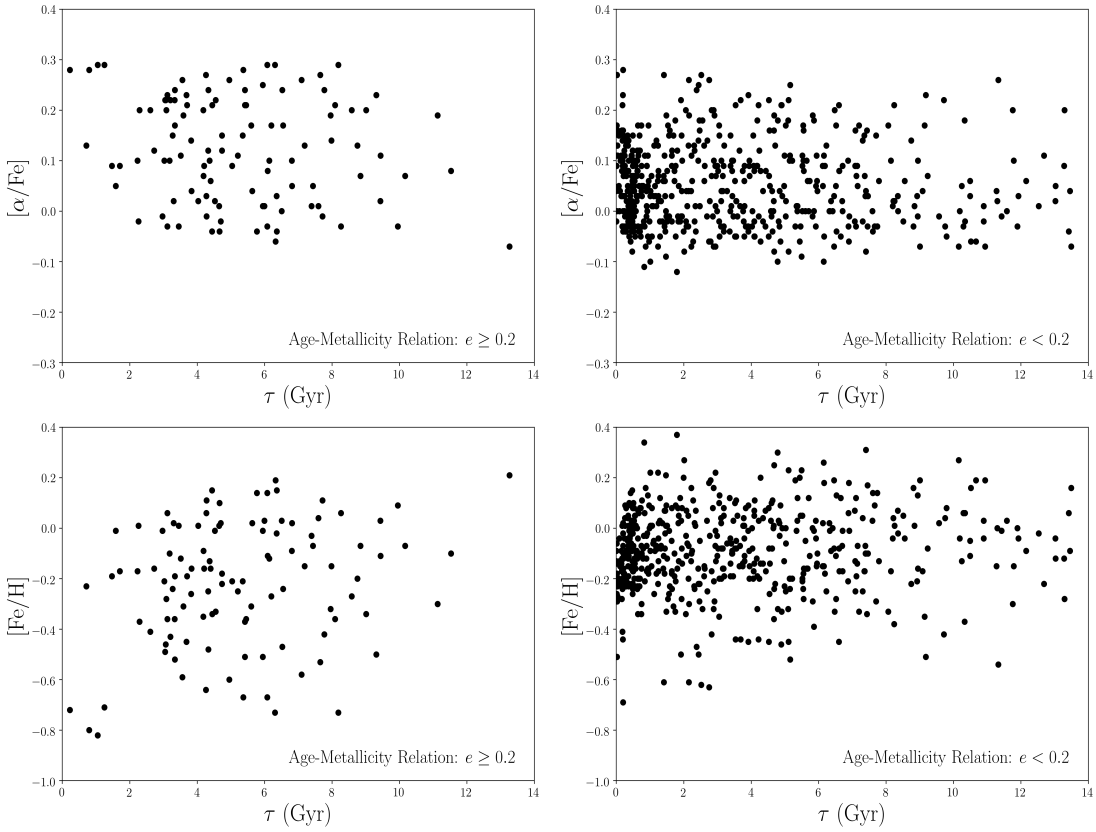

Figure 4.15 Metallicity against FUV-determined ages for two populations of stars: $e < 0.4$ and $e \geq 0.4$.

the inner parts of the Milky Way formed first, and the first formed stars then migrated outward due to dynamical heating. This formation history is commonly called the "inside out" model (Matteucci & Francois 1989). In addition to the above attributes of these old stars, they also have a large range in motion towards the Galactic center, U (see figure 4.16). This again, is consistent with a large velocity dispersion caused by dynamical heating. Radial mixing plays its role here by redistributing stars radially over time (Loebman et al. 2011). That is, older stars are less radially dispersed, and exist at higher vertical scale heights.

A high-resolution hydrodynamic simulation of a Milky Way-like galaxy, Bird

et al. (2013) shows a similar scenario to what we observe here. The simulation within their work uses a fully cosmological environment and tracks age cohorts of stars over the galaxy's formation history. They do note that this method is less comparable to observations which utilize chemical tracers. However, it is a useful comparison for this work due to its simplistic nature in tracking stars based on their ages. Bird et al. (2013) stars formed at redshift > 3 would have been scattered into kinematically hot configurations with thick scale heights and at shorter radial scale lengths. Younger stars are found at larger radii, but exist closer to Galactic plane. Indeed, in this work we observe the Milky Way structure following an "inside out" pattern.

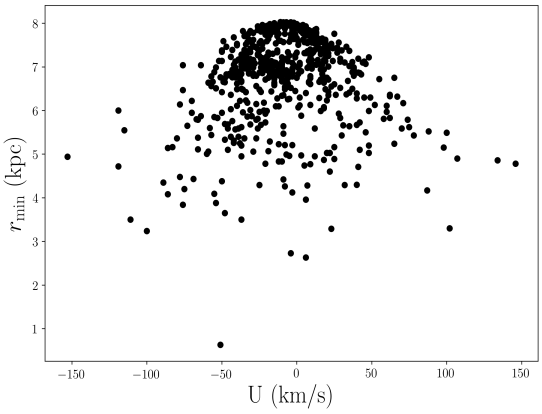

Figure 4.16 Perigalacitc radii versus velocity towards the Galactic center for the set up stars in our cross-matched sample for which we determined *FUV* ages. All values are from Casagrande et al. (2011).

4.4.1 High and Low Alpha Stars

Quite often the population of stars in the Milky Way disk are split into two groups: thin and thick disk constituents. The formation history of these two populations

have been thoroughly speculated.[14] The thick disk may have formed in situ when metal poor stars maintained their scale heights after the surrounding gas collapsed into the Galactic plane (Veltz et al. 2008; Robin et al. 2014; Navarro et al. 2018). Thin disk stars may have then formed later in the collapsed disc. Perhaps a major merger (Veltz et al. 2008), or several mergers (Brook et al. 2004) early on in the Milky Way's formation history formed the thick disk stars via accretion. As suggested in the previous section, our galaxy's structure may have been the result of heating mechanisms which have driven the thick disk outwards ("inside out" formation). As these stars are older, they have had more opportunities to gravitationally interact with Giant Molecular Clouds (Hänninen & Flynn 2002; Aumer et al. 2016), black holes (Lacey & Ostriker 1985; Hänninen & Flynn 2002) and other stars.[15] Many works support the claim that within the varying scenarios of mechanisms which have driven the Milky Way's evolution, the kinematic trends were likely designated at birth (Bird et al. 2013). Regardless of the formation history, the thin and thick disk stars are generally classified by their [Fe/H] abundance, age, or a combination of the two parameters.

However, there is significant, recent interest in a different classification of stellar populations based on [α/Fe] estimates. High alpha and low alpha stars then distinguish the high and low alpha disks, respectively, within the solar neighborhood (Fuhrmann 1998; Prochaska et al. 2000) and extended to Galactic structure studies (Bovy et al. 2012; Haywood et al. 2013; Bovy et al. 2016). It is important to note that Bovy et al. (2012) show a lack of clear correlation between the low and high alpha disks and the

[14] See Bird et al. (2013) for a detailed discussion.

[15] Although the assembled mass from GMCs and black holes contributes to the scattering significantly more than stellar mass.

thin and thick disks. In addition, the distinction between low and high alpha disks appears to be dependent upon Galactocentric radius, where the high alpha population resides closer to the Galactic center and the low alpha population in an annulus further out (Bovy et al. 2016; Haywood et al. 2016; Mackereth et al. 2019).

In the radial mixing model high alpha stars which formed in the inner disk will have a steeper slope in an age-velocity dispersion relation (Schönrich & Binney 2009; Mackereth et al. 2019) It follows that a low alpha population should have a flatter AVR. We have split our stellar sample into low and high alpha populations using a simple cut at $[\alpha/\mathrm{Fe}]= 0.1$, with low alpha stars falling below this threshold and high alpha stars above. We note that this is a bit of an arbitrary and simple distinction. Indeed, a more appropriate designation would include a Galactocentric radius consideration (see e.g., Mackereth et al. 2019). Figure 4.17 shows the AVR for both the low and high alpha samples and FUV-determined ages (τ).[16] The AVRs were fit with a power law function and have the forms

$$s = 17.85\tau^{0.27} \tag{4.26}$$

and

$$s = 15.36\tau^{0.15} \tag{4.27}$$

for the high and low alpha populations, respectively. Here s is the quadrature sum of

[16]Perhaps another instructive pair of AVRs would be constructed by parsing populations by eccentricity. We did attempt to fit two AVRs where the high eccentricity population consisted of stars with $e >= 0.3$ and a low eccentricity population with $e < 0.3$. As noted in the prior subsection, eccentricity also correlates with perigalactic radii, r_{min}, where high eccentricity implies a small r_{min}. However, the sample with high eccentricity is a significantly smaller subsample which contributes to a quite scattered and flat AVR. This is consistent with other observations in this work, as this sub-population does not include younger stars, and so will appear to be flat. The scattered nature of the plot does not allow for a well-fit power law curve.

the three velocity dispersions, σ_U, σ_V, and σ_W. Indeed, we do see a flatter AVR curve for the lower alpha population. The flatter curve indicates a younger, dynamically cool population which has not had as much time or opportunities to heat.

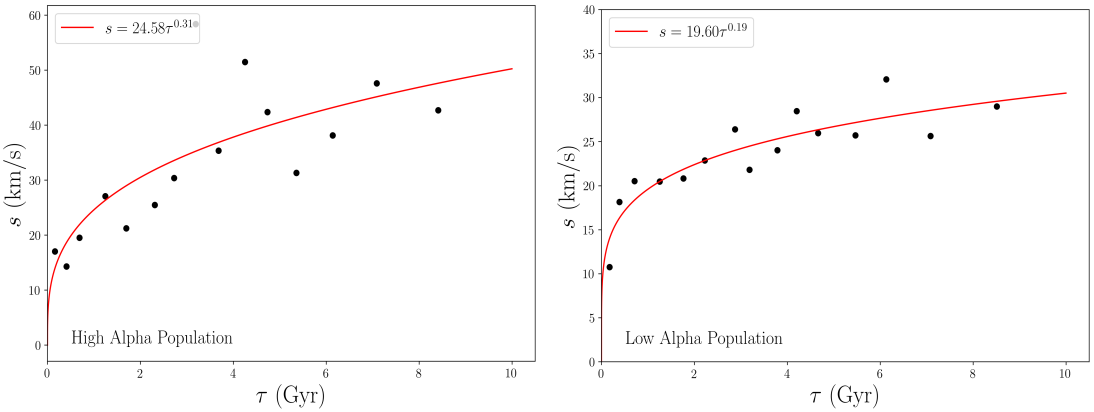

Figure 4.17 AVRs constructed for both the low and high alpha samples, with a designation at below and above $[\alpha/\mathrm{Fe}]= 0.1$, respectively, and FUV-determined ages.

4.5 Conclusion

In this work we have calibrated a relationship between *GALEX* FUV magnitude and stellar age for FGK type stars. This calibration is similar to that given in Crandall et al. (2020), however, in this case one utilizes readily available *Gaia* $(G-G_{\mathrm{BP}})$ colors instead of Johnson $(B-V)$ colors, such that this calibration is more accessible. The empirical relationship described herein allows a user to estimate the age of a Sun-like star with only an FUV magnitude and *Gaia* $(G-G_{\mathrm{BP}})$ color.

Furthermore, we have constructed age-velocity relations for a compiled set of 660 Geneva-Copenhagen Survey stars using FUV-determined ages. We find that the AVRs may be fit with a power law function. The power law parameter β for our AVRs

are consistent with those fit to AVRs constructed by simple simulations of Galactic formation due to Giant Molecular Cloud (GMC) heating with $\beta \sim 0.25$. In addition, perigalactic and eccentricity versus FUV-age plots show that our collection of stars is consistent to an "inside out" model in which older stars are more centrally located with larger eccentricities, while younger stars are found at larger radii and have smaller eccentricities.

Chapter 5

Summary and Future Work

5.1 Summary

This thesis presents and calibrates an empirical relationship between stellar age and *GALEX FUV* magnitudes of FGK dwarfs stars. Furthermore, it explores the validity of such a relationship in giant stars. Chiefly, this thesis uses FUV-determined ages of stars from the Geneva-Copenhagen Survey to interpret the formation and evolution history of the Milky Way.

In Chapter 2 the FUV-excess parameter, Q, shows promise as an age indicator for late-F, G, K type dwarf stars. Like previous works on the use of coronal and chromospheric emission observations, this indicator shows a relationship between stellar activity and age of dwarf stars. This chapter formulated a calibration which demonstrates *GALEX FUV* photometry as a stellar activity indicator for age-dating purposes.

Within Chapter 3, I examined correlations between four chromospheric and

coronal activity indicators. There is an evident correlation between $\log(L_{\rm X}/L_{\rm bol}) > -6.0$ and $\log(F_{\rm MgII}/F_{\rm bol}) < -4.8$, where $L_{\rm X}$ is the X-ray luminosity from *ROSAT* observations (a coronal activity indicator), and $F_{\rm MgII}$ is the flux from Mg II h and k emission lines (a chromospheric activity indicator). I found a varied range of *FUV* emission for core-helium burning stars (CHeB) indicating that giants in this phase may be receiving a magnetic field strength "boost."

Finally, in Chapter 4 I have re-calibrated the relationship between *GALEX* *FUV* magnitude and stellar age for FGK type stars. However, compared to the calibration in Chapter 2, one may use readily available *Gaia* $(G - G_{\rm BP})$ colors instead of Johnson $(B-V)$ colors. Furthermore, I have constructed age-velocity relations for a set of 660 Geneva-Copenhagen Survey stars using *FUV*-determined ages. I find that the AVRs are fit with a power law function consistent with those fit to AVRs constructed by simple simulations of Galactic formation due to Giant Molecular Cloud (GMC) heating. In addition, perigalactic and eccentricity versus *FUV*-age plots show that our collection of stars is consistent to an "inside out" model in which older stars are more centrally located with larger eccentricities, while younger stars are found at larger radii and have smaller eccentricities.

5.2 Future Work

The work in this thesis touches on a number of possible extensions that may be addressed in the coming years.

5.2.1 *GALEX* *NUV* Magnitudes as a Metallicity Indicator

Metallicity plays an important role in interpreting the Milky Way's formation history. Often, metallicity is determined through high-resolution spectroscopy. Future proposed work would correlate *NUV* photometry with late-F, G and K type dwarf star metallicity. As *NUV* flux is sensitive to metallicity due to line blanketing, the *GALEX* survey provides a wealth of information for Milky Way dwarf stars. Stellar formation and evolution investigations, such as metallicity explorations of stars in the Galactic halo and disk, benefit from a simple correlation between *NUV* photometry and metallicity.

As a proof of concept, co-authors of papers with this thesis, Graeme Smith and Constance, have compiled a set of dwarf stars from several surveys and demonstrated an *NUV* photometry dependence on metallicity. SEGUE Survey stars were collected, with a large number located in the Milky Way thick disk and halo. The dwarfs in this survey are discernible from giants, as the SEGUE Stellar Parameter Pipeline (Lee et al. 2008a,b) filters by T_{eff}, [Fe/H] abundance and log g. In addition, dwarf stars were identified from several exoplanet catalogs that have GALEX NUV photometry. In all, 45,483 stars have been collected. The collection of stars shows a clear *NUV* flux and metallicity relationship, for metallicity bins of [Fe/H] > -0.4, $-0.7 <$[Fe/H]< -0.4, $-1.3 <$[Fe/H]< -0.7, and [Fe/H]< -1.3. Future work would utilize the demonstrated *NUV* flux and metallicity relationship to define simple correlation functions, providing a method of estimating a fundamental property of dwarf stars.

5.2.2 Extended *Hipparcos* Catalog

The *FUV*-age calibration presented in this thesis has practicality in opening up the vast amount of *GALEX* near-all-sky *FUV* photometry for use in stellar age dating. Considerable overlap to exists between the *GALEX FUV* survey and various large astrometric and stellar abundance surveys including the the Geneva-Copenhagen and RAVE surveys. It follows that FUV-age dating could be incorporated into populations studies of FGK dwarfs within the Galaxy. One specific study of interest would include the Extended *Hipparcos* Catalog (XHIP) (Anderson & Francis 2012). This catalog contains 116,096 *Hipparcos* stars with spectral types, 46,392 with radial velocities, and 18,549 with [Fe/H] abundances. It also includes stellar ages from the Geneva-Copenhagen Survey. Such a large catalog will have substantial overlap with the *GALEX* GR6-7 catalog. Furthermore, XHIP includes identifications of exoplanet host stars. It would be of interest to estimate the ages of such stars using *GALEX* observations and our calibrated *FUV*-age relationship.

Bibliography

Abadi, M. G., Navarro, J. F., Steinmetz, M., & Eke, V. R. 2003, ApJ, 597, 21

Adibekyan, V. Zh., Santos, N. C., Sousa, S. G., & Israelian, G. 2011, A&A, 535, L11

Agüeros, M. A., et al. 2018, ApJ, 862, 33

Anderson, E., & Francis, C. 2012, Astron. Lett. 38, 331–346

Aumer, M., Binney, J., & Schönrich, R. 2016, MNRAS, 462, 1697

Ayres, T. R., Marstad, N. C., & Linsky J. L. 1981, ApJ, 247, 545

Ayres, T. R., Linsky, J. L., Basri, B. S., Landsman, W., Henry, R. C., Moos, H. W., & Stencel R. E. 1982, ApJ, 256, 550

Ayres, T. R., Brown, A., Harper, G. M., & Bennett P. D. 1997, ApJ, 491, 876

Ayres, T. R., Simon, T., Stren, R. A., Drake, S. A., Wood, B. E., & Brown, A. 1998, ApJ, 496, 428

Ayres, T. R., Hodges-Kluck, E., & Brown A. 2007, ApJS, 171, 304

Ayres, T. R. 2015, AJ, 149, 58

Baliunas, S. L., Hartmann, L., & Dupree, A. K. 1983, ApJ, 271, 672

Ballering, N. P., Rieke, G. H., Su, K. Y. L., & Montiel, E. 2013, ApJ, 775, 55

Barbanis, B. & Woltjer, L. 1967, ApJ, 150

Barnes, S. A. 2007, ApJ, 669, 1167

Barry, D. C. 1988, ApJ, 334, 436

Bappu, M. K. V., & Sivaraman, K. R. 1977, MNRAS, 178, 279

Bensby, T., Feltzing, S., & Lundstöm, I. 2004, A&A, 421, 969

Bertelli, G., Girardi, L., Marigo, P. & Nasi, E. 2008, A&A, 484, 815

Bertelli, G., Nasi, E., Girardi, G. & Marigo, P. 2009, A&A, 508, 355

Bianchi, L., Conti, A., & Shiao, B. 2014 AdvSpRes, 53, 900

Bird, J. C., Kazantzidis, S., Weinberg, D. H., Duedes, J., Callegari, S., Mayer, L. & Madau, P. 2013, ApJ, 773, 43

Booth, R. S., Poppenhaeger, K., Watson, C. A., Silva Aguirre, V., & Wolk, S. J. 2017, MNRAS, 471, 1012

Bovy, J., Rix, H. W., & Hogg, D. W. 2012, ApJ, 751, 131

Bovy, J., Rix, H.-W., Schlafly, E. F., Nidever, D. L., Holtzman, J. A., Shetrone, M. & Beers, T. C. 2016, ApJ, 823, 30

Bovy, J. 2017, MNRAS, 470, 1360

Brewer, J. M., Fischer, D. A. , Valenti, J. A. & Piskunov, N. 2016, ApJ, 225, 32

Brook, C. B., Kawata, D., Gibson, B. K. & Freeman, K. 2004, ApJ, 612, 894

Brook, C. B., et al. 2012, MNRAS, 426, 690

Burnstein, D. 1979, ApJ, 234, 829

Carglberg, R. G, Dawson, P. C., Hsu, T., & Vandenberg, D. 1985, ApJ, 294, 674

Casagrande, L., et al. 2011, A&A, 530, A138

Casagrande, L. & VandenBerg, D. A. 2018, MNRAS, 479, L102

Ceverino, D., Dekel, A., Mandelker, N., Bournaud, F., Burkert, A., Genzel, R., & Primack, J 2012, MNRAS, 420, 3490

Choi, J., Dotter, A., Conroy, C., Cantiello, M., Paxton, B., & Johnson, B. D. 2016, ApJ, 823, 102

Cochrane, K. M. & Smith, G. H. 2019, PASP, 131 114201

Conti, A., Bianchi, L., & Shiao, B. 2011, Ap&SS, 335, 329

Crandall, S., Smith, G. H., Subramonian, A., Ho, K., & Cochrane, K. M. 2020, AJ, 160, 217

Czesla, S., Schröter, S., Schneider, C. P., Huber, K. F., Pfeifer, F., Andreasen, D. T., & Zechmeister, M. 2019, https://ui.adsabs.harvard.edu/abs/2019ascl.soft06010C

Daniel, S. A., Latham, D. W., Mathieu, R. D. & Twarog, B. A. 1994, PASP, 106, 281

Delgado Mena, E., et al. 2017, A&A, 606, A94

De Simone, R., Wu, X., & Tremaine, S. 2004, MNRAS, 350, 627

Deutsch, A. J. 1970, in Ultraviolet Stellar Spectra and Related Ground-Based Observations, Proc. IAU Symposium no. 36, ed. L. Houziaux & H. E. Butler (Dordrecht, Reidel), p. 199

Dixon, D., Tayar, J., & Stassun, K. G. 2020, AJ, 160, 12

Doherty, L. R. 1985, MNRAS217, 41

Dotter, A. 2016, ApJS, 222, 8

Dupree, A. K., Whitney, B. A., & Pasquini, L. 1999, ApJ, 520, 751

Dupree, A. K., Lobel, A., Young, P. R., Ake, T. B., Linsky, J, L., & Redfield, S. 2005, ApJ, 622, 629

Eggen, O. J., Lynden-Bell, D.., & Sandage, A. R. 1962, ApJ, 136, 748E

Findeisen, K., Hillenbrand, L., & Soderblom, D. 2011, AJ, 142, 23

Fuhrmann, K., 1998, A&A, 338, 161

Brown, A. G. A. et al. 2016, A&A, 595, A2

Gaia Collaboration, et al. 2018, A&A, 616, A10

Gaia Collaboration, et al. 2018, A&A, 616, A11

Gilmore, G., & Reid, N. 1983, MNRAS, 202, 1025

Gondoin, P. 1999, A&A, 352, 217

Haisch, B., Schmitt, J. H. M. M., & Rosso, C. 1991, ApJ, 383, L15

Hänninen, J. & Flynn, C. 2002, MNRAS, 337, 731

Hartmann, L., Dupree, A. K., Jordan, C., & Brown, A. 1985, ApJ, 296, 576

Haywood, M. 2006, MNRAS, 371, 1760

Haywood, M., Di Matteo, P., Lehnert, M. D., Katz, D., & Gómez, A. 2013, A&A, 560, A109

Haywood, M., Lehnert, M. D., Di Matteo, P., Snaith, O. Schultheis, M., Katz, D., & Gómez, A. 2016, A&A, 589, A66

Hoffleit, D. E., & Warren, W. H. jr., 1991, The Bright Star Catalogue, 5th Rev. Ed., Yale Univ. Obs., New Haven

Holmberg, J., Nordstöm, B., & Andersen J. 2007, A&A, 475, 519

Holmberg, J., Nordström, B., & Andersen, J. 2009, A&A, 501, 941

Houk, N. & Swift, C., 1999, Michigan Spectral Survey, Ann Arbor, Dep. Astron., Univ. Michigan, 5, 0

Hünsch, M. & Schröder K. -P. 1996, A&A, 309, L51

Hünsch, M., Schmitt, J. H. M. M., Schroeder, K. -P., & Reimers, D. 1996, A&A, 310, 801

Hünsch, M., Schmitt, J. H. M. M., & Voges, W. 1998, A&AS, 127, 251

Isaacson, H. & Fischer D. 2010, ApJ, 725, 875

Isabel Pérez Martínez, M., Schröder, K. -P., & Cuntz, M. 2011, MNRAS, 414, 418

Jackson, A. P., Davis, T. A., & Wheatley P. J. 2012, MNRAS, 422, 2024

Jeffers, J. N. R. 1952, Forestry: An International Journal of Forest Research, 25, 66

Jenkins, J. S., et al. 2011, A&A, 531, A8

Jordi, C. 2018, *Gaia DR2 Photometry*, Gaia Data Workshop, Heidelberg, June 19, 2018

Jørgensen, B. R. & Lindegren L. 2004, A&A, 436, 127

Keenan, P. C. & McNeil, R. C. 1989, ApJS, 71, 245

Kim, Y.-C., Demarque, P., Yi, S. K., & Alexander, D. R. 2002, ApJS, 143, 499

Koch, A., et al. 2007, AJ, 133, 270

Koevari, Z., et al., 2007, A&A, 463, 1071

Kokubo, E., & Ida, S. 1992, PASJ, 44, 601

Kumamoto, J., Baba, J., & Saitoh, T. R. 2017, Publications of the Astronomical Society of Japan, 69, 32

Kurucz, R. L. 1992, The Stellar Populations of Galaxies, IAU Symp. No. 149, ed. B. Barbuy, & A. Renzini (Dordrecht: Kluwer) 225

Lacey, C. G. & Ostriker, J. P. 1985, AJ, 299, 633

Latham, D. W. 1992, IAU Coll. 135, Complementary Approaches to Double and Mul-

tiple Star Research, ASP Conf. Ser. 32, ed. H. A. McAlister, & W. I. Hartkopf (San Francisco, CA: ASP) 110

Layden, A.C., & Sarajedini, A. 2000, AJ, 119, 1760

Lee, Y. S., et al. 2008, AJ, 136, 2022

Lee, Y. S., et al. 2008, AJ, 136, 2050

Lin, J., Dotter, A., Ting, Y. S., & Asplund, M. 2018, MNRAS477, 2966

Linsky, J. L. & Haisch B. M. 1979, ApJ, 229, L2

Loebman, S. R., Roškar, R., Debattista, V. P., Ivezić, Z., Quinn, T. R., & Wadsley, J. 2011 ApJ 737 8

Lorenzo-Oliveira, D., Porto De Mello, G. F., Dutra-Ferreira, L., & Ribas, I. 2016, A&A595 A11

Lorenzo-Oliveira, D., et al. 2018, A&A, 619, A73

Mackereth, J. T., et al. 2019, MNRAS, 489, 176

Madau, P. & Dickinson M. 2014, Annu. Rev. Astron. Astrophys., 52, 415

Maeder, A. & Meynet G. 2014, ApJ, 793, 123

Maggio, A., Vaiana, G. S., Haisch, B. M., Stern, R. A., Bookbinder, J., Harnden, F. R. Jr., & Rosner, R. 1990, ApJ, 348, 253

Mamajek, E. E. & Hillenbrand L. A. 2008, ApJ, 687, 1264

Martin, C. et al. 2003, SPIE Conf. 4854, Future EUV-UV and Visible Space Astrophysics Missions and Instrumentation

Martin, D. C., et al. 2005, ApJ, 619, L1

Massarotti, A., Latham, D. W., Stefanik R. P. & Fogel, J. 2008, AJ, 135, 209

Matteucci, F. & Francois, P. 1989, MNRAS, 239, 885

Mermilliod, J. C., Mermilliod, M., & Hauck, B. 1997, &AS, 124, 349

Minchev, I., Chiappini, C., & Martig, M. 2013, A&A, 558, A9

Mints, A. & Hekker, S. 2018, A&A, 618, A54

Moetazedian, R. & Just, A. 2016, MNRAS, 459, 2905

Morrissey, P., et al. 2007, ApJS, 173, 682

Netopil M., Paunzen E., Stütz C.: Developments of the Open Cluster Database WEBDA. In: Moitinho A., Alves J. (eds.). Star Clusters in the Era of Large Surveys, Astrophysics and Space Science Proceedings. Springer, Berlin, Heidelberg, 53 (2012)

Navarro, J. F., et al. 2018 MNRAS, 476, 3648

Nordström, B., et al. 2004a, PASA, 21, 129

Nordström, B., et al. 2004b, A&A, 418, 989

Noyes, R. W., Hartmann, L. W., Baliunas, S. L., Duncan, D. K., & Vaughan, A. H. 1984, ApJ, 279, 763

Pace, G. & Pasquini L. 2004, A&A, 426, 1021

Pasquini, L., Brocato, E., & Pallavicini, R. 1990, A&A, 234, 277

Paxton, B., Bildsten, L., Dotter, A., Herwig, F., Lesaffre, P., & Timmes, F. 2016, ApJS, 192, 3

Paxton, B., et al. 2013, ApJS, 208, 4

Paxton, B., et al. 2015, ApJS, 220, 15

Pérez Martínez, M. I., Schröder, K. P., & Cuntz, M. 2011, , 414, 418

Piatti, E. A., & Geisler, D. 2013, AJ, 145, 17

Pietrinferni, A., Cassisi, S., Salaris, M. & Castelli, F. 2004, ApJ, 612, 168

Pietrinferni, A., Cassisi, S., Salaris, M. & Castelli, F. 2006, ApJ, 642, 797

Pietrinferni, A., Cassisi, S., Salaris, M., Percival, S., & Ferguson, J. W. 2009, ApJ, 697, 275

Pilyugin, L. S. & Edmunds, M. G. 1996, A&A, 313, 783

Pizzolato, N., Maggio, A., Micela, G., Sciortino, S., & Ventura, P. 2003, A&A, 397, 147

Pont, F. & Eyer L. 2004, MNRAS, 351, 487

Prochaska, J. X., Naumov, S. O., Carney, B. W., McWilliam, A., & Wolfe, A. M. 2000, AJ, 120, 2513

Rana, N. C. & Basu, S. 1992, A&A, 265, 499

Reid, I. N., Turner, E. L, Turnbull, M. C., Mountain, M., & Valenti J. A. 2007, ApJ, 665, 767

Rix, H. & Bovy, J. 2013, Astron. Astrophys. Rev., 21, 61

Robin, A. C., Reylé, C., Fliri, J., Czekaj, M., Robert, C. P., & Martins A. M. M. 2014, A&A, 569, A13

Rocha-Pinto, H. J., Flynn, C., Scalo, J., Hänninen, J., Maciel, W. J., & Hensler, G. 2004, A&A, 423, 517

Roman N. G., 1950, AJ, 55, 182

Roman N. G., 1950b, ApJ, 112, 554

Rutten, R. G. M., & Pylyser, E. 1988, A&A, 191, 227

Salim, S., et al. 2005, ApJ, 619, L39

Sanders, J. L. & Das P. 2018, MNRAS, 481, 4093

Schönrich, R. & Binney, J. 2009, MNRAS, 396, 203

Schröder, K. -P., Mittag, M., Jack, D., Rodríguez Jiménez, A., & Schmitt J. H. M. M. 2020, MNRAS, 492, 1110

Schuster, W. J., Moreno, E., Nissen, P. E., & Pichardo B. 2012, A&A, 538, 21

Seabroke, G. M & Gilmore, G. 2007, MNRAS, 380, 1348

Sierchio, J. M., Rieke, G. H., Su, K. Y. L., & Gáspár, A. 2014, ApJ, 785, 33

Simon, T. 1984, ApJ, 279, 738

Simon, T., Herbig, G., & Boesgaard, A. M. 1985, ApJ, 293, 551

Simon, T., & Drake, S. A. 1989, ApJ, 346, 303

Skumanich, A. 1972, ApJ, 171, 565

Smith, G. H. & Shetrone M. D. 2000, PASP, 112, 1320

Smith, G. H. & Redenbaugh A. K. 2010, PASP, 122, 1303

Smith, G. H., Hargrave, M., & Eckholm, E. 2017, PASA, 34, 49

Smith, G. H. 2018, PASP, 130, 990

Soderblom, D. R., Duncan, D. K., & Johnson, D. R. H. 1991, ApJ, 375, 722

Soderblom, D. R. 2010, Annu. Rev. Astron. Astrophys., 48, 581

Soderblom, D. R. 2015, Astrophysics & Space Science Proceedings, Vol 39 (Switzerland: Springer), p.3

Soubiran, C., Bienaymé, O., Mishenina, T. V., & Kovtyukh, V. V. 2008, A&A, 480, 91

Spitzer, L. & Schwarzschild, M. 1951, ApJ, 114, 385S

Spitzer, L. & Schwarzschild, M. 1953, ApJ, 118, 106S

Stencel, R. E. 1978, ApJ, 223, L37

Strassmeier, K. G., et al. 2011, A&A, 535, A98

Strömberg, G. 1946, ApJ, 104, 12S

Sun, M., et al. 2018, ApJ, 861, 153

Tayar, J., Claytor, Z. R., Huber, D., & van Sanders, J. 2021, submitted

Taylor, B. J. 2007, AJ, 134, 934

Ting, Y. S. & Rix, H. W. 2019, ApJ, 878, 1

Treyer, M., et al. 2005, ApJ, 619, L19

Tsikoudi, V. 1979, ApJ, 234, 842

Twarog, B. A. 1980a, ApJS, 44, 1

Twarog, B. A. 1980b, ApJ, 242, 242

Valenti, J. A., & Fischer, D. A 2005, ApJS, 159, 141

van Leeuwen, F., 2007, A&A, 474, 653

Veltz, L., et al., 2008, A&A, 480, 753

Walker, I. R., Mihos, J. C., & Hernquist, L. 1996, ApJ, 460, 121

Wenger, M., Ochsenbein, F., Egret, D., et al. 2000, A&AS, 143, 9

Yi, S., Demarque, P., Kim, Y.-C, et al. 2001, ApJS, 136, 417

Wang, S., Bai, Y., He, L., & Liu J. 2020, ApJ, 902, 114

Wenger, M., Ochsenbein, F. & Egret D. 2000, &AS, 143, 9

Wielen, R. 1977, A&A, 60, 263

Weiler, M. 2018, A&A, 617, A138

Wilson, O. C., & Vainu Bappu, M. K. 1957, ApJ, 125, 661

Wilson, O. C. 1967, PASP, 79, 46

Wilson, O. C. 1976, ApJ, 205, 823

Appendix A

Appendix: Supplemental Work on FUV-age Calibration

A.1 The Relationship Between $\log R'_{\rm HK}$ and Stellar Age

Chromospheric and coronal radiation, such as Ca II H and K and soft X-ray emission are often used as stellar activity indicators, and hence age. Figure A.1 shows the relationship between Ca II emission line flux parameter $\log R'_{\rm HK}$ and stellar age. Stars in this plot and their respective $\log R'_{\rm HK}$ estimates and stellar ages were compiled from Ballering et al. (2013). Ages from this source were found in the literature through a combination of techniques including chromospheric activity measurements, X-ray emission, Hertzsprung-Russel diagram placement, surface gravity, gyrochronology, and cluster membership. Here $R'_{\rm HK}$ (Noyes et al. 1984) is the ratio of emission line flux, the determination of which requires high-resolution spectroscopy, to stellar bolometric

flux. This figure demonstrates a clear correlation between this chromospheric activity indicator and stellar age.

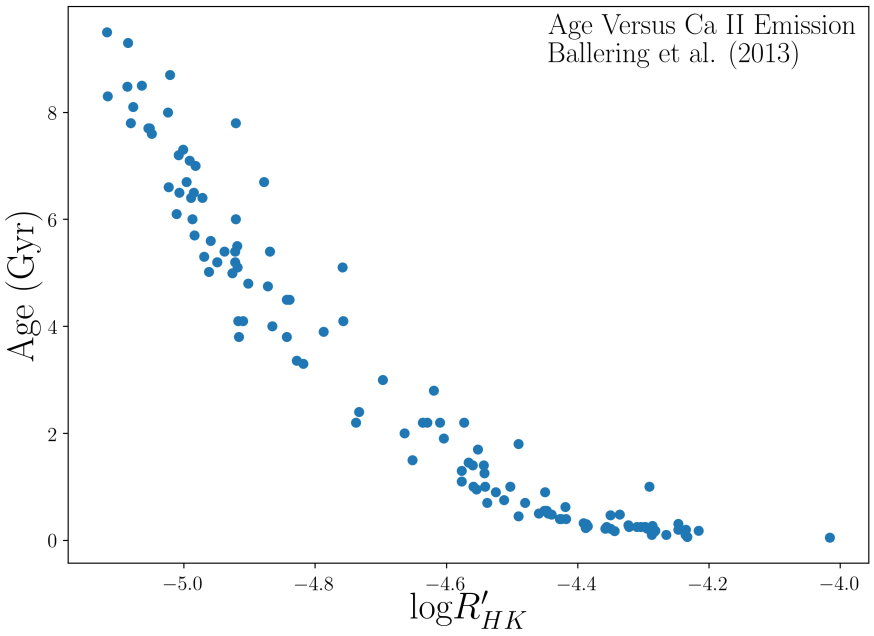

Figure A.1 A demonstration of the relationship between chromospheric activity indicator $\log R'_{\rm HK}$ and stellar age. Estimates for both parameters were compiled from Ballering et al. (2013).

A.2 Metallicity Comparison in Calibration Sample

The FUV-age calibration sample in Chapter 2 have metallicities near solar-abundance with 75% of the dwarfs falling within $-0.2 \leq$[Fe/H]≤ 0.2. The metallicity values for our sample were taken from Casagrande et al. (2011) and Valenti & Fischer (2005). This chapter addresses any concerns related to using multiple sources to compare metallicity estimates. As these two sources determined [Fe/H] values differently one may question whether they are comparable. Figure A.2 shows the dwarf stars from our

sample that have metallicity estimates from both sources [17]. The red line indicates a 1:1 line. We note very little scatter about this 1:1 line and conclude the the metallicities from these two sources are comparable, and both sources may be used to quote metallicities for our stellar sample.

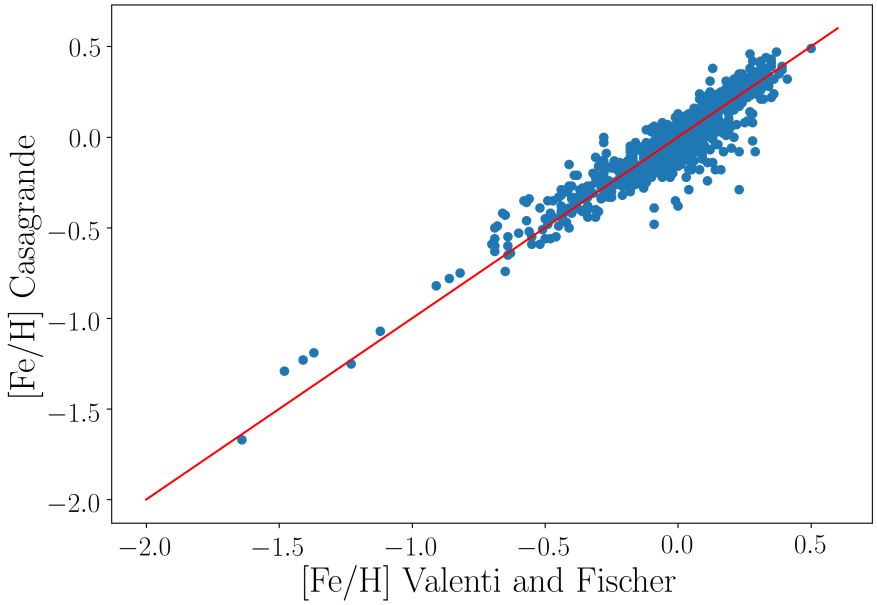

Figure A.2 A comparison of metallicity for stars within our calibration sample which have [Fe/H] estimates in both sources used in Chapter 2: Casagrande et al. (2011) and Valenti & Fischer (2005).

A.3 Gyrochronology Versus *FUV*-Determined Ages

In this section I compare gyrochronology-determined ages and *FUV*-determined ages of field stars from Barnes (2007) and Mamajek & Hillenbrand (2008). Figure A.3 shows gyrochronology-determined ages from these two sources and *FUV*-determined ages, τ, which were estimated with Equations Equations 4.3, 3.4, 2.4, 2.10, and 2.11. In

[17] Note that in the calibration [Fe/H] values were first used from Casagrande et al. (2011) and then Valenti & Fischer (2005) if they were not quoted in the former.

addition, Barnes (2007) and Mamajek & Hillenbrand (2008) also have chromospheric-determined ages estimated from R'_{HK} values. This plot is an interesting exploration as both of these age-dating techniques rely on the spin-down phenomenon. We note that there is significant scatter between the gyrochronology and *FUV*-determined ages for stars older than ~ 4 Gyr.

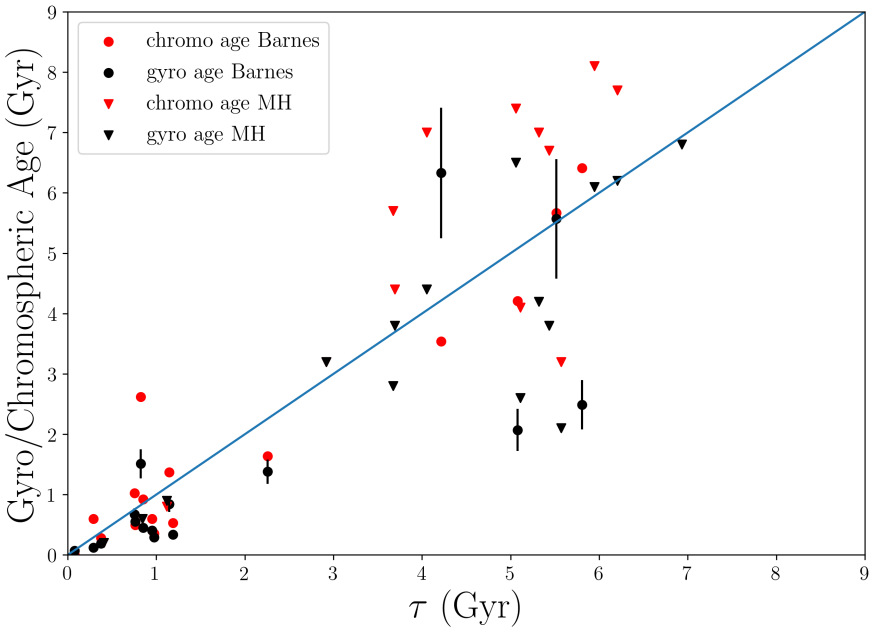

Figure A.3 A comparison between gyrochronology (black) and *FUV*-determined ages of field stars from Barnes (2007) (circles) and Mamajek & Hillenbrand (2008) (triangles). The two sources also quote chromospheric-determined ages (red). Here, τ is the *FUV*-determined age found using Equations 4.3, 3.4, 2.4, 2.10, and 2.11.

Appendix B

Appendix: Tables Relevant to *FUV*-Age Calibration

B.1 Calibration Stellar Sample

Table B.1 includes all FGK field dwarf stars used in the Chapter 2 calibration analysis from catalogs Ballering et al. (2013); Isaacson & Fischer (2010); Sierchio et al. (2014); Lorenzo-Oliveira et al. (2018). Stellar parameters listed include HD identifiers, V and B magnitudes from the *Hipparcos* catalog, *FUV*-B colors with *GALEX* magnitudes, and reported ages from the above sources.

Table B.1: Properties of Field Star Used in *FUV*-Age Calibration

Catalog[a]	HD	V	$(B-V)$	$(FUV-B)$	Q[b]	Age[c](Gyr)
i	HD 105	7.51	0.60	10.10	-2.05	0.2
i	HD 1388	6.51	0.60	11.57	-0.62	5.9
i	HD 7590	6.59	0.59	10.71	-1.42	0.4
i	HD 16397	7.36	0.58	11.54	-0.43	4.6
i	HD 16623	8.76	0.60	11.26	-0.96	5.3
i	HD 20367	6.40	0.57	10.30	-1.54	0.4

Table B.1: Properties of Field Star Used in FUV-Age Calibration

Catalog[a]	HD	V	$(B-V)$	$(FUV-B)$	Q[b]	Age[c](Gyr)
i	HD 25825	7.85	0.59	10.50	-1.62	0.3
i	HD 27859	7.79	0.60	10.46	-1.74	0.8
i	HD 38949	7.80	0.57	10.47	-1.24	0.7
i	HD 52711	5.93	0.59	11.46	-0.68	6.4
i	HD 55575	5.54	0.58	11.33	-0.54	6.3
i	HD 56322	7.88	0.60	10.12	-2.11	0.5
i	HD 78366	5.95	0.58	10.70	-1.30	0.9
i	HD 89307	7.02	0.59	11.30	-0.83	4.9
i	HD 97334	6.41	0.60	10.67	-1.54	0.3
i	HD 98553	7.54	0.59	11.06	-1.07	2.7
i	HD 100180	6.27	0.57	11.18	-0.59	5.1
i	HD 104800	9.21	0.59	11.28	-0.72	4.8
i	HD 104860	7.92	0.60	10.08	-2.08	0.2
i	HD 108510	6.75	0.58	11.02	-0.97	3.6
i	HD 110897	5.95	0.56	10.98	-0.59	6.1
i	HD 117378	7.64	0.59	10.36	-1.77	0.8
i	HD 130948	5.86	0.58	10.47	-1.39	0.4
i	HD 135143	7.84	0.60	11.33	-0.91	4.0
i	HD 142267	6.07	0.60	11.44	-0.74	5.1
i	HD 152555	7.82	0.59	10.08	-2.01	0.1
i	HD 154417	6.00	0.58	10.43	-1.47	0.7
i	HD 155060	7.21	0.56	10.81	-0.84	6.8
i	HD 160693	8.39	0.58	11.36	-0.51	4.5
i	HD 183216	7.13	0.60	10.74	-1.46	0.6
i	HD 187748	6.64	0.59	10.28	-1.82	0.6
i	HD 193901	8.65	0.55	10.68	-0.84	4.0
i	HD 198089	7.43	0.59	11.52	-0.51	6.9
i	HD 199598	6.93	0.58	10.76	-1.23	2.4
i	HD 206860	5.96	0.59	10.37	-1.66	0.3
b	HD 105	7.51	0.60	10.10	-2.05	0.2
b	HD 7590	6.59	0.59	10.71	-1.42	0.6
b	HD 20367	6.40	0.57	10.30	-1.54	0.5
b	HD 23079	7.12	0.58	11.18	-0.79	5.3
b	HD 38949	7.80	0.57	10.47	-1.24	0.9
b	HD 52711	5.93	0.59	11.46	-0.68	6.4
b	HD 55575	5.54	0.58	11.33	-0.54	5.7
b	HD 78366	5.95	0.58	10.70	-1.30	1.0
b	HD 84075	8.59	0.59	10.15	-1.89	0.1
b	HD 88742	6.38	0.59	10.99	-1.11	2.3
b	HD 90712	7.52	0.59	10.39	-1.61	0.3
b	HD 90905	6.88	0.56	10.04	-1.61	0.3

Table B.1: Properties of Field Star Used in FUV-Age Calibration

Catalog[a]	HD	V	$(B-V)$	$(FUV-B)$	Q[b]	Age[c](Gyr)
b	HD 100180	6.27	0.57	11.18	-0.59	3.8
b	HD 104860	7.92	0.60	10.08	-2.08	0.3
b	HD 108954	6.20	0.57	10.95	-0.79	4.1
b	HD 110897	5.95	0.56	10.98	-0.59	6.4
b	HD 115043	6.82	0.60	10.72	-1.53	0.4
b	HD 152555	7.82	0.59	10.08	-2.01	0.1
b	HD 154417	6.00	0.58	10.43	-1.47	0.8
b	HD 183216	7.13	0.60	10.74	-1.46	1.0
b	HD 199598	6.93	0.58	10.76	-1.23	2.2
b	HD 206860	5.96	0.59	10.37	-1.66	0.3
b	HD 207129	5.57	0.60	11.55	-0.67	4.0
s	HD 105	7.51	0.60	10.10	-2.05	0.2
s	HD 7590	6.59	0.59	10.71	-1.42	0.6
s	HD 20367	6.40	0.57	10.30	-1.54	0.5
s	HD 23079	7.12	0.58	11.18	-0.79	5.3
s	HD 26923	6.32	0.57	10.48	-1.30	0.6
s	HD 38949	7.80	0.57	10.47	-1.24	0.9
s	HD 55575	5.54	0.58	11.33	-0.54	5.7
s	HD 78366	5.95	0.58	10.70	-1.30	0.8
s	HD 88742	6.38	0.59	10.99	-1.11	2.3
s	HD 90905	6.88	0.56	10.04	-1.61	0.3
s	HD 97334	6.41	0.60	10.67	-1.54	0.5
s	HD 104860	7.92	0.60	10.08	-2.08	0.3
s	HD 115043	6.82	0.60	10.72	-1.53	0.4
s	HD 130948	5.86	0.58	10.47	-1.39	0.5
s	HD 154417	6.00	0.58	10.43	-1.47	0.8
s	HD 183216	7.13	0.60	10.74	-1.46	1.0
s	HD 206860	5.96	0.59	10.37	-1.66	0.4
i	HD 377	7.59	0.63	10.43	-2.12	0.2
i	HD 1832	7.57	0.64	11.72	-0.98	4.0
i	HD 3821	7.02	0.62	11.14	-1.34	0.9
i	HD 5294	7.41	0.65	11.19	-1.66	0.8
i	HD 8262	6.96	0.63	11.89	-0.67	5.0
i	HD 9986	6.77	0.65	11.68	-1.12	4.6
i	HD 11505	7.43	0.63	11.89	-0.76	6.2
i	HD 12039	8.07	0.65	10.17	-2.67	0.1
i	HD 19467	6.97	0.65	12.11	-0.66	6.2
i	HD 20439	7.78	0.62	10.74	-1.70	0.5
i	HD 24521	9.61	0.64	10.71	-2.04	0.4
i	HD 25445	9.00	0.65	11.58	-1.22	5.9
i	HD 27530	8.16	0.64	11.46	-1.27	4.4

Table B.1: Properties of Field Star Used in FUV-Age Calibration

Catalog[a]	HD	V	$(B-V)$	$(FUV-B)$	Q[b]	Age[c](Gyr)
i	HD 28187	7.79	0.63	11.74	-0.85	5.9
i	HD 28192	8.06	0.63	10.73	-1.85	0.9
i	HD 28992	7.90	0.63	10.71	-1.90	0.6
i	HD 29980	8.03	0.65	10.36	-2.46	0.4
i	HD 30495	5.49	0.63	10.95	-1.67	0.8
i	HD 30572	8.50	0.62	10.68	-1.83	1.3
i	HD 44614	7.59	0.63	11.69	-0.90	7.6
i	HD 45391	7.15	0.61	11.86	-0.53	4.1
i	HD 56124	6.93	0.63	11.50	-1.11	2.5
i	HD 56202	8.42	0.64	10.55	-2.18	0.4
i	HD 60737	7.70	0.62	10.36	-2.13	0.1
i	HD 65080	8.21	0.64	11.12	-1.57	3.0
i	HD 66171	8.18	0.62	11.61	-0.88	5.6
i	HD 70516	7.71	0.65	10.48	-2.37	0.1
i	HD 71148	6.32	0.62	11.59	-0.94	5.5
i	HD 71881	7.44	0.63	11.50	-1.10	7.7
i	HD 73226	7.54	0.63	11.64	-0.98	7.4
i	HD 77407	7.04	0.61	10.15	-2.19	0.1
i	HD 82905	8.91	0.65	11.78	-1.05	7.3
i	HD 82943	6.54	0.62	11.38	-1.13	5.1
i	HD 88072	7.55	0.65	12.38	-0.41	6.5
i	HD 88371	8.42	0.64	12.03	-0.65	5.6
i	HD 88725	7.75	0.61	11.59	-0.74	5.3
i	HD 90681	7.83	0.65	11.31	-1.53	3.5
i	HD 92719	6.79	0.62	11.57	-0.93	3.7
i	HD 94835	7.94	0.62	11.74	-0.79	2.9
i	HD 95128	5.03	0.62	11.52	-1.01	6.1
i	HD 96700	6.51	0.61	11.56	-0.73	4.0
i	HD 98618	7.65	0.64	11.89	-0.85	6.7
i	HD 101847	8.33	0.63	10.76	-1.89	0.3
i	HD 102158	8.06	0.62	11.32	-1.18	6.4
i	HD 104389	8.45	0.61	11.40	-0.91	2.7
i	HD 106252	7.41	0.63	11.53	-1.13	5.1
i	HD 125612	8.31	0.63	11.46	-1.12	4.2
i	HD 126053	6.25	0.64	12.05	-0.65	5.7
i	HD 129814	7.52	0.64	11.56	-1.11	5.2
i	HD 140296	8.69	0.61	10.37	-1.92	1.3
i	HD 140913	8.06	0.61	10.48	-1.90	0.5
i	HD 145224	8.37	0.64	11.31	-1.45	1.7
i	HD 145229	7.45	0.60	10.39	-1.88	0.5
i	HD 148238	8.94	0.65	11.57	-1.25	6.3

Table B.1: Properties of Field Star Used in FUV-Age Calibration

Catalog[a]	HD	V	$(B-V)$	$(FUV-B)$	Q[b]	Age[c](Gyr)
i	HD 150433	7.21	0.63	11.82	-0.79	5.7
i	HD 159222	6.52	0.64	11.77	-0.93	5.1
i	HD 164595	7.07	0.63	12.00	-0.65	5.9
i	HD 168009	6.30	0.64	11.83	-0.90	6.6
i	HD 168874	6.99	0.64	10.61	-2.06	0.7
i	HD 170778	7.49	0.62	10.59	-1.88	0.4
i	HD 176377	6.80	0.61	11.10	-1.20	4.1
i	HD 183658	7.27	0.64	11.97	-0.74	5.7
i	HD 185414	6.73	0.64	11.31	-1.36	4.3
i	HD 197076	6.43	0.61	11.46	-0.90	4.3
i	HD 205905	6.75	0.62	10.85	-1.66	0.8
i	HD 210323	8.43	0.63	10.88	-1.77	1.4
i	HD 213519	7.68	0.65	11.86	-0.95	7.0
i	HD 217165	7.67	0.62	11.34	-1.10	5.9
i	HD 217813	6.65	0.62	10.84	-1.64	0.5
i	HD 218168	8.12	0.63	10.41	-2.21	0.5
i	HD 219428	8.26	0.61	10.88	-1.45	0.6
i	HD 222582	7.68	0.65	12.12	-0.68	5.2
i	HD 223238	7.69	0.63	11.75	-0.81	7.5
i	HD 224383	7.89	0.64	11.72	-1.03	6.8
b	HD 377	7.59	0.63	10.43	-2.12	0.2
b	HD 6434	7.72	0.61	11.55	-0.84	5.4
b	HD 12039	8.07	0.65	10.17	-2.67	0.1
b	HD 30495	5.49	0.63	10.95	-1.67	0.7
b	HD 60737	7.70	0.62	10.36	-2.13	0.3
b	HD 70516	7.71	0.65	10.48	-2.37	0.2
b	HD 71148	6.32	0.62	11.59	-0.94	5.4
b	HD 72905	5.63	0.62	10.49	-1.96	0.2
b	HD 77407	7.04	0.61	10.15	-2.19	0.1
b	HD 95128	5.03	0.62	11.52	-1.01	6.5
b	HD 100167	7.35	0.62	11.33	-1.11	2.2
b	HD 107146	7.04	0.60	10.30	-1.97	0.2
b	HD 126053	6.25	0.64	12.05	-0.65	5.2
b	HD 129333	7.60	0.63	9.72	-2.83	0.1
b	HD 145229	7.45	0.60	10.39	-1.88	0.7
b	HD 150706	7.01	0.61	10.85	-1.46	0.9
b	HD 159222	6.52	0.64	11.77	-0.93	4.1
b	HD 168009	6.30	0.64	11.83	-0.90	7.3
b	HD 170778	7.49	0.62	10.59	-1.88	0.4
b	HD 189567	6.07	0.65	11.72	-1.09	4.5
b	HD 197076	6.43	0.61	11.46	-0.90	4.8

Table B.1: Properties of Field Star Used in FUV-Age Calibration

Catalog[a]	HD	V	$(B-V)$	$(FUV-B)$	Q[b]	Age[c](Gyr)
b	HD 205905	6.75	0.62	10.85	-1.66	1.3
b	HD 210918	6.23	0.65	11.91	-0.89	7.3
b	HD 217813	6.65	0.62	10.84	-1.64	0.5
b	HD 222582	7.68	0.65	12.12	-0.68	5.2
s	HD 377	7.59	0.63	10.43	-2.12	0.2
s	HD 30495	5.49	0.63	10.95	-1.67	0.7
s	HD 60737	7.70	0.62	10.36	-2.13	0.3
s	HD 71148	6.32	0.62	11.59	-0.94	5.4
s	HD 88725	7.75	0.61	11.59	-0.74	6.0
s	HD 92719	6.79	0.62	11.57	-0.93	3.6
s	HD 107146	7.04	0.60	10.30	-1.97	0.2
s	HD 114853	6.93	0.64	11.78	-0.97	5.1
s	HD 126053	6.25	0.64	12.05	-0.65	5.3
s	HD 140913	8.06	0.61	10.48	-1.90	0.6
s	HD 145229	7.45	0.60	10.39	-1.88	0.7
s	HD 159222	6.52	0.64	11.77	-0.93	4.1
s	HD 168009	6.30	0.64	11.83	-0.90	7.3
s	HD 170778	7.49	0.62	10.59	-1.88	0.4
s	HD 199509	6.98	0.62	11.51	-0.95	5.2
s	HD 202628	6.75	0.64	11.27	-1.41	1.9
s	HD 205905	6.75	0.62	10.85	-1.66	1.3
s	HD 210918	6.23	0.65	11.91	-0.89	7.3
s	HD 217813	6.65	0.62	10.84	-1.64	0.5
s	HD 222582	7.68	0.65	12.12	-0.68	5.2
l	HD 6204	8.52	0.65	11.00	-1.82	0.6
l	HD 8291	8.61	0.64	11.42	-1.27	1.9
l	HD 9986	6.77	0.65	11.68	-1.12	3.5
l	HD 16008	8.61	0.65	11.48	-1.30	3.6
l	HD 19467	6.97	0.65	12.11	-0.66	8.8
l	HD 20782	7.36	0.63	11.73	-0.87	7.7
l	HD 30495	5.49	0.63	10.95	-1.67	0.8
l	HD 54351	8.00	0.63	11.74	-0.87	4.0
l	HD 88072	7.55	0.65	12.38	-0.41	4.5
l	HD 129814	7.52	0.64	11.56	-1.11	6.2
l	HD 183658	7.27	0.64	11.97	-0.74	6.0
l	HD 196390	7.33	0.63	11.32	-1.23	1.2
l	HD 197076	6.43	0.61	11.46	-0.90	2.4
l	HD 200633	8.34	0.64	11.79	-0.91	4.1
l	HD 202628	6.75	0.64	11.27	-1.41	0.6
l	HD 208704	7.16	0.64	11.67	-1.04	7.0
l	HD 210918	6.23	0.65	11.91	-0.89	8.9

Table B.1: Properties of Field Star Used in FUV-Age Calibration

Catalog[a]	HD	V	$(B-V)$	$(FUV-B)$	Q[b]	Age[c](Gyr)
l	HD 222582	7.68	0.65	12.12	-0.68	6.7
l	HD 223238	7.69	0.63	11.75	-0.81	5.7
l	HD 224383	7.89	0.64	11.72	-1.03	8.0
i	HD 1461	6.47	0.67	12.33	-0.75	6.8
i	HD 1835	6.39	0.66	10.96	-1.96	0.6
i	HD 4208	7.78	0.66	12.20	-0.77	4.0
i	HD 4915	6.98	0.66	11.69	-1.28	3.8
i	HD 6512	8.15	0.66	11.74	-1.15	6.2
i	HD 8038	8.41	0.70	11.66	-1.64	1.5
i	HD 8648	7.38	0.67	12.02	-1.06	6.6
i	HD 9407	6.52	0.69	12.31	-0.87	6.3
i	HD 10086	6.60	0.69	11.34	-1.88	1.4
i	HD 10145	7.70	0.69	12.14	-1.08	5.2
i	HD 10353	8.48	0.70	10.71	-2.58	0.4
i	HD 12846	6.89	0.66	11.81	-1.14	5.5
i	HD 13825	6.80	0.69	12.11	-1.11	7.9
i	HD 16275	8.66	0.66	11.86	-1.13	5.6
i	HD 18803	6.62	0.70	12.26	-1.00	4.9
i	HD 19034	8.08	0.68	12.07	-1.03	5.1
i	HD 20619	7.05	0.66	11.86	-1.02	2.9
i	HD 22670	9.07	0.70	10.91	-2.39	0.7
i	HD 26736	8.05	0.66	10.73	-2.17	0.4
i	HD 26756	8.45	0.69	11.07	-2.17	0.8
i	HD 26990	7.50	0.66	11.08	-1.86	0.8
i	HD 28099	8.10	0.66	10.95	-2.03	0.7
i	HD 29150	7.58	0.69	12.28	-0.89	4.3
i	HD 30246	8.30	0.66	11.03	-1.95	1.0
i	HD 45161	8.14	0.69	11.34	-1.84	1.2
i	HD 47309	7.60	0.67	12.14	-0.91	7.5
i	HD 51046	8.06	0.68	12.07	-1.04	5.9
i	HD 64324	7.78	0.66	11.14	-1.78	1.0
i	HD 68017	6.78	0.68	11.93	-1.18	5.2
i	HD 76151	6.01	0.66	11.55	-1.39	1.8
i	HD 76752	7.47	0.68	12.09	-1.04	5.9
i	HD 76780	7.63	0.69	12.02	-1.22	3.9
i	HD 79282	8.30	0.65	11.37	-1.50	3.4
i	HD 82460	8.40	0.67	11.59	-1.45	3.2
i	HD 86728	5.37	0.68	12.19	-0.90	8.0
i	HD 89022	8.97	0.68	11.97	-1.15	7.6
i	HD 90156	6.92	0.66	12.18	-0.74	6.0
i	HD 91275	8.68	0.70	12.32	-0.96	5.0

Table B.1: Properties of Field Star Used in FUV-Age Calibration

Catalog[a]	HD	V	$(B-V)$	$(FUV-B)$	Q[b]	Age[c](Gyr)
i	HD 92320	8.38	0.68	11.76	-1.35	3.3
i	HD 92788	7.31	0.69	12.59	-0.66	6.7
i	HD 106116	7.43	0.70	12.57	-0.74	6.8
i	HD 108916	8.49	0.67	10.78	-2.22	0.9
i	HD 109286	8.78	0.70	11.15	-2.13	0.8
i	HD 110537	7.83	0.68	12.25	-0.83	6.9
i	HD 111031	6.87	0.70	12.32	-0.94	8.2
i	HD 112257	7.80	0.67	11.93	-1.06	4.1
i	HD 113039	8.94	0.66	12.19	-0.73	6.6
i	HD 114174	6.78	0.67	11.81	-1.20	5.6
i	HD 114826	8.92	0.68	10.99	-2.17	0.5
i	HD 117122	8.42	0.69	12.52	-0.71	5.4
i	HD 118914	8.89	0.66	12.07	-0.88	8.1
i	HD 119824	8.30	0.66	11.56	-1.34	3.4
i	HD 127334	6.36	0.70	12.28	-1.03	7.5
i	HD 129191	8.19	0.68	12.27	-0.87	6.0
i	HD 132756	7.26	0.69	12.33	-0.89	6.5
i	HD 134987	6.47	0.69	12.28	-0.94	8.1
i	HD 136925	7.91	0.66	12.13	-0.76	7.6
i	HD 138004	7.48	0.68	11.74	-1.35	3.0
i	HD 138573	7.22	0.66	12.17	-0.72	6.5
i	HD 143174	8.65	0.65	11.06	-1.82	1.7
i	HD 152125	8.92	0.70	12.27	-1.02	5.0
i	HD 155968	8.41	0.69	11.76	-1.43	2.0
i	HD 159909	7.28	0.69	12.06	-1.18	6.0
i	HD 164509	8.10	0.67	11.54	-1.44	4.3
i	HD 170469	8.21	0.68	12.30	-0.80	7.6
i	HD 171067	7.20	0.69	12.41	-0.82	4.7
i	HD 186104	7.64	0.66	12.00	-0.97	7.4
i	HD 188298	8.46	0.66	11.05	-1.85	1.8
i	HD 189625	7.34	0.65	11.78	-1.09	2.8
i	HD 201219	8.01	0.69	11.45	-1.78	0.9
i	HD 201989	7.38	0.69	11.06	-2.15	0.3
i	HD 206374	7.45	0.69	11.33	-1.85	0.6
i	HD 207832	8.78	0.69	11.81	-1.42	1.8
i	HD 217014	5.45	0.67	12.08	-0.91	7.6
i	HD 222986	8.81	0.68	10.41	-2.75	0.4
b	HD 1461	6.47	0.67	12.33	-0.75	7.2
b	HD 9472	7.63	0.67	10.99	-2.01	0.5
b	HD 26990	7.50	0.66	11.08	-1.86	1.4
b	HD 64324	7.78	0.66	11.14	-1.78	1.3

Table B.1: Properties of Field Star Used in FUV-Age Calibration

Catalog[a]	HD	V	$(B-V)$	$(FUV-B)$	Q[b]	Age[c](Gyr)
b	HD 68017	6.78	0.68	11.93	-1.18	6.0
b	HD 76151	6.01	0.66	11.55	-1.39	1.9
b	HD 86728	5.37	0.68	12.19	-0.90	8.1
b	HD 90156	6.92	0.66	12.18	-0.74	5.3
b	HD 92788	7.31	0.69	12.59	-0.66	6.5
b	HD 102438	6.48	0.68	12.27	-0.86	5.1
b	HD 134987	6.47	0.69	12.28	-0.94	7.8
b	HD 200746	7.97	0.65	10.52	-2.35	0.5
b	HD 201219	8.01	0.69	11.45	-1.78	1.0
b	HD 201989	7.38	0.69	11.06	-2.15	0.6
b	HD 209779	7.57	0.67	10.83	-2.24	0.6
b	HD 217014	5.45	0.67	12.08	-0.91	7.7
s	HD 1461	6.47	0.67	12.33	-0.75	7.2
s	HD 10086	6.60	0.69	11.34	-1.88	1.3
s	HD 18803	6.62	0.70	12.26	-1.00	4.5
s	HD 20619	7.05	0.66	11.86	-1.02	3.5
s	HD 27466	7.84	0.67	11.69	-1.37	1.5
s	HD 63433	6.90	0.68	10.99	-2.16	0.3
s	HD 64324	7.78	0.66	11.14	-1.78	1.3
s	HD 76151	6.01	0.66	11.55	-1.39	2.2
s	HD 86728	5.37	0.68	12.19	-0.90	8.1
s	HD 90156	6.92	0.66	12.18	-0.74	5.9
s	HD 102438	6.48	0.68	12.27	-0.86	5.2
s	HD 127334	6.36	0.70	12.28	-1.03	8.0
s	HD 134987	6.47	0.69	12.28	-0.94	7.8
s	HD 138004	7.48	0.68	11.74	-1.35	3.8
s	HD 201219	8.01	0.69	11.45	-1.78	1.0
s	HD 217014	5.45	0.67	12.08	-0.91	7.6
s	HD 217343	7.47	0.66	10.45	-2.44	0.2
l	HD 2071	7.27	0.68	11.80	-1.33	4.8
l	HD 6718	8.45	0.66	11.96	-1.00	7.3
l	HD 11195	8.89	0.66	12.09	-0.82	4.9
l	HD 25874	6.74	0.67	12.05	-0.96	7.0
l	HD 45289	6.67	0.67	12.04	-1.02	9.0
l	HD 45346	8.66	0.66	12.53	-0.42	7.0
l	HD 68168	7.34	0.67	11.62	-1.38	5.4
l	HD 78660	8.34	0.66	11.62	-1.36	6.6
l	HD 96423	7.23	0.68	12.18	-0.95	6.5
l	HD 110537	7.83	0.68	12.25	-0.83	6.2
l	HD 114174	6.78	0.67	11.81	-1.20	6.4
l	HD 122194	9.39	0.65	12.11	-0.76	5.5

Table B.1: Properties of Field Star Used in FUV-Age Calibration

Catalog[a]	HD	V	$(B-V)$	$(FUV-B)$	Q[b]	Age[c](Gyr)
l	HD 133600	8.18	0.66	11.96	-0.93	7.2
l	HD 134664	7.76	0.66	11.56	-1.39	3.9
l	HD 138573	7.22	0.66	12.17	-0.72	6.6
l	HD 140538	5.86	0.68	11.81	-1.35	4.5
l	HD 163441	8.43	0.69	11.72	-1.45	5.0
l	HD 183579	8.67	0.65	11.68	-1.18	2.6
l	HD 218544	8.73	0.68	12.15	-0.94	6.8
l	HD 220507	7.59	0.69	12.12	-1.11	8.8

[a] "i" = Isaacson & Fischer (2010), "b" = Ballering et al. (2013), "s" = Sierchio et al. (2014), "l" = Lorenzo-Oliveira et al. (2018)

[b] FUV-excess parameter determined by Equation 3.4 as discussed in Section 2.3.

[c] Literature-quoted ages with the majority derived from stellar chromospheric and coronal activity indicators, and ages from other sources (e.g. surface gravity, gyrochronology, isochrones) being less commonly adopted.

B.2 Thin and Thick Disk Stars

A sample of stars with their chemical abundances from Delgado Mena et al. (2017) is given in Table B.2. These abundances were used to designate thin and thick disk Milky Way constitutions. Stars are ordered by ascending Q value.

Table B.2: Thick and Thin Disc Constituents[a]

Name	$(B-V)$	(FUV)	[α/Fe]	Q[b]	Thin/Thick
HD 19034	0.67	20.83	0.61	-2.26	thick
HD 8638	0.63	21.45	0.47	-1.10	thick
HD 14747	0.68	21.39	0.46	-1.00	thick
HD 213941	0.66	20.49	0.56	-0.97	thick
HD 11397	0.61	21.53	0.45	-0.94	thick

Table B.2: Thick and Thin Disc Constituents[a]

Name	$(B-V)$	(FUV)	[α/Fe]	Q[b]	Thin/Thick
HD 967	0.61	21.03	0.66	-0.93	thick
HD 88725	0.60	19.95	0.54	-0.83	thick
HD 150433	0.64	19.66	0.50	-0.69	thick
HD 97783	0.63	21.33	0.66	-0.69	thick
HD 12387	0.66	19.86	0.38	-0.69	thick
HD 28701	0.61	20.27	0.49	-0.62	thick
HD 77110	0.58	21.50	0.47	-0.59	thick
HD 199288	0.59	18.49	0.51	-0.56	thick
HD 11505	0.63	19.96	0.35	-0.54	thick
HD 212231	0.61	19.99	0.43	-0.50	thick
HD 69611	0.58	19.63	0.66	-0.45	thick
HD 199847	0.59	20.97	0.62	-0.44	thick
HD 181720	0.58	19.92	0.55	-0.31	thick
HD 197197	0.62	20.17	0.37	-0.14	thick
HD 16784	0.68	19.56	0.78	0.15	thick
HD 207869	0.64	21.65	0.21	-2.25	thin
HD 102438	0.68	19.43	0.18	-2.12	thin
HD 161098	0.67	20.83	0.08	-2.10	thin
HD 107094	0.65	21.15	0.12	-2.08	thin
HD 124364	0.66	20.46	0.09	-2.07	thin
HD 4208	0.67	20.65	0.14	-2.00	thin
HD 90156	0.68	19.76	0.12	-1.87	thin
HD 206172	0.67	21.26	0.05	-1.83	thin
HD 110619	0.67	20.39	0.20	-1.82	thin
HD 216777	0.64	20.61	0.20	-1.81	thin
HD 172643	0.68	21.67	-0.01	-1.69	thin
HD 115674	0.68	21.04	-0.03	-1.60	thin
HD 4915	0.67	19.33	0.09	-1.54	thin
HD 28821	0.68	20.45	0.15	-1.51	thin
HD 186302	0.65	21.52	0.02	-1.51	thin
HD 101644	0.68	21.57	0.15	-1.49	thin
HD 1320	0.65	20.63	0.07	-1.49	thin
HD 106116	0.65	20.70	0.03	-1.48	thin
HD 10895	0.66	20.89	0.02	-1.46	thin
HD 212036	0.68	20.98	-0.0	-1.45	thin
HD 8930	0.66	20.76	-0.06	-1.44	thin
HD 104982	0.65	20.55	0.11	-1.43	thin
HD 8038	0.66	20.77	-0.04	-1.41	thin
HD 20619	0.66	19.56	0.05	-1.41	thin
HD 114853	0.64	19.35	0.14	-1.40	thin
HD 16008	0.66	20.74	0.02	-1.36	thin

Table B.2: Thick and Thin Disc Constituents[a]

Name	$(B-V)$	(FUV)	[α/Fe]	Q[b]	Thin/Thick
HD 210272	0.66	19.95	0.13	-1.36	thin
HD 41248	0.61	21.16	0.14	-1.36	thin
HD 97998	0.63	19.43	0.13	-1.35	thin
HD 2071	0.68	19.75	0.04	-1.34	thin
HD 6718	0.64	21.07	-0.02	-1.33	thin
HD 189567	0.64	18.44	0.20	-1.33	thin
HD 8406	0.65	20.23	0.02	-1.32	thin
HD 178904	0.68	21.23	0.02	-1.32	thin
HD 172568	0.63	21.18	0.20	-1.30	thin
HD 101339	0.68	21.40	0.03	-1.29	thin
HD 197083	0.62	21.40	0.23	-1.29	thin
HD 204287	0.66	19.84	0.11	-1.29	thin
HD 29428	0.67	21.81	-0.04	-1.28	thin
HD 28471	0.65	20.79	0.08	-1.26	thin
HD 67	0.67	20.43	-0.05	-1.24	thin
HD 19423	0.64	20.67	0.10	-1.23	thin
HD 210918	0.65	18.79	0.15	-1.23	thin
HD 41323	0.64	21.17	0.09	-1.23	thin
HD 90702	0.68	20.29	-0.09	-1.20	thin
HD 1461	0.68	19.47	0.06	-1.19	thin
HD 44219	0.66	20.61	0.07	-1.19	thin
HD 216008	0.64	20.65	0.05	-1.18	thin
HD 22249	0.67	20.33	-0.03	-1.17	thin
HD 20782	0.65	19.72	0.04	-1.17	thin
HD 190613	0.65	20.80	0.03	-1.16	thin
HD 204313	0.68	20.74	0.04	-1.15	thin
HD 222582	0.65	20.45	0.09	-1.14	thin
HD 109271	0.66	20.35	-0.01	-1.14	thin
HD 78538	0.64	20.03	-0.03	-1.13	thin
HD 76151	0.67	18.22	-0.02	-1.12	thin
HD 215456	0.63	19.24	0.10	-1.10	thin
HD 155968	0.68	20.86	-0.02	-1.09	thin
HD 183658	0.65	19.88	0.03	-1.09	thin
HD 19641	0.63	20.57	0.05	-1.08	thin
HD 214867	0.64	20.91	-0.16	-1.08	thin
HD 4307	0.61	18.41	0.17	-1.08	thin
HD 29303	0.64	20.09	-0.11	-1.07	thin
HD 92719	0.64	18.98	0.04	-1.07	thin
HD 190524	0.62	20.04	-0.01	-1.07	thin
HD 208704	0.60	19.47	0.05	-1.05	thin
HD 129191	0.66	21.14	0.03	-1.05	thin

Table B.2: Thick and Thin Disc Constituents[a]

Name	$(B-V)$	(FUV)	[α/Fe]	Q[b]	Thin/Thick
HD 44594	0.66	18.93	0.06	-1.05	thin
HD 16417	0.66	18.21	0.07	-1.04	thin
HD 201422	0.66	20.02	-0.07	-1.00	thin
HD 223171	0.66	19.28	0.05	-1.00	thin
HD 13578	0.62	20.17	0.10	-0.99	thin
HD 114729	0.62	18.85	0.28	-0.98	thin
HD 96700	0.61	18.68	0.10	-0.98	thin
HD 189625	0.66	19.78	0.01	-0.98	thin
HD 198075	0.59	20.24	0.03	-0.97	thin
HD 221420	0.68	18.71	0.15	-0.97	thin
HD 221343	0.67	20.24	-0.05	-0.97	thin
HD 34449	0.62	20.29	0.01	-0.96	thin
HD 110668	0.67	20.17	0.02	-0.96	thin
HD 161555	0.66	20.11	0.13	-0.96	thin
HD 211415	0.64	17.39	0.12	-0.95	thin
HD 200633	0.66	20.77	-0.04	-0.95	thin
HD 134664	0.67	19.98	-0.06	-0.94	thin
HD 20407	0.58	18.50	0.20	-0.93	thin
HD 27471	0.61	20.26	0.06	-0.92	thin
HD 221146	0.59	19.24	0.09	-0.92	thin
HD 88218	0.60	18.26	0.14	-0.92	thin
HD 34327	0.63	19.57	0.06	-0.91	thin
HD 97037	0.61	19.05	0.08	-0.90	thin
HD 220456	0.63	20.41	-0.01	-0.90	thin
HD 109098	0.63	19.76	0.08	-0.90	thin
HD 218340	0.63	20.31	-0.03	-0.90	thin
HD 156079	0.67	20.16	0.02	-0.89	thin
HD 177409	0.62	19.64	0.03	-0.88	thin
HD 31527	0.59	19.54	0.09	-0.88	thin
HD 25912	0.66	20.37	-0.03	-0.87	thin
HD 32804	0.65	19.71	-0.06	-0.87	thin
HD 10180	0.63	19.65	0.07	-0.85	thin
HD 82114	0.62	19.31	-0.03	-0.85	thin
HD 125612	0.61	20.39	-0.06	-0.85	thin
HD 361	0.62	19.04	0.02	-0.85	thin
HD 144585	0.66	18.83	0.07	-0.85	thin
HD 217395	0.58	20.08	0.00	-0.85	thin
HD 21161	0.61	19.75	0.03	-0.84	thin
HD 199190	0.62	18.88	0.08	-0.83	thin
HD 90936	0.63	20.68	-0.03	-0.83	thin
HD 86652	0.64	20.48	-0.07	-0.80	thin

Table B.2: Thick and Thin Disc Constituents[a]

Name	$(B-V)$	(FUV)	[α/Fe]	Q[b]	Thin/Thick
HD 207129	0.60	17.72	0.02	-0.80	thin
HD 218379	0.64	19.62	0.09	-0.80	thin
HD 116410	0.67	20.16	-0.04	-0.78	thin
HD 23030	0.65	19.95	0.10	-0.78	thin
HD 16382	0.61	19.87	-0.02	-0.76	thin
HD 1388	0.59	18.68	0.05	-0.76	thin
HD 211317	0.65	19.44	0.06	-0.76	thin
HD 217786	0.58	19.73	0.10	-0.76	thin
HD 217958	0.68	20.40	0.02	-0.76	thin
HD 199960	0.63	18.40	-0.01	-0.75	thin
HD 201496	0.6	20.11	0.01	-0.74	thin
HD 88742	0.59	17.97	-0.06	-0.74	thin
HD 122862	0.58	17.79	0.08	-0.73	thin
HD 213240	0.61	18.91	0.03	-0.73	thin
HD 168871	0.58	18.36	0.08	-0.72	thin
HD 208672	0.61	19.97	-0.10	-0.72	thin
HD 85725	0.62	18.55	0.04	-0.72	thin
HD 82943	0.64	18.55	-0.02	-0.71	thin
HD 153276	0.60	20.27	0.06	-0.70	thin
HD 39091	0.58	17.52	0.02	-0.70	thin
HD 216435	0.62	18.16	-0.01	-0.69	thin
HD 202209	0.62	19.87	-0.07	-0.68	thin
HD 196800	0.59	19.42	-0.03	-0.68	thin
HD 180409	0.58	18.46	0.07	-0.68	thin
HD 38973	0.59	18.54	0.01	-0.67	thin
HD 29980	0.63	19.04	-0.03	-0.66	thin
HD 9782	0.60	19.13	-0.02	-0.66	thin
HD 7449	0.60	19.06	-0.00	-0.64	thin
HD 71479	0.63	19.27	0.01	-0.63	thin
HD 204385	0.59	19.04	0.02	-0.61	thin
HD 2567	0.64	20.15	-0.01	-0.60	thin
HD 44120	0.59	19.28	0.03	-0.60	thin
HD 9578	0.59	19.55	-0.07	-0.59	thin
HD 115341	0.60	19.56	-0.05	-0.58	thin
HD 24085	0.60	19.58	0.01	-0.57	thin
HD 31103	0.59	19.41	-0.04	-0.57	thin
HD 108063	0.65	18.51	0.05	-0.54	thin
HD 457	0.63	19.76	-0.01	-0.51	thin
HD 11226	0.58	18.66	0.03	-0.48	thin
HD 144846	0.59	19.90	-0.02	-0.48	thin
HD 24062	0.63	19.41	-0.08	-0.45	thin

Table B.2: Thick and Thin Disc Constituents[a]

Name	$(B-V)$	(FUV)	[α/Fe]	Q[b]	Thin/Thick
HD 209458	0.58	19.41	0.21	-0.42	thin
HD 18083	0.59	19.69	-0.05	-0.32	thin
HD 199086	0.59	19.42	-0.12	-0.28	thin
HD 139879	0.63	19.62	-0.03	-0.24	thin
HD 206116	0.60	19.31	-0.15	0.19	thin

[a] These stars were collected from Delgado Mena et al. (2017). We reduced the sample to include stars with *GALEX FUV* magnitudes and to those with colors $0.575 \leq (B-V) \leq 0.685$.

[b] FUV-excess parameter determined by Equation 3.4 as discussed in Section 2.3.

Appendix C

Appendix: Red Giant Sample

Table C.1 includes all red giant stars used in the Chapter 3 analysis. The stars are organized by HD identifiers.

Table C.1: Giant Star Sample

Name	*GALEX* *FUV*	*Gaia* G	*Gaia* σ_G	*Gaia* $G_{\rm BP}$	*Gaia* $\sigma_{G_{\rm BP}}$	*ROSAT* $\log(L_X/L_{bol})$[a]
HD 1227	20.08	5.87	0.0	6.36	0.0	-6.09
HD 1522	18.38	3.08	0.01	3.94	0.01	-6.94
HD 1737	18.28	4.87	0.0	5.43	0.0	-5.24
HD 2630	14.65	6.04	0.0	6.26	0.0	-5.35
HD 4482	18.04	5.22	0.0	5.76	0.0	-5.48
HD 4502	15.21	3.68	0.0	4.39	0.01	-4.81
HD 4737	18.84	6.03	0.0	6.5	0.0	-5.32
HD 5516	17.78	4.05	0.01	4.64	0.01	-5.31
HD 6245	18.48	5.11	0.0	5.62	0.0	-5.81
HD 6559	19.15	5.82	0.0	6.39	0.0	-5.31
HD 6763	13.4	5.4	0.0	5.61	0.0	-5.66
HD 6793	17.38	5.09	0.0	5.59	0.0	-4.51
HD 7672	16.38	5.24	0.0	5.78	0.01	-3.9
HD 8634	14.98	6.06	0.0	6.32	0.0	-5.19
HD 8829	12.92	5.41	0.0	5.61	0.0	-5.77
HD 8921	19.89	5.72	0.0	6.45	0.01	-6.11
HD 9774	18.85	4.98	0.0	5.53	0.0	-6.23
HD 10072	18.04	4.73	0.0	5.25	0.0	-5.34
HD 10308	15.98	6.09	0.0	6.34	0.0	-4.6

Table C.1: Giant Star Sample

Name	*GALEX* *FUV*	*Gaia* *G*	*Gaia* σ_G	*Gaia* $G_{\rm BP}$	*Gaia* $\sigma_{G_{\rm BP}}$	*ROSAT* $\log(L_X/L_{bol})$[a]
HD 10588	18.59	6.07	0.0	6.55	0.0	-5.1
HD 11025	14.86	5.4	0.0	5.91	0.0	-5.22
HD 11559	17.99	4.3	0.0	4.85	0.0	-5.65
HD 11937	16.83	3.38	0.0	4.01	0.01	-4.92
HD 12055	13.65	4.53	0.0	5.06	0.0	-5.25
HD 12173	13.25	6.16	0.0	6.24	0.0	-5.79
HD 12641	16.89	5.7	0.0	6.18	0.0	-5.28
HD 15889	19.56	5.98	0.0	6.53	0.0	-5.15
HD 15920	18.63	4.88	0.0	5.4	0.0	-5.7
HD 16058	18.6	4.41	0.0	5.67	0.01	-5.91
HD 16161	18.66	4.58	0.01	5.11	0.0	-5.99
HD 16246	15.15	6.38	0.0	6.62	0.0	-4.28
HD 16327	15.57	6.07	0.0	6.33	0.0	-5.14
HD 17006	18.86	5.86	0.0	6.33	0.0	-4.98
HD 17824	18.28	4.45	0.0	5.02	0.0	-5.49
HD 18953	18.38	5.06	0.0	5.57	0.0	-4.82
HD 19926	13.95	5.11	0.0	5.8	0.0	-5.37
HD 20313	14.09	5.59	0.0	5.77	0.0	-5.93
HD 21024	14.92	5.39	0.0	5.65	0.0	-5.45
HD 22231	20.56	5.34	0.0	5.93	0.0	-5.87
HD 23838	14.91	5.42	0.0	5.86	0.0	-5.4
HD 24497	11.83	5.9	0.0	6.43	0.0	-5.52
HD 26076	20.82	5.76	0.0	6.29	0.0	-5.05
HD 26575	19.69	6.12	0.0	6.69	0.0	-5.51
HD 27022	17.72	5.02	0.0	5.48	0.0	-5.0
HD 28525	14.6	5.42	0.0	5.9	0.0	-5.09
HD 31553	18.65	5.41	0.0	6.06	0.0	-5.58
HD 31910	15.83	3.69	0.0	4.29	0.01	-6.02
HD 34172	19.11	5.57	0.0	6.07	0.0	-5.99
HD 34658	14.37	5.21	0.0	5.46	0.0	-5.77
HD 37434	17.27	5.76	0.0	6.4	0.0	-4.93
HD 37763	20.59	4.81	0.0	5.44	0.0	-6.63
HD 38645	19.25	5.97	0.0	6.46	0.0	-5.25
HD 39070	16.92	5.32	0.0	5.81	0.01	-5.64
HD 39523	18.18	4.13	0.0	4.78	0.0	-5.63
HD 39743	17.88	6.28	0.0	6.83	0.01	-4.19
HD 46730	13.81	6.19	0.0	6.39	0.0	-6.09
HD 47442	14.99	4.02	0.0	4.71	0.0	-6.49
HD 47703	16.54	6.33	0.0	6.62	0.0	-5.54
HD 50337	12.12	4.1	0.0	4.66	0.0	-6.22

Table C.1: Giant Star Sample

Name	*GALEX* *FUV*	*Gaia* *G*	*Gaia* σ_G	*Gaia* $G_{\rm BP}$	*Gaia* $\sigma_{G_{\rm BP}}$	*ROSAT* $\log(L_X/L_{bol})$[a]
HD 50522	15.1	4.19	0.01	4.58	0.0	-5.87
HD 51266	20.77	5.98	0.0	6.49	0.0	-5.54
HD 54719	19.62	3.95	0.01	4.69	0.01	-6.68
HD 57727	18.77	4.73	0.0	5.27	0.0	-5.61
HD 62141	19.6	5.99	0.0	6.49	0.0	-5.69
HD 62264	16.32	5.99	0.0	6.43	0.0	-5.74
HD 62898	19.09	4.34	0.0	5.42	0.0	-6.4
HD 68290	17.93	4.41	0.0	4.95	0.0	-5.53
HD 69148	18.43	5.48	0.0	5.96	0.0	-5.88
HD 71152	13.98	6.88	0.0	7.04	0.0	-4.36
HD 71369	17.01	3.03	0.0	3.77	0.01	-6.44
HD 71433	16.64	6.47	0.0	6.76	0.0	-5.02
HD 73596	14.64	6.1	0.0	6.33	0.0	-5.89
HD 74485	18.97	5.87	0.0	6.36	0.0	-5.3
HD 77996	18.74	4.58	0.0	5.26	0.0	-5.58
HD 78235	18.3	5.15	0.0	5.66	0.0	-5.02
HD 78668	18.65	5.5	0.0	6.01	0.0	-5.06
HD 79193	13.39	6.05	0.0	6.19	0.0	-5.59
HD 79940	14.27	4.45	0.0	4.76	0.0	-6.31
HD 80710	16.73	5.71	0.0	6.41	0.0	-5.95
HD 81799	18.18	4.32	0.0	4.97	0.0	-5.66
HD 81873	19.79	5.39	0.0	5.97	0.0	-5.78
HD 82210	16.56	4.28	0.0	4.76	0.0	-4.46
HD 82635	17.06	4.23	0.0	4.79	0.0	-5.1
HD 83108	15.07	6.37	0.0	6.6	0.0	-5.29
HD 84441	15.08	2.6	0.0	3.73	0.07	-7.0
HD 85206	18.29	5.53	0.0	6.22	0.0	-5.72
HD 85396	19.24	5.15	0.0	5.67	0.0	-5.62
HD 85945	18.06	5.71	0.0	6.2	0.0	-4.46
HD 87682	19.51	5.94	0.0	6.43	0.0	-5.26
HD 88639	18.17	5.82	0.0	6.3	0.01	-4.85
HD 88786	19.52	6.24	0.0	6.7	0.0	-5.28
HD 90071	13.64	6.16	0.0	6.35	0.0	-5.25
HD 91135	16.66	6.38	0.0	6.67	0.0	-5.94
HD 93813	18.12	2.79	0.03	3.71	0.03	-7.0
HD 95314	20.56	5.24	0.0	6.15	0.0	-5.79
HD 98233	20.48	6.43	0.0	6.93	0.0	-5.28
HD 99564	15.64	5.8	0.0	6.08	0.01	-5.15
HD 99967	19.5	5.91	0.0	6.61	0.01	-6.12
HD 100418	16.42	5.9	0.0	6.22	0.0	-5.27

Table C.1: Giant Star Sample

Name	*GALEX* *FUV*	*Gaia* *G*	*Gaia* σ_G	*Gaia* $G_{\rm BP}$	*Gaia* $\sigma_{G_{\rm BP}}$	*ROSAT* $\log(L_X/L_{bol})$[a]
HD 101107	13.64	5.44	0.0	5.67	0.0	-6.04
HD 101112	20.51	5.9	0.0	6.46	0.0	-5.91
HD 101132	13.77	5.53	0.0	5.75	0.0	-5.42
HD 101154	20.19	5.95	0.0	6.55	0.0	-5.45
HD 102070	17.59	4.37	0.0	4.96	0.0	-6.19
HD 103484	18.12	5.28	0.0	5.81	0.0	-5.23
HD 104438	19.43	5.26	0.0	5.85	0.0	-6.11
HD 106677	16.46	5.86	0.0	6.49	0.01	-3.96
HD 108225	19.42	4.72	0.0	5.26	0.0	-6.15
HD 109272	19.6	5.33	0.0	5.81	0.0	-5.94
HD 109379	16.08	2.25	0.0	7.51	0.41	-7.44
HD 112989	16.63	4.42	0.0	5.12	0.0	-5.96
HD 113049	19.05	5.7	0.0	6.26	0.0	-5.27
HD 113226	17.25	2.45	0.0	3.72	0.08	-6.47
HD 114474	19.6	4.9	0.0	5.5	0.01	-5.97
HD 115337	15.63	6.06	0.0	6.53	0.01	-5.63
HD 115659	17.14	2.62	0.0	3.52	0.03	-6.02
HD 117566	17.46	5.54	0.0	5.97	0.0	-4.73
HD 119458	16.43	5.75	0.0	6.21	0.0	-6.12
HD 120048	18.54	5.68	0.0	6.19	0.0	-5.05
HD 120064	14.38	5.82	0.0	6.12	0.0	-5.03
HD 122744	19.42	6.01	0.0	6.49	0.0	-5.67
HD 129312	17.52	4.53	0.01	5.1	0.0	-5.71
HD 130529	18.23	5.22	0.0	5.98	0.0	-5.44
HD 132813	15.72	3.09	0.02	4.95	0.02	-6.67
HD 133208	17.72	3.14	0.0	3.86	0.01	-6.76
HD 136138	13.95	5.39	0.0	5.94	0.0	-5.11
HD 136407	14.15	6.02	0.0	6.25	0.0	-5.59
HD 139906	17.9	5.6	0.0	6.06	0.0	-5.81
HD 141714	16.83	4.33	0.0	4.8	0.0	-4.91
HD 144208	11.4	5.6	0.0	5.97	0.0	-5.53
HD 147266	19.35	5.77	0.0	6.28	0.0	-5.63
HD 147675	16.8	3.52	0.0	4.16	0.01	-5.27
HD 148374	19.57	5.76	0.01	6.07	0.02	-5.87
HD 148387	17.1	2.48	0.02	3.22	0.02	-7.62
HD 150450	18.78	3.94	0.0	5.15	0.0	-6.97
HD 150682	14.42	5.8	0.0	6.03	0.0	-5.31
HD 150997	17.02	3.12	0.0	3.88	0.01	-6.58
HD 151087	13.54	5.94	0.0	6.12	0.0	-5.28
HD 151900	14.67	6.19	0.0	6.43	0.0	-5.22

Table C.1: Giant Star Sample

Name	*GALEX* *FUV*	*Gaia* *G*	*Gaia* σ_G	*Gaia* $G_{\rm BP}$	*Gaia* $\sigma_{G_{\rm BP}}$	*ROSAT* $\log(L_X/L_{bol})$[a]
HD 153956	20.44	5.69	0.0	6.31	0.0	-6.03
HD 154619	19.5	6.13	0.0	6.61	0.0	-5.71
HD 155103	13.04	5.28	0.0	5.5	0.0	-6.21
HD 156015	13.63	5.19	0.01	5.63	0.02	-4.85
HD 156266	19.37	4.39	0.01	4.99	0.0	-6.54
HD 156971	14.0	6.37	0.0	6.56	0.0	-5.6
HD 159181	14.39	2.38	0.0	3.35	0.03	-5.9
HD 161814	19.62	5.49	0.0	6.03	0.0	-5.47
HD 163217	18.27	4.76	0.0	5.44	0.0	-5.94
HD 165462	19.45	5.97	0.0	6.57	0.0	-5.32
HD 166208	17.66	4.71	0.0	5.23	0.0	-5.45
HD 168322	20.71	5.84	0.0	6.37	0.0	-5.8
HD 169836	19.81	5.46	0.0	5.99	0.0	-5.1
HD 175824	14.98	5.71	0.0	5.98	0.0	-5.19
HD 176598	18.43	5.35	0.0	5.88	0.0	-5.3
HD 180006	18.81	4.82	0.0	5.38	0.0	-6.22
HD 181597	21.16	5.99	0.0	6.59	0.0	-5.83
HD 184398	13.11	6.0	0.0	6.66	0.01	-5.02
HD 184492	18.16	4.71	0.0	5.37	0.0	-5.47
HD 187372	19.34	5.31	0.0	6.42	0.0	-6.23
HD 189831	19.61	4.2	0.0	5.04	0.0	-6.8
HD 190252	19.24	6.08	0.0	6.55	0.0	-5.37
HD 196385	13.63	6.29	0.0	6.48	0.0	-5.65
HD 196574	18.71	4.01	0.0	4.56	0.0	-6.22
HD 199253	19.46	4.84	0.0	5.46	0.0	-5.88
HD 199442	21.32	5.7	0.0	6.33	0.0	-5.26
HD 199532	14.4	4.93	0.0	5.26	0.0	-4.45
HD 199665	19.32	5.24	0.0	5.75	0.0	-5.7
HD 199951	17.28	4.37	0.0	4.9	0.0	-5.02
HD 200763	20.12	4.85	0.0	5.46	0.0	-5.95
HD 202951	19.86	5.19	0.0	6.25	0.01	-5.81
HD 203387	16.74	3.97	0.0	4.52	0.0	-4.94
HD 204960	19.95	5.26	0.0	5.83	0.0	-6.04
HD 207964	14.35	5.81	0.0	6.03	0.0	-4.92
HD 209278	12.27	7.06	0.0	7.12	0.01	-4.81
HD 210960	14.94	5.27	0.0	5.8	0.0	-5.95
HD 211416	16.4	2.22	0.0	3.57	0.03	-7.08
HD 212132	13.77	5.52	0.0	5.74	0.0	-5.16
HD 212271	18.67	5.26	0.0	5.78	0.0	-4.9
HD 214987	19.45	5.8	0.0	6.32	0.0	-5.36

Table C.1: Giant Star Sample

Name	*GALEX* *FUV*	*Gaia* *G*	*Gaia* σ_G	*Gaia* $G_{\rm BP}$	*Gaia* $\sigma_{G_{\rm BP}}$	*ROSAT* $\log(L_X/L_{bol})$[a]
HD 214995	19.38	5.58	0.0	6.19	0.0	-5.4
HD 215545	13.99	6.54	0.0	6.7	0.0	-5.19
HD 216489	15.94	5.66	0.01	6.28	0.02	-4.02
HD 216718	16.36	5.53	0.01	5.97	0.0	-5.82
HD 216756	14.34	5.79	0.0	6.02	0.0	-5.84
HD 218356	14.79	4.24	0.0	5.03	0.0	-5.23
HD 218527	18.37	5.13	0.0	5.66	0.0	-5.51
HD 218658	14.1	4.2	0.0	4.66	0.01	-5.29
HD 218670	17.44	3.52	0.0	4.16	0.01	-5.43
HD 219916	15.76	4.56	0.0	5.1	0.0	-6.34
HD 220657	14.61	4.2	0.0	4.6	0.0	-4.9
HD 223011	12.45	6.27	0.0	6.39	0.0	-5.19
HD 223346	16.01	6.34	0.0	6.6	0.0	-5.47
HD 223460	16.45	5.62	0.0	6.09	0.0	-4.3

[a] *ROSAT* X-ray luminosity to bolometric luminosity ratio